

Cover Page



Universiteit Leiden

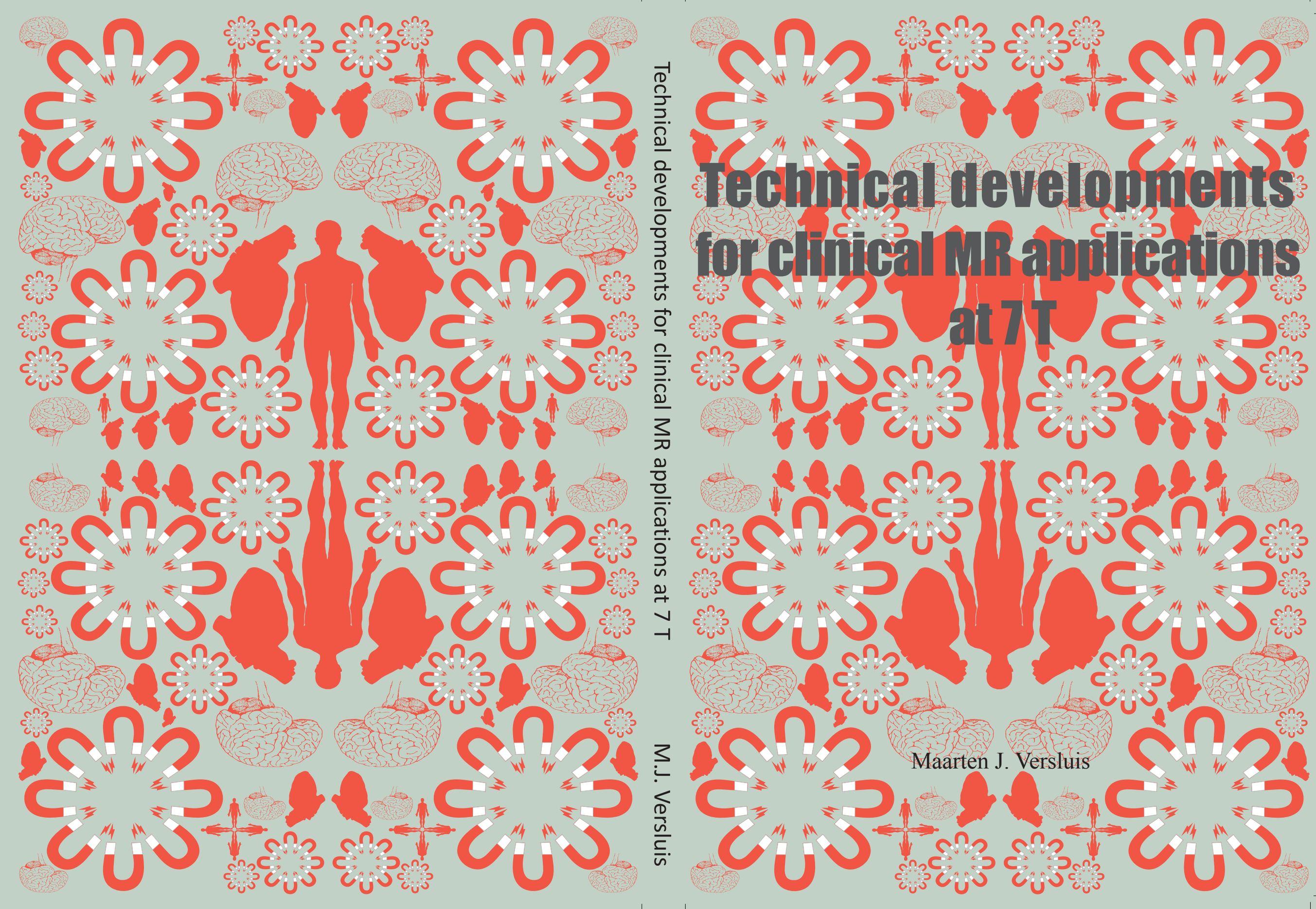


The handle <http://hdl.handle.net/1887/20590> holds various files of this Leiden University dissertation.

Author: Versluis, Maarten Jan

Title: Technical developments for clinical MR applications at 7 T

Issue Date: 2013-03-06



Technical developments for clinical MR applications at 7 T

Maarten J. Versluis

Technical developments for clinical MR applications at 7 T

M.J. Versluis

STELLINGEN

BEHORENDE BIJ HET PROEFSCHRIFT

TECHNICAL DEVELOPMENTS FOR CLINICAL MR APPLICATIONS AT 7 T

1. Resonance frequency fluctuations are a major cause of image artifacts in Alzheimer's Disease patients at high field (*this thesis*)
2. Modern RF coils with a high channel count can be used for accurate, real-time measurement of resonance frequency fluctuations using a navigator echo approach. (*this thesis*)
3. The increased phase shift between gray and white matter is a promising marker to reveal underlying AD pathology. (*this thesis*)
4. The frequent use of local Tx/Rx coils at 7 Tesla requires a specific RF power calibration method. (*this thesis*)
5. The effect of field strength on clinical diagnosis is difficult to quantify (J. Duyn, Neuroimage. 2012 Aug 15;62(2):1241-8)
6. Successful new techniques need to have the ability to provide unique contrast without sacrificing routine imaging contrast. (D. Sodickson)
7. A clinical role for tailored 7T cardiac MR applications is at the moment merely a vision. (T. Niendorf, Eur Radiol. 2010 Dec;20(12):2806-16)
8. High-field susceptibility-based MRI contrast can be used to reveal the local cortical architecture based on iron distribution. (M. Fukunaga, Proc Natl Acad Sci U S A. 2010 Feb 23;107(8):3834-9)
9. De ontwikkeling van 7 Tesla MRI is eerder technologie gedreven dan toepassings gedreven.
10. Alles is mogelijk. Wat mogelijk is, gebeurt. Alles gebeurt. (H. Mulisch)

Maarten J. Versluis
6 maart 2013

Technical developments for clinical MR applications at 7 T

Maarten Jan Versluis
2013

The studies presented in this thesis were performed at the C.J. Gorter center for high field MRI, of the department of Radiology of the Leiden University Medical Center, The Netherlands.

Part of this research was performed within the framework of CTMM, the Center for Translational Molecular Medicine (www.ctmm.nl), project LeARN (grant 02N-101).

Cover design by Michiel Wijtenburg (www.veld.nu)

Technical developments for clinical MR applications at 7 T

Proefschrift

ter verkrijging van
de graad van Doctor aan de Universiteit Leiden
op gezag van de Rector Magnificus prof. mr. C.J.J.M. Stolker,
volgens besluit van het College voor Promoties
te verdedigen op woensdag 6 maart 2013
klokke 15 uur

door

Maarten Jan Versluis

geboren te Bussum
in 1979

PROMOTIECOMMISSIE

PROMOTORES:

Prof. Dr. A.G. Webb
Prof. Dr. M.A. van Buchem

CO-PROMOTOR:

Dr. ir. M.J.P. van Osch

OVERIGE LEDEN:

Prof. Dr. H.J. Lamb
Prof. Dr. M.E. Ladd (E. L. Hahn Institute for MRI, Essen, Germany)
Dr. J.M. Hoogduin (Universitair Medisch Centrum Utrecht)

Table of Contents

1. Introduction and Outline 9

PART ONE: TECHNICAL DEVELOPMENTS - BODY APPLICATIONS

2. Simple RF design for human functional and morphological cardiac imaging at 7 Tesla 19

3. Right Coronary MR Angiography at 7 Tesla: A Direct Quantitative and Qualitative Comparison with 3 Tesla in Young Healthy Volunteers 33

4. Improved Signal-to-Noise in Proton Spectroscopy of the Human calf Muscle at 7 Tesla Using Localized B_1 Calibration 47

PART TWO: TECHNICAL DEVELOPMENTS - HIGH RESOLUTION BRAIN IMAGING

5. Origin and reduction of motion and f_0 artifacts in high resolution T_2^* -weighted magnetic resonance imaging: application in Alzheimer's disease patients 61

6. Retrospective image correction in the presence of non linear temporal magnetic field changes using multichannel navigator echoes 79

7. Fast high resolution whole brain T_2^* -weighted imaging using echo planar imaging at 7 Tesla 101

PART THREE: CLINICAL APPLICATION OF 7 TESLA MRI

8. Cortical phase changes in Alzheimer's disease at 7 Tesla MRI: a novel imaging marker 117

9. High-field imaging of neurodegenerative diseases 135

10. Subject tolerance of 7 Tesla MRI examinations 157

General discussion 167

Summary and Conclusions 177

Nederlandse Samenvatting en Conclusies 185

Dankwoord 201

Curriculum Vitae 205



Introduction and Outline

INTRODUCTION

Since the introduction of magnetic resonance imaging (MRI) in hospitals great efforts have been made in enhancing this technique and enabling its use in clinical practice. Constant improvements in field strength, gradients, coils and pulse-sequences have led to a steady increase in the number of MRI exams. To date more than 150 million examinations have been performed worldwide. Only recently, the conventional field strength for most exams was 1.5 Tesla, and 3 Tesla MRI scanners were used almost exclusively in large academic hospitals. Currently, the standard for many applications is shifting towards 3 Tesla due to improved image quality and information content. The recent introduction of whole body 7 Tesla MRI scanners has created a new research field, which requires new technical developments to benefit from its potential. At the end of 2012 approximately 35 of these systems were in operation, exclusively in research locations and academic hospitals. The work presented in this thesis describes a number of technical developments to enable the application of 7 Tesla MRI in a clinical (research) setting.

A higher magnetic field strength leads to an increased magnetization of spins, which in turn results in higher signal-to-noise ratio (SNR) that can be used for more detailed imaging, i.e. higher spatial resolution, shorter scanning times or increased (quantitative) information content. In addition, most contrast mechanisms are also dependent on field strength, leading to visualization of structures not visible at lower field strengths (1–5).

However on the downside, the technical complexity scales with field strength and not all previously developed techniques at lower field strengths can be translated easily to 7 Tesla. The increased magnetic field inhomogeneity, increased radiofrequency (RF) field (B_1) inhomogeneity due to shorter RF wavelengths and more easily reached temperature specific absorption rate (SAR) limits lead to important hardware and sequence challenges. It is crucial for the clinical acceptance and added value of 7 Tesla MRI to find solutions for these problems and to define the areas in which 7 Tesla MRI can help to improve diagnosis.

Literature shows promising results of early studies performed in patients with neurodegenerative diseases. Increased visualization of lesions in patients with Multiple Sclerosis (MS) (5, 6), increased sensitivity to the detection of cerebral microbleeds, common to many neurodegenerative diseases (7, 8) and visualization of small lenticulostriate arteries (2, 9, 10) could be obtained with 7 Tesla MRI. Initially imaging outside of the brain was expected to benefit less from the higher magnetic field strength, because the dimensions

of the human body lead to pronounced B_1 inhomogeneities and the large air cavities create strong B_0 inhomogeneities. However, with appropriate modification there are areas that could benefit. In imaging of the coronary arteries the increased SNR and improved background suppression due to longer longitudinal relaxation values (T_1) could allow for a higher spatial resolution to be able to assess branching vessels. Initial results have shown the feasibility of cardiac imaging (11, 12). Another technique, which is expected to benefit is magnetic resonance spectroscopy (MRS), both in the brain as well as in other anatomies. The higher precession frequency results in a greater frequency difference (chemical shift) between different metabolites and allows for the quantification of more metabolites with higher accuracy (13, 14). The quality of an MR spectrum relies strongly on a homogeneous B_0 and B_1 field, which are more difficult to achieve at a 7 Tesla than at lower field strengths. Therefore the full potential of MRS can only be obtained with suitable modifications.

In this thesis techniques for different anatomies of the human body were developed: brain, cardiac and leg muscle. This thesis is divided into three parts: part one deals with technical solutions for body applications, in particular to minimize the influence of increased B_1 -inhomogeneity. Part two describes developments to improve high resolution brain imaging and the last part provides clinical applications of 7 Tesla MRI and describes how examinations are perceived by healthy subjects.

The first part, consisting of **chapter 2, 3 and 4** is concerned with designing appropriate sequences and coils to cope with B_1 -homogeneity problems. The precession frequency of spins (Larmor frequency) is linearly dependent on the applied field strength and for proton nuclei at 7 Tesla, the most abundant of MR detectable spins in the human body the resonance frequency is approximately 300 MHz. A linear reduction in wavelength is observed with increasing Larmor frequency and at 7 Tesla the corresponding wavelength in tissue is in the same range as the dimensions of the human body (approximately 11 cm) leading to B_1 inhomogeneities that are non-existent or not as severe at 3 Tesla and 1.5 Tesla systems. As a result it is much more complicated to design suitable RF coils that have sufficient homogeneity over a large region of interest, a typical requirement for most imaging and spectroscopy studies. At the time of the introduction of 7 Tesla MRI scanners the only commercially available coil was a head coil. Therefore, in order to image other anatomies custom coil design was required. The second chapter describes the design of a coil and corresponding sequence modifications to enable imaging of the heart. Different coil configurations have been tested

to ensure sufficient coverage to image the entire heart, while avoiding tissue induced signal voids due to destructive RF field interference. The third chapter uses this coil to visualize the lumen of the right coronary artery in human volunteers. The small size of the coronary arteries requires high resolution imaging and therefore results in long scanning times. A higher magnetic field strength could prove beneficial for faster or more detailed visualization of the coronary arteries and the branching vessels in particular. In this chapter a comparison is made with 3 Tesla, and improved contrast and vessel sharpness were found at 7 Tesla compared to a similar protocol at 3 Tesla. In the fourth chapter a calibration sequence is introduced that measures locally the B_1 -field. Before each MR experiment the system needs to be calibrated to establish a relation between the amount of power needed from the RF amplifier and the resulting B_1 -field. This relation varies depending on subject, imaging location and RF coil. Conventionally a rapid MRI sequence is used that measures the average B_1 -field over a large region. This method is valid when the B_1 can be considered constant within this region, which is the case at lower field strengths and when using a RF body coil for excitation. At 7 Tesla and especially when using local RF coils this no longer the case. Therefore, an extension of the conventional calibration was designed to specifically measure the B_1 field in a small region-of-interest, which better represents the true underlying inhomogeneous B_1 -field. When this area of interest is small enough, such as in preparation of a single voxel MRS experiment the B_1 -field can be approximated as homogeneous. Using a volume selective RF calibration it was possible to correctly estimate the local flip angle. Subsequently, MR spectra obtained with these RF settings resulted in higher signal-to-noise ratios.

The second part, consisting of **chapter 5, 6 and 7** deals with technical developments aimed at high resolution brain imaging. One of the most striking examples of changed and increased contrast at 7 Tesla is provided by T_2^* -weighted images of the brain. This contrast is generated by a gradient echo sequence with a sufficiently long echo time and is sensitive to magnetic field inhomogeneities. Because the MR signal is a complex signal, both phase and magnitude images are obtained, which contain different information. The magnitude images reflect the T_2^* -value of the tissue, while the phase images are directly related to the underlying magnetic field. The fifth chapter describes the application of a T_2^* -weighted sequence in AD patients, because it was hypothesized that the high sensitivity of this sequence to magnetic field inhomogeneities and thus to disease specific changes in tissue iron concentration, would enable the detection of AD-plaques. However, the sequence is also sensitive to unwanted static and dynamic magnetic field inhomogen-

eities caused by e.g. air cavities, respiration and body movements. This problem is greater at high magnetic field strengths, because the amplitude of the inhomogeneities scales linearly with the magnetic field strength. Whereas static field inhomogeneities result in artifacts close to the field disturbance, dynamic magnetic field fluctuations result in an overall degradation of the image quality. To obtain reliable image quality in AD patients a sequence modification had to be made to dynamically measure the magnetic field during image acquisition, termed a navigator echo. Retrospectively this information can be used to remove the effect of the unwanted magnetic field inhomogeneities from the data to obtain high quality data. The sixth chapter introduces an extension of this technique by including a measurement of the spatial variation within a slice by using multiple coil elements and the corresponding sensitivity profiles, termed sensitivity encoded (SENSE) navigators. The corresponding image quality of corrupted scans was proven to be substantially improved using the extended technique. Chapter 7 describes the implementation of a very efficient sequence to obtain whole brain high resolution T_2^* -weighted images using echo planar imaging (EPI). EPI is not frequently used for high resolution imaging, mainly due to image distortions and signal voids. The sequence described in this chapter limits the amount of distortions, while obtaining a significant gain in speed to allow for whole brain acquisitions within reasonable scanning times. This is important for clinical use and it also reduces the chance that images are corrupted by motion.

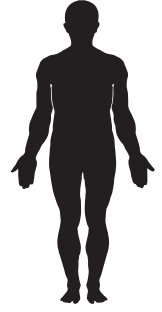
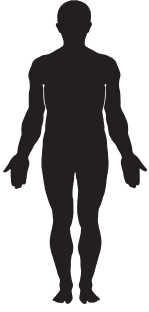
Finally the third part, consisting of **chapter 8, 9 and 10** demonstrates the application of 7 Tesla in clinical studies. Chapter 8 describes a study performed in patients with AD using a high resolution T_2^* -weighted sequence, which was corrected for dynamic magnetic field fluctuations (see chapter 5). One of the hallmarks of the disease is the deposition of the protein Amyloid- β locally in the cortex, co-localized with iron. By using the phase of the complex MR signal a measure for the susceptibility difference between neighboring tissues can be obtained. This measure is expected to change depending on the amount of iron present. The chapter shows that phase measurements provide an accurate tool to differentiate AD patients from healthy controls, potentially enabling to follow disease progress in an earlier stage. Chapter 9 provides a review of the current state of clinical studies that have been performed at 7 Tesla in patients with neurodegenerative diseases. At the time of writing only a limited number of patient studies have been performed using 7 Tesla. Even though the full potential of improved detail and image quality compared to lower field strengths still remains to be proven, specific cases of 7 Tesla MRI have demonstrated an advantage over lower field strengths.

In chapter 10 the results of a short survey that was conducted with the first 101 healthy volunteers participating in 7 Tesla MRI studies are presented. How well a 7 Tesla MRI examination is perceived is of great importance for the patient acceptance of 7 Tesla MRI. Although some side effects were mentioned, mostly nausea and scanner noise, the large majority of the subjects felt comfortable during the examination.

Chapter 11 provides a general discussion of these scientific chapters.

REFERENCES

1. Duyn JH, van Gelderen P, Li T-Q, de Zwart JA, Koretsky AP, Fukunaga M. High-field MRI of brain cortical substructure based on signal phase. *Proceedings of the National Academy of Sciences* 2007 ;104:11796–11801.
2. Kang C-K, Park C-W, Han J-Y, Kim S-H, Park C-A, Kim K-N, Hong S-M, Kim Y-B, Lee KH, Cho Z-H. Imaging and analysis of lenticulostriate arteries using 7.0-Tesla magnetic resonance angiography. *Magnetic Resonance in Medicine* 2009 ;61:136–144.
3. Fukunaga M, Li T-Q, van Gelderen P, de Zwart JA, Shmueli K, Yao B, Lee J, Maric D, Aronova MA, Zhang G, Leapman RD, Schenck JF, Merkle H, Duyn JH. Layer-specific variation of iron content in cerebral cortex as a source of MRI contrast. *Proceedings of the National Academy of Sciences* 2010 ;107:3834 –3839.
4. Zwanenburg JJM, Hendrikse J, Luijten PR. Generalized multiple-layer appearance of the cerebral cortex with 3D FLAIR 7.0-T MR imaging. *Radiology* 2012 ;262:995–1001.
5. Tallantyre EC, Morgan PS, Dixon JE, Al-Radaideh A, Brookes MJ, Morris PG, Evangelou N. 3 Tesla and 7 Tesla MRI of multiple sclerosis cortical lesions. *J Magn Reson Imaging* 2010 ;32:971–977.
6. Kollia K, Maderwald S, Putzki N, Schlamann M, Theysohn JM, Kraff O, Ladd ME, Forsting M, Wanke I. First Clinical Study on Ultra-High-Field MR Imaging in Patients with Multiple Sclerosis: Comparison of 1.5T and 7T. *AJNR Am J Neuroradiol* 2009 ;30:699–702.
7. Conijn MMA, Geerlings MI, Biessels G-J, Takahara T, Witkamp TD, Zwanenburg JJM, Luijten PR, Hendrikse J. Cerebral Microbleeds on MR Imaging: Comparison between 1.5 and 7T. *AJNR Am J Neuroradiol* 2011 ;32:1043–1049.
8. Greenberg SM, Vernooij MW, Cordonnier C, Viswanathan A, Al-Shahi Salman R, Warach S, Launer LJ, Van Buchem MA, Breteler MM. Cerebral microbleeds: a guide to detection and interpretation. *The Lancet Neurology* 2009 ;8:165–174.
9. Liem MK, van der Grond J, Versluis MJ, Haan J, Webb AG, Ferrari MD, van Buchem MA, Lesnik Oberstein SAJ. Lenticulostriate Arterial Lumina Are Normal in Cerebral Autosomal-Dominant Arteriopathy With Subcortical Infarcts and Leukoencephalopathy. *Stroke* 2010 ;41:2812 –2816.
10. Hendrikse J, Zwanenburg JJ, Visser F, Takahara T, Luijten P. Noninvasive Depiction of the Lenticulostriate Arteries with Time-of-Flight MR Angiography at 7.0 T. *Cerebrovasc Dis* 2008 ;26:624–629.
11. Vaughan JT, Snyder CJ, DelaBarre LJ, Bolan PJ, Tian J, Bolinger L, Adriany G, Andersen P, Strupp J, Ugurbil K. Whole-body imaging at 7T: Preliminary results. *Magnetic Resonance in Medicine* 2009 ;61:244–248.
12. Elderen SGC van, Versluis MJ, Webb AG, Westenberg JJM, Doornbos J, Smith NB, Roos A de, Stuber M. Initial results on in vivo human coronary MR angiography at 7 T. *Magnetic Resonance in Medicine* 2009 ;62:1379–1384.
13. Tkáč I, Oz G, Adriany G, Ugurbil K, Gruetter R. In vivo ¹H NMR spectroscopy of the human brain at high magnetic fields: metabolite quantification at 4T vs. 7T. *Magn Reson Med* 2009 ;62:868–879.
14. van den Bogaard SJA, Dumas EM, Teeuwisse WM, Kan HE, Webb A, Roos RAC, van der Grond J. Exploratory 7-Tesla magnetic resonance spectroscopy in Huntington's disease provides in vivo evidence for impaired energy metabolism. *J. Neurol.* 2011 ;258:2230–2239.



Technical developments Body



2

Simple RF design for human functional and morphological cardiac imaging at 7 Tesla.

*M.J. Versluis
N. Tsekos
N.B. Smith
A.G. Webb*

ABSTRACT

Morphological and functional cardiac MRI can potentially benefit greatly from the recent advent of commercial high-field (7 Tesla and above) MRI systems. However, conventional hardware configurations at lower field using a body coil for homogeneous transmission are not available at these field strengths. Sophisticated multiple-transmit-channel systems have been shown to be able to image the human heart at 7 Tesla (T) but such systems are currently not widely available. In this paper, we empirically optimize the design of a simple quadrature coil for cardiac imaging at 7 T. The size, geometry, and position have been chosen to produce a B_1 field with no tissue-induced signal voids within the heart. Standard navigator echoes for gating were adapted for operation at the heart/lung interface, directly along the head-foot direction. Using this setup, conventional and high resolution cine functional imaging have been successfully performed, as has morphological imaging of the right coronary artery.

INTRODUCTION

The majority of high field MRI studies have focused on the brain, with developments such as transmit arrays(1), contrast optimization (2) and RF pulse design for increased B_1 homogeneity (3) forming a few of the areas of active technical research. Musculoskeletal imaging at 7 T has also seen a recent surge in activity (4–6). Abdominal imaging is acknowledged to be the most challenging area for high field MRI due to the large dimensions of the torso. The fact that these dimensions are now significantly greater than the wavelength of the electromagnetic (EM) radiation in tissue result in sample induced inhomogeneities in the transmitted and received B_1 fields. The complex wave behavior can also cause electric field “hot-spots”, resulting in raised local heating. Similar effects in the field of electromagnetic hyperthermia have been known for many decades, as has the solution of using transmit arrays with different magnitudes and phases applied to each element of the array (7, 8). In MRI terms, this process has been termed “ B_1 -shimming” (9), in which the spatial distributions of the magnetic component of the EM field is the major focus of the optimization strategy.

Only recently has it been shown that whole-body imaging is feasible at 7 Tesla and above (10). The authors showed results from both an actively detunable TEM resonator combined with multi-channel stripline detector, and a full transmit array (10). Specific results have also been shown for the heart using this type of RF hardware (11). This approach can be considered as the optimum engineering solution, but does require extensive hardware design and construction, and a very high level of technical skill to implement successfully. The purpose of our current study was to determine whether a much more simple approach could be used to acquire both morphological and functional cardiac images of clinical utility at 7 T.

In terms of cardiac imaging, the pros and cons of moving from lower to higher magnetic fields have been discussed previously in (12) and references therein, comparing 1.5 T and 3 T: such considerations are also pertinent when considering cardiac imaging at 7 T. Briefly, the advantages of higher fields include improved tagging due to the prolonged T_1 time of the myocardium, improved perfusion imaging both due to the increased signal-to-noise (S/N) and the longer myocardial T_1 values, and a higher velocity-to-noise ratio in blood velocity measurements. Specific challenges outlined in (12) included implementation of high efficiency balanced SSFP sequences without off-resonance banding artifacts, the detrimental effects of B_1 and B_0 inhomogeneity on inversion-recovery prepared sequences in particular, and the high potential specific absorption ratio (SAR). Although not mentioned, localized

MR spectroscopy is also an area that should profit considerably from the higher field. Based upon these observations, the potential of cardiac imaging at 7 T appears very high.

In this paper we show that a simple RF coil configuration can be used to acquire high quality cardiac images at 7 T. The geometry of a quadrature transmit/receive surface coil was optimized to achieve coverage across the entire heart, enabling acquisition of functional cine images in both four-chamber and two-chamber cross-sections, as well as morphological images of the right coronary artery (RCA).

MATERIALS AND METHODS

All experiments were performed using a Philips Achieva 7 T whole body system. The system has a single proton RF transmit channel, with two quadrature ports available on the RF interface box, through which custom-built coils can be connected via simple type-N connectors. The maximum power from the RF amplifier is 4 kW, with approximately a 50% loss through ~20 meters of cabling between the amplifier and coil interface: the maximum available power for each quadrature channel is therefore ~1 kW. All experiments were approved by the Commissie Medische Ethiek at the Leiden University Medical Center.

RF coil geometry.

In addition to improving the S/N, quadrature coils help to alleviate the B_1 inhomogeneities encountered at high field (13). In this study, the different quadrature coil configurations tested included overlapped circular and rectangular loops, rectangular loops with central common capacitors (14), and loop/butterfly pairs (15): this list is certainly not exhaustive, but represents the most commonly used configurations. For a given size, the performance of each coil was assessed in terms of B_1 homogeneity and S/N. Any coil arrangement that produced a significant dark “banding” within the image was discarded, irrespective of the S/N. Empirically, we observed that the optimum arrangement was the loop/butterfly pair. As described by Kumar and Bottomley (16), for circular loops the geometry that produces the maximum intrinsic S/N (excluding system and conductive losses in the detector) at a depth d is given at low frequencies by $r_0 = d/\sqrt{5}$ and $r_8 = 0.6d$, where r_0 is the radius of the single loop, and r_8 that of each half of the butterfly coil. The distance to the center of the heart from the surface of the chest in a typical volunteer was approximately 10 cm: the single loop was placed 2 cm above the chest, and the butterfly coil 1 cm above the chest, in accordance with the

“liftoff” phenomenon described by Suits et al. (17). These numbers give values of 10.8 cm for the diameter of the single loop and 13.2 cm for the diameter of each loop of the butterfly coil. Upon testing, it was found that these dimensions did not give sufficient penetration for the posterior part of the heart to be seen with sufficient S/N, and so the dimensions were increased successively until the heart could be fully visualized. The values determined empirically were 15 cm diameter for the single loop and 18 cm diameter for each loop of the butterfly coil. The RF coils were segmented into conductor lengths of 6 cm, corresponding to $\sim\lambda/16$ at 298 MHz, using 3.9 pF non-magnetic capacitors (ATC, Series B, Huntington Station, NY). Three variable capacitors (1-40 pF, Johansson, Camarillo, CA) were used for fine tuning and impedance matching in a balanced configuration. A lattice balun was used to improve the balance of the coil. Finally, a 1 cm diameter gap, filled with foam, was used between the coil and patient to avoid very heavy sample losses (17). Figures 1(a), (b) and (c) show schematics and a photograph of the coil geometry and placement on the subject.

Network analyzer measurements were performed on the patient outside the magnet and, after fine tuning, the S_{11} and S_{22} parameters were both less than -20 dB, with the S_{21} between -18 and -24 dB for all patients studied. The unloaded and loaded Q values were measured to be 186 and 18, respectively. There is a negligible frequency shift when the coil is placed on the patient since the 1 cm spacer reduces the interaction of the strong electric fields around each capacitor with the body.

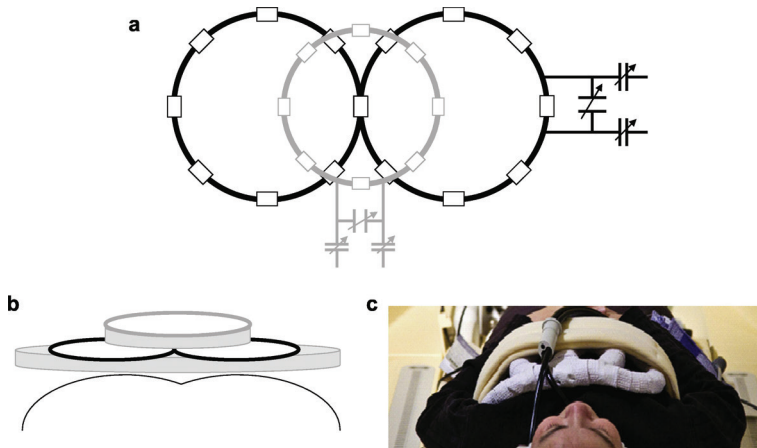


Figure 1. Schematic of RF coils

(a) The single loop (gray lines)/butterfly coil (black lines) configuration. Capacitors are denoted by the small boxes. The impedance matching networks are shown for each coil. (b) Physical placement of the coils on the subject's chest. The shaded regions represent open-core foam of thickness 1 cm. (c) Photograph of the coil assembly placed on top of the volunteer, and interfaced to the quadrature transmit/receive box of the Philips 7 tesla.

Vector electrocardiogram (vEKG).

A four-channel commercial vector ECG (VECG) module was used to trigger from the R-wave. Despite the well-known magneto-hydraulic effect, EKG's were obtained in the vast majority of cases without the need for electrode repositioning, as has also been reported by Snyder et al (11).

Navigator gating.

Navigator echo gating was used for imaging the RCA using a "pencil-beam" navigator. Conventional navigator gating has the pencil beam centered on the right hemi diaphragm, at the lung/liver interface in a head/foot direction. Since coverage was limited in the head/foot direction using the surface coil setup, we adapted the pencil beam to be situated at the heart/lung interface, but maintaining the head/foot direction of the navigator. This approach was based on previous experience of coronary artery imaging at 7 T (18), and proved to be highly reproducible despite the relatively small surface area perpendicular to the navigator beam, as compared to the conventional configuration.

Cine imaging.

Cine images were acquired using a segmented gradient echo sequence with

RF spoiling and crusher gradients to eliminate transverse magnetization. A TURBOFLASH gradient echo sequence was used for prescribing the short axis views planes for cine imaging. Multislice cine scans were acquired in multiple breath-holds (acquiring one or two slices per breath-hold).with the following parameters: TR / TE =4 ms / 2.4 ms, tip angle=20°, voxel size = 1.3 x 1.4 x 8 mm³, 12-14 slices. VECG triggering was used retrospectively to reconstruct 33 heart phases. High resolution cine images were acquired for a single slice in a breath hold of ~20 s with the following parameters: TR / TE = 5.4 / 3.4 ms, tip angle = 20°, voxel size = 0.65 x 0.7 x 8 mm³.

Coronary artery imaging.

The procedure for acquisition of the coronary artery geometry is described in detail elsewhere (18). To summarize, the basic steps are to acquire scout scans for the visual identification of the time period (Td) of minimal coronary motion. The scan plane is then localized parallel to the right coronary artery (RCA). Free-breathing 3D coronary MRA (segmented k-space gradient-echo imaging, TR=4 ms, TE=1.5 ms, RF excitation angle=15°, field-of-view=320x291 mm², scan matrix=392x373, 15 slices, slice thickness=2 mm, acquisition window ~ 100 ms, scan time ~ 5 min) was performed using prospective navigator gating with the 2D selective navigator localized at the heart-lung interface. Image data were collected in mid-diastole at the predetermined time Td. An adiabatic spectrally selective inversion recovery module with inversion time (TI) = 305ms was used for fat suppression to enhance the endogenous contrast between the coronary blood-pool and epicardial fat.

Estimation of B_1^+ for SAR calculations.

The B_1^+ field was estimated using an interleaved dual repetition FLASH sequence which allows a direct calculation of the tip angle distribution (19). The following parameters were used: TR₁ / TR₂ / TE = 15 / 75 / 1.0 ms, tip angle = 40°, voxel size = 2.3 x 4.6 x 15 mm³, 15 signal averages, total scan duration was 3 minutes. Images were acquired in the transverse plane for measurements at the chest surface and also at the center of the heart. Fifteen signal averages were acquired to reduce the effects of heart motion on the estimated B_1^+ map. It should be noted that the results obtained are only estimations, and are not absolutely quantitative due to the fact that, for practical purposes of scanning time, the maps were acquired in 2D rather than 3D scans (20). Because of the thick slice and the number of averages the effect that respiratory and cardiac motion have on the steady state magnetization is expected to be minimal.

RESULTS

Coil performance.

Figure 2 shows images acquired with three different RF coil configurations using a low flip angle, low resolution TURBOFLASH sequence to assess the B_1 profile of each configuration. Figure 2a uses a single loop coil, and displays minor non-uniformity in the image, as predicted by a number of previous studies. Figure 2b shows the results of using the loop/butterfly combination driven in quadrature, with not only the expected increase in penetration depth, but also an improvement in the B_1 uniformity. The improvement in B_1 may also be indirectly appreciated considering the increased CNR between the septal wall and the two ventricles, the improved B_1 results to a higher effective flip angle. It should be noted that the symmetric sensitivity profile of the quadrature coil arises from the combination of two asymmetric fields, the B_1^+ transmit field and the B_1^- receive field, as described previously by Wang et al.(21). Figure 2c is illustrative, in the sense that the two coils are driven in an anti-quadrature configuration, and gives a good indication of areas in which the B_1 fields of the two coils are orthogonal.

Cine-scans.

Individual frames of a cine-sequence at a “conventional” spatial resolution of $1.3 \times 1.4 \times 8 \text{ mm}^3$ are shown in Figures 3 and 4 for the short-axis and four-chamber configurations, respectively. There is excellent blood/myocardium contrast and no areas of B_1 inhomogeneity beyond those which are associated with the intrinsic drop-off of B_1 amplitude from a surface coil. The SNR of the myocardium was measured to be between 10 and 25:1 depending on the particular area of the myocardium, the SNR of the left ventricle was between 20 and 40:1. In order to take advantage of the high sensitivity of the 7 T, a high resolution cine scan was run on one volunteer. Images with a spatial resolution of $0.65 \times 0.7 \times 8 \text{ mm}^3$ are shown in Figure 5. Although the SNR is obviously reduced compared to the images in Figures 3 and 4, there is much finer definition of the cardiac muscles.

Coronary artery imaging.

Figure 6 shows successive slices in which the right coronary artery can be easily visualized, together with an expanded view for clarity. There is good contrast between the artery and the surrounding tissue, allowing clear delineation of the artery walls. In all high field human studies, an important issue is the specific absorption rate (SAR), both in terms of local and average values.

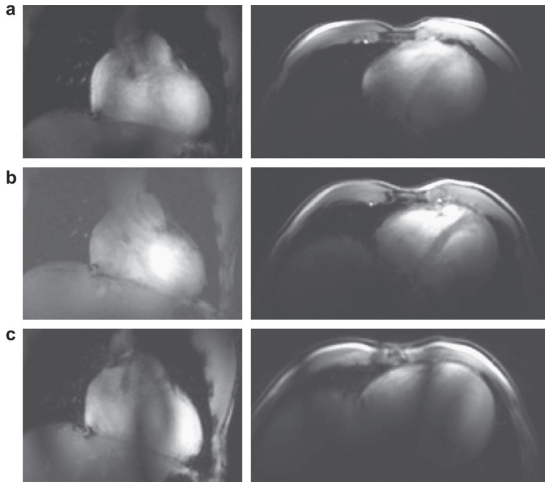


Figure 2. Scout images of different coil configurations

Coronal (left) and axial (right) low-resolution scout images acquired using different coil configurations. (a) Single loop coil, (b) loop/butterfly pair in quadrature configuration, (c) loop/butterfly pair in an anti-quadrature configuration. *SAR estimation.*

Despite some initial promising studies using direct MRI temperature measurements in vivo, it remains extremely challenging to measure SAR directly, and so most estimations are based on computer simulations. Since blood perfusion is not included in the majority of simulations, one must also recognize that such simulations represent “worst-case” scenarios in terms of causing actual tissue heating. We have based our SAR estimations on previous work by Collins and Smith (22), who specifically modeled the SAR for a surface coil adjacent to an anatomically-correct human body model. The regions of highest SAR were found to be at the right medial portion of the pectoral muscle near the superior end of the sternum: the SAR in the heart itself is extremely low. The authors provide appropriate scaling factors for setups different than the particular one which they studied.

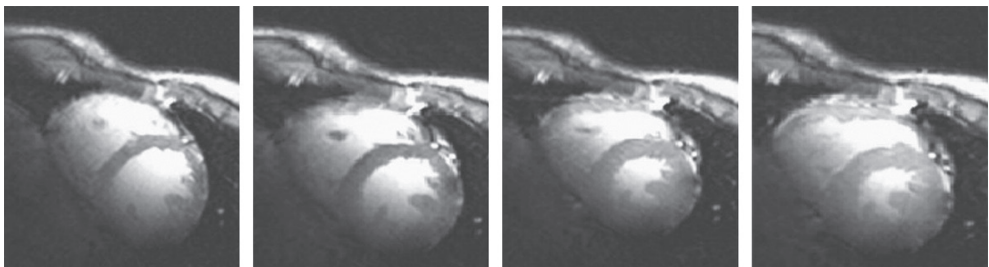


Figure 3. Images from a short-axis cine sequence.

Images are acquired over eight breath-holds with times corresponding to 25 ms intervals. Shown is every fourth image acquired at times 0, 99, 198 and 297 ms after the R-wave.

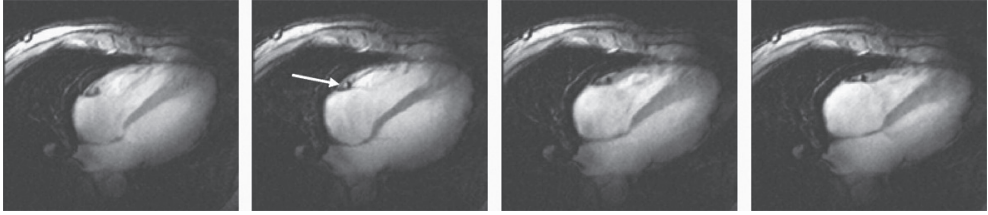


Figure 4. Images from a four-chamber cine sequence.

Images are acquired over eight breath-holds with times corresponding to 27 ms intervals. Every fourth images is shown above at times 108, 216, 324 and 432 ms after the R-wave. Data acquisition parameters are described in the main text. The right coronary artery can also be seen (small arrow) perpendicular to the slice dimension.

The initial step was to estimate the B_1^+ using the same power level as for all the cine sequences. Using the technique outlined previously our estimated B_1^+ at the center of the heart was 1.4 μT (using a 0.6 ms duration half sinc-gauss excitation pulse) and at the surface of the chest was 4.9 μT , compared to values of 1.875 μT and 20 μT from a 3 ms rectangular pulse used in the Collins paper (22). The difference in the ratios of the two values can be at least in part explained by the larger surface coil chosen for the simulations (a 22.9 cm diameter linear surface coil with four-port drive). The results from the Collins and Smith paper were interpolated to values at 298.1 MHz since frequencies of 64, 125, 175, 260 and 345 MHz were used in the original simulations. Using the fact that the SAR is proportional to the time integral of the magnitude of the square of the B_1^+ field, we can arrive at approximate SAR values. The SAR in the heart is, as derived from the relative B_1^+ values, negligible compared to that at the chest surface. As noted by Collins and Smith, the local SAR is the limiting factor, since the average SAR is up to two orders of magnitude less. The estimated value of local SAR at the chest surface is ~ 0.2 W/kg per 1 g of tissue, which is more than a factor-of-four below those of the Food and Drug Administration (FDA) and International Electro-technical Commission (IEC).

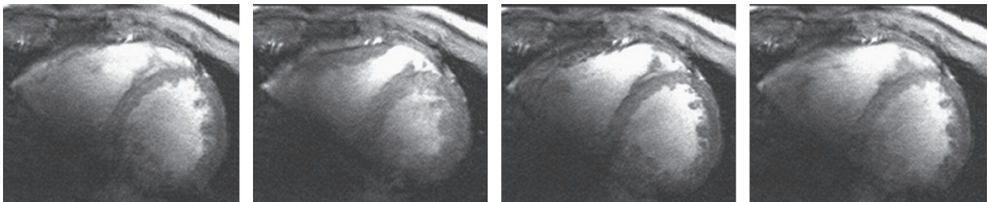


Figure 5. Images from a high resolution short-axis cine sequence.

Every fourth frame from a high-resolution cine sequence showing excellent delineation of the papillary muscles in the myocardium. Images were acquired every 35 ms.

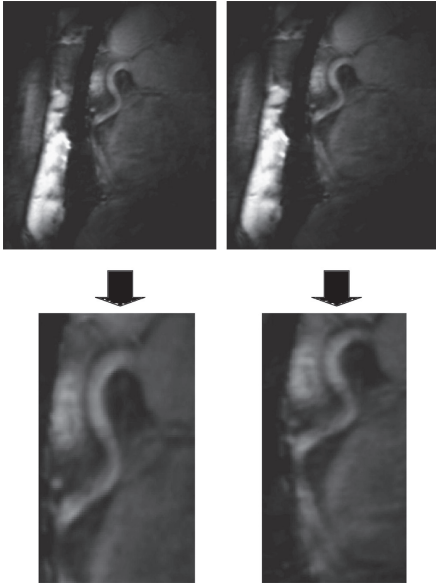


Figure 6. Right coronary artery.

Two successive slices through a volunteer showing the right coronary artery.(top). Expansion of the images showing more clearly the delineation of the artery (bottom).

CONCLUSIONS

Although the optimum RF engineering configuration for high field body imaging will ultimately consist of separate multi-channel transmit and receive arrays, this setup is not widely available at the current time, and there is a sentiment that it is not possible to perform useful body imaging at 7 tesla and above without such technology. The results shown here illustrate that a well-designed simple coil setup is capable of obtaining both cine-cardiac sequences for functional applications, as well as structural information related to, for example, dimensions of the coronary artery.

A number of challenges remain to be addressed. For example, the use of high efficiency balanced imaging sequences is routine at 1.5 tesla, but has proved challenging to implement at 3 tesla (12) and is likely to require sophisticated higher order shimming to be even feasible at 7 tesla. The lack of a body-coil for uniform excitation also makes many standard preparation modules for imaging sequences difficult: for example, black-blood imaging or quantitative velocity measurements. One of the most promising applications for very high field cardiac MR is localized cardiac spectroscopy (both homonuclear and heteronuclear), which has the advantage of significantly enhanced spectral resolution, but again has a number of significant challen-

ges in order to obtain high quality spectra. The aim of this current paper is to show that, even with relatively simple RF coil design, both functional and structural information can be obtained, and that many groups can now apply their expertise acquired at lower fields to the challenges of cardiac MR at 7 tesla and above.

ACKNOWLEDGEMENTS

The help of Saskia van Elderen and Albert de Roos at the Leiden University Medical Center, as well as Matthias Stuber at Johns Hopkins, is gratefully acknowledged.

REFERENCES

1. Adriany G, Van de Moortele P-F, Ritter J, Moeller S, Auerbach EJ, Akgün C, Snyder CJ, Vaughan T, Uğurbil K. A geometrically adjustable 16-channel transmit/receive transmission line array for improved RF efficiency and parallel imaging performance at 7 Tesla. *Magn Reson Med* 2008 ;59:590–597.
2. Duyn JH, van Gelderen P, Li T-Q, de Zwart JA, Koretsky AP, Fukunaga M. High-field MRI of brain cortical substructure based on signal phase. *Proc Natl Acad Sci U S A* 2007 ;104:11796–801.
3. Zelinski AC, Wald LL, Setsompop K, Alagappan V, Gagoski BA, Goyal VK, Adalsteinsson E. Fast slice-selective radio-frequency excitation pulses for mitigating B₁+ inhomogeneity in the human brain at 7 Tesla. *Magn Reson Med* 2008 ;59:1355–1364.
4. Krug R, Carballido-Gamio J, Banerjee S, Burghardt AJ, Link TM, Majumdar S. In vivo ultra-high-field magnetic resonance imaging of trabecular bone microarchitecture at 7 T. *J Magn Reson Imaging* 2008 ;27:854–859.
5. Krug R, Carballido-Gamio J, Banerjee S, Stahl R, Carvajal L, Xu D, Vigneron D, Kelley DAC, Link TM, Majumdar S. In vivo bone and cartilage MRI using fully-balanced steady-state free-precession at 7 tesla. *Magn Reson Med* 2007 ;58:1294–1298.
6. Zuo J, Bolbos R, Hammond K, Li X, Majumdar S. Reproducibility of the quantitative assessment of cartilage morphology and trabecular bone structure with magnetic resonance imaging at 7 T. *Magn Reson Imaging* 2008 ;26:560–566.
7. Sullivan D. Mathematical methods for treatment planning in deep regional hyperthermia. *IEEE Transactions on Microwave Theory and Techniques* 1991 ;39:864–872.
8. Wust P, Nadobny J, Felix R, Deuffhard P, Louis A, John W. Strategies for optimized application of annular-phased-array systems in clinical hyperthermia. *Int J Hyperthermia* 1991 ;7:157–173.
9. Metzger GJ, Snyder C, Akgun C, Vaughan T, Ugurbil K, Van de Moortele P-F. Local B₁+ shimming for prostate imaging with transceiver arrays at 7T based on subject-dependent transmit phase measurements. *Magn Reson Med* 2008 ;59:396–409.
10. Vaughan JT, Snyder CJ, DelaBarre LJ, Bolan PJ, Tian J, Bolinger L, Adriany G, Andersen P, Strupp J, Ugurbil K. Whole-body imaging at 7T: Preliminary results. *Magnetic Resonance in Medicine* 2009 ;61:244–248.

11. Snyder CJ, DelaBarre L, Metzger GJ, Moortele P-F van de, Akgun C, Ugurbil K, Vaughan JT. Initial results of cardiac imaging at 7 tesla. *Magnetic Resonance in Medicine* 2009 ;61:517–524.
12. Gharib AM, Elagha A, Pettigrew RI. Cardiac magnetic resonance at high field: promises and problems. *Curr Probl Diagn Radiol* 2008 ;37:49–56.
13. Hoult DI, Phil D. Sensitivity and power deposition in a high-field imaging experiment. *J Magn Reson Imaging* 2000 ;12:46–67.
14. Boskamp EB. Magnetic resonance imaging apparatus comprising a quadrature coil system. 1989 ;
15. Hyde JS, Jesmanowicz A, Grist TM, Froncisz W, Kneeland JB. Quadrature detection surface coil. *Magn Reson Med* 1987 ;4:179–184.
16. Kumar A, Bottomley PA. Optimized quadrature surface coil designs. *MAGMA* 2008 ;21:41–52.
17. Suits BH, Garroway AN, Miller JB. Surface and gradiometer coils near a conducting body: the lift-off effect. *J. Magn. Reson.* 1998 ;135:373–379.
18. Elderen SGC van, Versluis MJ, Webb AG, Westenberg JJM, Doornbos J, Smith NB, Roos A de, Stuber M. Initial results on in vivo human coronary MR angiography at 7 T. *Magnetic Resonance in Medicine* 2009 ;62:1379–1384.
19. Yarnykh VL. Actual flip-angle imaging in the pulsed steady state: A method for rapid three-dimensional mapping of the transmitted radiofrequency field. *Magnetic Resonance in Medicine* 2007 ;57:192–200.
20. Wu X, Deelchand D, Yarnykh V, Ugurbil K, Van de Moortele P. Actual flip angle imaging: from 3D to 2D. In: *Proc. Intl. Soc. Mag. Reson. Med.* 2009. p. 371.
21. Wang J, Yang QX, Zhang X, Collins CM, Smith MB, Zhu X-H, Adriany G, Ugurbil K, Chen W. Polarization of the RF field in a human head at high field: a study with a quadrature surface coil at 7.0 T. *Magn Reson Med* 2002 ;48:362–369.
22. Collins CM, Smith MB. Calculations of B(1) distribution, SNR, and SAR for a surface coil adjacent to an anatomically-accurate human body model. *Magn Reson Med* 2001 ;45:692–699.

3

Right Coronary MR Angiography at 7 Tesla: A Direct Quantitative and Qualitative Comparison with 3 Tesla in Young Healthy Volunteers

*S.G.C. van Elderen
M.J. Versluis
J.J.M. Westenberg
H. Agarwal
N.B. Smith
M. Stuber
A. de Roos
A.G. Webb*

ABSTRACT*Purpose:*

To objectively compare quantitative parameters related to image quality attained at coronary magnetic resonance (MR) angiography of the right coronary artery (RCA) performed at 7 Tesla (T) and 3 T.

Materials and Methods:

Institutional review board approval was obtained, and volunteers provided signed informed consent. Ten healthy adult volunteers (mean age \pm standard deviation, 25 years \pm 4; seven men, three women) underwent navigator-gated three-dimensional MR angiography of the RCA at 7 T and 3 T. For 7 T, a custom-built quadrature radiofrequency transmit-receive surface coil was used. At 3 T, a commercial body radiofrequency transmit coil and a cardiac coil array for signal reception were used. Segmented k-space gradient-echo imaging with spectrally selective adiabatic fat suppression was performed, and imaging parameters were similar at both field strengths. Contrast-to-noise ratio between blood and epicardial fat; signal-to-noise ratio of the blood pool; RCA vessel sharpness, diameter, and length; and navigator efficiency were quantified at both field strengths and compared by using a Mann-Whitney U test.

Results:

The contrast-to-noise ratio between blood and epicardial fat was significantly improved at 7 T when compared with that at 3 T (87 ± 34 versus 52 ± 13 ; $P = .01$). Signal-to-noise ratio of the blood pool was increased at 7 T (109 ± 47 versus 67 ± 19 ; $P = .02$). Vessel sharpness obtained at 7 T was also higher ($58\% \pm 9$ versus $50\% \pm 5$; $P = .04$). At the same time, RCA vessel diameter and length and navigator efficiency showed no significant field strength dependent difference.

Conclusion:

In our quantitative and qualitative study comparing in vivo human imaging of the RCA at 7 T and 3 T in young healthy volunteers, parameters related to image quality attained at 7 T equal or surpass those from 3 T.

INTRODUCTION

Currently, relatively few (approximately 40) 7 T magnetic resonance (MR) imaging systems are available for human use, and most of them are situated in research centers. High-field-strength cardiac MR imaging initially was thought to be problematic due to magnetic field inhomogeneity and specific absorption rate constraints. Furthermore, contemporary commercial 7 T units are not routinely equipped with body radiofrequency (RF) transmit coils or surface RF receive coils. Despite these major challenges, a number of research groups already have demonstrated the feasibility of cardiac imaging at 7 T and beyond (1–5). Initial attempts focusing on coronary artery imaging at 7 T showed that these barriers can be removed successfully, and initial in vivo human images were promising (6). Although these early 7 T studies were conducted by using single-channel RF transmit-receive coil architecture, recent advances in surface coil technology seem particularly promising. However, although an improvement in image quality may be expected at higher magnetic field strength (7), there have been no reports, to our knowledge, on cardiac MR imaging studies in which investigators directly and objectively compare parameters related to image quality at 7 T with those obtained at lower field strength. Therefore, the purpose of our study was to objectively compare quantitative parameters related to image quality attained at coronary MR angiography of the right coronary artery (RCA) performed at 7 T and 3 T.

MATERIALS AND METHODS

Our study was approved by our institutional review board, and all volunteers provided signed informed consent. Three-dimensional (3D) MR angiography of the right coronary system was performed in 10 healthy young adult volunteers (mean age \pm standard deviation, 25 years \pm 4; seven men, three women) who underwent imaging at 7 T and 3 T (Achieva; Philips Healthcare, Best, the Netherlands) in a prospective study design. For practical reasons, 7 T imaging always occurred before 3 T imaging. Coronary MR Angiography was performed with prospective navigator technology and vector electrocardiographic (ECG) triggering (8). All volunteers underwent imaging in a head-first, supine position. None of the volunteers received nitroglycerin before MR imaging. The mean interval between the two examinations was 8 weeks \pm 5.

Imaging at 7 T

A quadrature transmit-receive surface coil consisting of two overlapping

loops (13-cm diameter each) was constructed in-house (Fig 1). The coil size is larger than described previously (4, 6) to improve volumetric coverage. First, non-ECG-triggered scout images in coronal, transverse, and sagittal orientations were acquired to plan subsequent images and to localize the two-dimensional selective navigator. At 7 T, the navigator was placed at the lung-heart interface because of the limited sensitive volume of the surface coil. Second, ECG-triggered, breath-hold multisection transverse cine scout imaging was performed for both the determination of the period of minimal coronary motion (trigger delay) and the volume targeting of the 3D stack in parallel with the middiastolic RCA. Finally, volume-targeted coronary MR angiography was performed by using a 3D segmented k-space gradient-echo imaging technique (parameters are in Table 1) combined with a spectrally selective adiabatic inversion-recovery pulse (inversion time, 200 msec) for fat saturation. First-order local volume shimming at the anatomic level of the RCA was performed in all cases.



Figure 1:RF coil

Custom-built quadrature RF transmit-receive surface coil consisting of two 13-cm elements used for our study at 7 T.

Imaging at 3 T

On the 3 T system, the body coil was used for RF transmission, with a commercial six-element cardiac coil array for signal reception. Scout imaging included free-breathing, retrospectively ECG-gated, two-dimensional cine balanced fast gradient-echo imaging in a horizontal long-axis view (four-chamber) to determine the trigger delay. Furthermore, ECG-triggered free-breathing navigator-gated and corrected 3D gradient-echo whole-heart imaging was performed for the anatomic localization of the RCA. After scout imaging, two coronary imaging sequences were performed at 3 T with different naviga-

tor localization in random order: (a) with navigator localization at the lung-heart interface (navigator at heart) and (b) with navigator localization at the lung-liver interface (navigator at liver). Both 3 T coronary imaging sequences consisted of a 3D segmented k-space gradient-echo technique with spectrally selective adiabatic inversion recovery (inversion time, 150 msec) for fat saturation. The coronary MR angiography imaging parameters were similar (Table 1) at both field strengths to support a fair quantitative comparison.

Table 1: Imaging Parameters at 7 T and 3 T Coronary MR Angiography			
Field strength	7 Tesla	3 Tesla	3 Tesla
Sequence	3D gradient echo	3D gradient echo	3D gradient echo
Navigator position/correction factor	Lung-Heart interface / 1.0	Lung-Heart interface / 1.0	Lung-Liver interface / 0.6
Coil	Quadrature two-element surface coil transmit/receive	Body coil transmit / six-element phased array receive	Body coil transmit / six-element phased array receive
Fat suppression	Adiabatic SPIR	Adiabatic SPIR	Adiabatic SPIR
TR (ms)	4.3	4.3	4.3
TE (ms)	1.38	1.38	1.38
TI (ms)	200	150	150
Acquired voxel size (mm³)	0.82x0.86x2.00	0.82x0.86x2.00	0.82x0.86x2.00
Reconstructed voxel size (mm³)	0.82x0.82x1.00	0.82x0.82x1.00	0.82x0.82x1.00
Number of slices	30	30	30
Field of view (mm²)	420x268	420x269	420x269
Matrix	512x312	512x312	512x312
Flip angle (°)	15	15	15
Acquisition window (ms)	107	108	108

Data Analysis

Images were processed and analyzed by using the Soap-Bubble tool (9). Both a visual qualitative description and a direct quantitative comparison between 7 T and 3 T images were performed. All data analyses were performed by one physician (S.G.C.v.E., with 4 years of experience in cardiac MR

imaging) with the supervision of a senior researcher (M.S., with 18 years of experience in cardiac MR imaging).

The following parameters were measured: contrast-to-noise ratio (CNR) between the blood pool and the epicardial fat, signal-to-noise ratio (SNR) of the blood pool, RCA vessel sharpness and diameter of the first 4 cm, and visible vessel length. The CNR was defined as the difference in signal intensity between a manually placed region of interest (ROI) in the aortic root (mean ROI area, $1.80 \text{ cm}^2 \pm 0.60$) near the offshoot of the RCA, and that of an ROI placed in the epicardial fat adjacent to the proximal RCA (mean ROI area, $0.90 \text{ cm}^2 \pm 0.61$), divided by the standard deviation of the background signal from an ROI positioned anterior to the chest wall (noise; mean ROI area, $9.95 \text{ cm}^2 \pm 3.98$). The SNR was calculated for the blood signal intensity in the described ROI localized in the aortic root. The average signal intensity from this ROI was divided by the noise. Vessel sharpness was measured by using signal intensity gradients perpendicular to the 3D course of the RCA and was calculated for the proximal 4 cm of the RCA (9). The RCA vessel length was measured manually, and both vessel sharpness and diameter for the proximal 4 cm of the RCA were calculated automatically by the software.

Statistical Analysis

Data are presented as mean \pm standard deviation. Comparisons were made between the results obtained at 7 T and 3 T and between the results obtained with the different navigator positions at 3 T. For comparisons, a non-parametric Mann-Whitney U test was used. $P < .05$ was considered to indicate a statistically significant difference.

RESULTS

Coronary MR angiography was performed successfully in all volunteers at both field strengths. At 7 T, one study volunteer complained about vertigo while the table was moving. All quantitative findings are listed in Table 2. Total time in the magnet was on average 30 minutes at 7 T and 20 minutes at 3 T.

Figures 2–4 illustrate example coronary MR angiography reformations obtained at 7 T and at 3 T. All images show high signal intensity of the coronary artery lumen, while that of the surrounding epicardial fat is suppressed. At 7 T, suppression of the epicardial fat appears visually improved when compared with that at 3 T (Fig 2). Consistent with these findings, quantitative CNR between the blood pool and epicardial fat was significantly improved at 7 T

(7 T versus 3 T navigator at heart, P = .013; 7 T versus 3 T navigator at liver, P = .009).

Table 2: Quantitative results obtained from 10 healthy volunteers

	7 Tesla, navigator on lung-heart	3 Tesla, navigator on lung-heart	3 Tesla, navigator on lung-liver
CNR	87.5 ± 33.9*	51.7 ± 12.7	47.8 ± 15.2
SNR blood pool	109.2 ± 46.9*	66.9 ± 19.4	67.2 ± 24.9
RCA vessel sharpness (%)	58.3 ± 8.9*	49.7 ± 5.1	48.9 ± 7.5
RCA vessel length (cm)	7.24 ± 2.34	8.21 ± 2.19	7.99 ± 2.73
RCA diameter, first 4 cm (mm)	2.97 ± 0.27	3.07 ± 0.38	3.07 ± 0.37
Navigator efficiency (%)	54 ± 20	53 ± 20	46 ± 14
Acquisition time (sec)	469 ± 225	410 ± 180	470 ± 191
Heart rate (beats / min)	70 ± 15	67 ± 10	69 ± 10

* significantly different from 3 T (p<0.05). CNR: contrast-to-noise ratio between proximal coronary blood pool and surrounding perivascular tissue; RCA: right coronary artery; SNR: signal-to-noise ratio

Visually, the contrast between the myocardium and the blood pool in the left ventricle is rather shallow at 7 T as shown in Figures 3 and 4.4. When compared with that at 3 T, the SNR of the blood pool measured on the 7 T images was 60% higher (7 T versus 3 T navigator at heart, P = .023; 7 T versus 3 T navigator at liver, P = .027). Improved delineation of the RCA at 7 T is visible in Figure 3, with good depiction of RCA branches and distal segments. Consistent with these findings, objective vessel sharpness analysis demonstrated improved quantitative vessel conspicuity at 7 T (versus 3 T navigator at heart, P = .038; versus 3 T navigator at liver; P = .031). Even though constraints related to the B1 field and coil sensitivity adversely affected the signal more distant to the surface transmit-receive coil at 7 T (Figs 2–4), there was no significant difference in vessel length (7 T versus 3 T navigator at heart, P = .233; 7 T versus 3 T navigator at liver, P = .414) or vessel diameter (7 T versus 3 T navigator at heart, P = .653; 7 T versus 3 T navigator at liver, P = .567) measurements among the images from the different field strengths. Navigator efficiency (7 T versus 3 T navigator at heart, P = .970; 7 T versus 3 T navigator at liver, P = .272) and total data acquisition time (7 T versus 3 T

navigator at heart, $P = .520$; 7 T versus 3 T navigator at liver, $P = .821$) also were not field strength dependent. No significant difference in CNR between the blood pool and epicardial fat, SNR of the blood pool, RCA vessel sharpness, vessel length, vessel diameter, navigator efficiency, or acquisition time was found between the 3 T images acquired with the different navigator localizations.

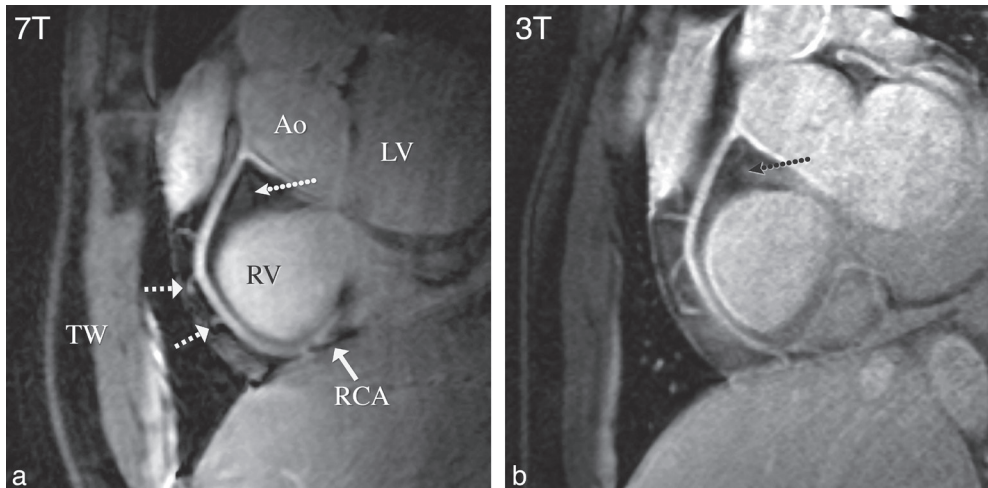


Figure 2: Coronary MR angiograms of the RCA.

Obtained at (a) 7 T and (b) 3 T in the same healthy 18-year-old man (double oblique volume targeted plane parallel to the RCA). Improved suppression of the epicardial fat (long dotted arrow) with high contrast between the blood and epicardial fat is visible at 7 T. At both field strengths, a number of small branching vessels are depicted (short dashed arrows). Also at 7 T, a long portion of the RCA is visible (solid arrow = distal part of RCA). Ao = aortic root, LV = left ventricle, RV = right ventricle, TW = thoracic wall.

DISCUSSION

In our study comparing 7 T and 3 T RCA coronary MR angiography in young healthy volunteers, we found improved CNR between the blood pool and the epicardial fat, enhanced SNR of the blood pool, and increased vessel sharpness at 7 T. These findings may have implications, since vessel conspicuity and well-defined borders of the coronary arteries support improved identification of significant coronary artery stenoses.

The results of a multicenter study indicate that multidetector computed tomography (CT) is highly promising and superior to MR angiography for the noninvasive evaluation of significant proximal coronary stenoses (10). However, the most recent data from a coronary MR angiography multicenter trial (11) demonstrate substantial progress, and further improvement in SNR di-

agnostic quality approaching that of CT angiography may be expected soon; therefore, the development of new MR imaging methodology at higher magnetic field strength is of particular interest.

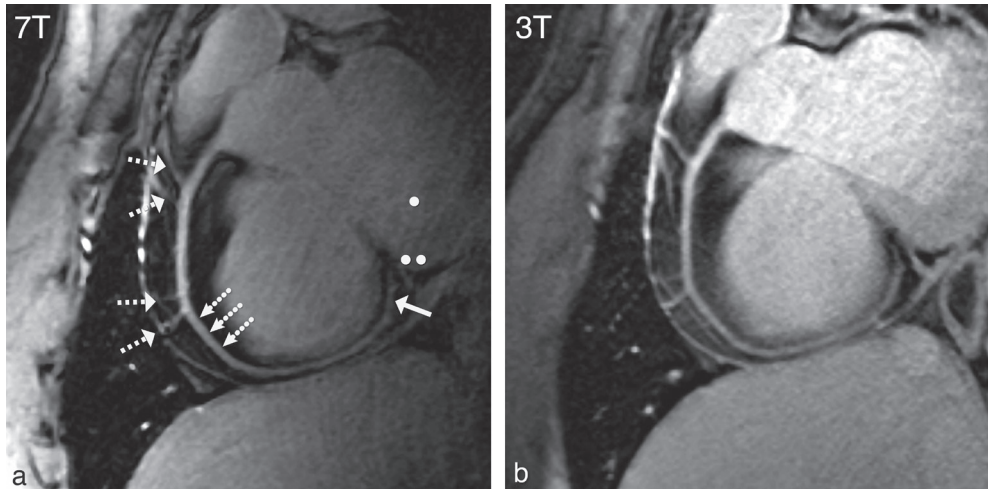


Figure 3: Coronary MR angiograms of the RCA.

Double oblique volume targeted plane parallel to the RCA in a healthy 26-year-old man display a high visual vessel definition (dotted arrows) in (a) the 7 T image compared with that at (b) 3 T. At 7 T, contrast is limited between the myocardium (.) and the blood pool (..). Multiple RCA side branches (dashed arrows) and distal parts of the RCA (solid arrow) are depicted clearly at both field strengths.

Approximately a twofold increase in SNR is predicted at 7 T when compared with 3 T (7, 12), whereas a 60% SNR improvement was found in our study, which may be explained with the prolonged T_1 at 7 T and the depth penetration of the RF transmit-receive coil, which was clearly inferior to that at 3 T. However, a significant 60% increase in SNR with a simple coil design is encouraging and emphasizes the need for further developments in coil technology. Recent advances in RF transmit arrays (2, 3) are a step in this direction. Findings from previous studies in which investigators compared 1.5 T and 3 T coronary MR angiography (13–15) clearly demonstrated that the expected 100% improvement in SNR could not be obtained. At 7 T, the lack of commercially available RF coils and the only recent availability of 7 T for whole-body human use constitute additional 7 T–specific limitations. Despite these limitations, the reported 60% improvement in SNR, when going from 3 T to 7 T, is consistent with that reported for direct 1.5 T versus 3 T.

Our findings of increased vessel sharpness at 7 T suggest that motion suppression works effectively at 7 T, since vessel sharpness depends on the performance of ECG triggering and the respiratory navigator. Two similar ima-

ging sequences with different navigator localizations were performed at 3 T to exclude the influence of navigator localization on the quantitative parameters related to image quality. Consistent with earlier findings (16), no navigator-dependent quantitative differences were observed.

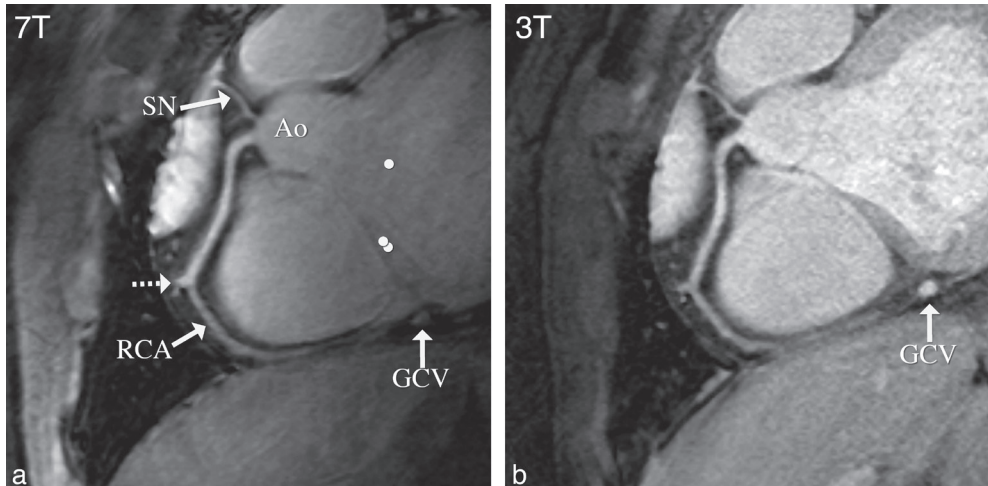


Figure 4: Sinoatrial nodal artery (SN) and a proximal branch of the RCA.

Image obtained in a double oblique volume targeted plane parallel to the RCA in a healthy 28-year-old man. (a) At 7 T, there is not much difference in signal intensity between the blood pool (.) and the myocardium (..). (b) At 3 T, this contrast is slightly improved. On b , the great cardiac vein (GCV) can be identified easily, but this structure is less visible on a , likely because of shortened T2* at 7 T, as well as limited surface coil RF penetration. Ao = aortic root, dashed arrow = RCA side branch.

The results from the RCA vessel length and diameter measurements were similar for both field strengths. This finding suggests that coverage and RF penetration of the surface coil at 7 T may not be limiting factors for visualization of the RCA.

The situation for the left coronary system is different. On the one hand, the penetration depth of the current transmit-receive coil is limited, so parts of the left coronary system may not be visualized easily. On the other hand, an enhancement of the contrast between myocardium and the blood pool is mandatory for visualizing the left coronary system. At 3 T, such contrast enhancement has been obtained with adiabatic T₂ preparation (17) or with the combination of extracellular contrast agents and inversion recovery (18). However, at 7 T, specific absorption rate constraints preclude the use of the T₂ preparation, and alternative 7 T–specific solutions with or without contrast agents remain to be explored. Finally, although a 60% increase in SNR was obtained at 7 T, we have not used this gain for increased spatial resolu-

tion. However, the objective of our work was a direct, quantitative, objective comparison with 3 T.

In conclusion, although substantial challenges are associated with 7 T cardiac MR imaging, a number of them have been addressed successfully. In our study directly comparing in vivo human imaging of the RCA at 7 T and 3 T in young healthy volunteers, quantitative parameters related to image quality attained at 7 T equal or surpass those from 3 T. Our results clearly warrant further evaluation in patients with coronary artery disease to assess the potential of our 7 T approach for the visualization of luminal RCA disease. Future work will concentrate on refinements in coil technology and contrast generation to support concomitant imaging of the left coronary system.

ACKNOWLEDGMENTS

Supported by the Dutch Organization for Scientific Research (Nederlandse Organisatie voor Wetenschappelijk Onderzoek [NWO]).

REFERENCES

1. Maderwald S, Orzada S, Schäfer LC, Bitz AK, Brote I, Kraff O, Theysohn JM, Ladd ME, Ladd SC, Quick HH. 7T Human in vivo cardiac imaging with an 8-channel transmit/receive array. In: Proceedings of the 17th Annual Meeting of ISMRM. 2009.
2. Snyder CJ, DelaBarre L, Metzger GJ, Moortele P-F van de, Akgun C, Ugurbil K, Vaughan JT. Initial results of cardiac imaging at 7 tesla. *Magnetic Resonance in Medicine* 2009 ;61:517–524.
3. Vaughan JT, Snyder CJ, DelaBarre LJ, Bolan PJ, Tian J, Bolinger L, Adriany G, Andersen P, Strupp J, Ugurbil K. Whole-body imaging at 7T: Preliminary results. *Magnetic Resonance in Medicine* 2009 ;61:244–248.
4. Versluis MJ, Tsekos N, Smith NB, Webb AG. Simple RF design for human functional and morphological cardiac imaging at 7 tesla. *Journal of Magnetic Resonance* 2009 ;200:161–166.
5. Frauenrath T, Hezel F, Heinrichs U, Kozerke S, Utting JF, Kob M, Butenweg C, Boesiger P, Niendorf T. Feasibility of cardiac gating free of interference with electromagnetic fields at 1.5 Tesla, 3.0 Tesla and 7.0 Tesla using an MR-stethoscope. *Invest Radiol* 2009 ;44:539–547.
6. Elderen SGC van, Versluis MJ, Webb AG, Westenberg JJM, Doornbos J, Smith NB, Roos A de, Stuber M. Initial results on in vivo human coronary MR angiography at 7 T. *Magnetic Resonance in Medicine* 2009 ;62:1379–1384.
7. Wen H, Denison TJ, Singerman RW, Balaban RS. The intrinsic signal-to-noise ratio in human cardiac imaging at 1.5, 3, and 4 T. *J. Magn. Reson.* 1997 ;125:65–71.
8. Fischer SE, Wickline SA, Lorenz CH. Novel real-time R-wave detection algorithm based on the vectorcardiogram for accurate gated magnetic resonance acquisitions. *Magn Reson Med* 1999 ;42:361–370.
9. Etienne A, Botnar RM, Muiswinkel AMC van, Boesiger P, Manning WJ, Stuber M. Soap-Bubble visualization and quantitative analysis of 3D coronary magnetic resonance angiograms. *Magnetic Resonance in Medicine* 2002 ;48:658–666.
10. Miller JM, Rochitte CE, Dewey M, Arbab-Zadeh A, Niinuma H, Gottlieb I, Paul N, Clouse ME, Shapiro EP, Hoe J, Lardo AC, Bush DE, de Roos A, Cox C, Brinker J, Lima JAC. Diagnostic performance of coronary angiography by 64-row CT. *N. Engl. J. Med.* 2008 ;359:2324–2336.
11. Kato S, Kitagawa K, Ishida N, Ishida M, Nagata M, Ichikawa Y, Katahira K, Matsumoto Y, Seo K, Ochiai R, Kobayashi Y, Sakuma H. Assessment of coronary artery disease using magnetic resonance coronary angiography: a national multicenter trial. *J. Am. Coll. Cardiol.* 2010 ;56:983–991.
12. Vaughan JT, Garwood M, Collins CM, Liu W, DelaBarre L, Adriany G, Andersen P, Merkle H, Goebel R, Smith MB, Ugurbil K. 7T vs. 4T: RF power, homogeneity, and signal-to-noise comparison in head images. *Magn Reson Med* 2001 ;46:24–30.
13. Bi X, Deshpande V, Simonetti O, Laub G, Li D. Three-dimensional breathhold SSFP coronary MRA: a comparison between 1.5T and 3.0T. *J Magn Reson Imaging* 2005 ;22:206–212.
14. Sommer T, Hackenbroch M, Hofer U, Schmiedel A, Willinek WA, Flacke S, Gieseke J, Träber F, Fimmers R, Litt H, Schild H. Coronary MR angiography at 3.0 T versus that at 1.5 T: initial results in patients suspected of having coronary artery disease. *Radiology* 2005 ;234:718–725.

15. Yang PC, Nguyen P, Shimakawa A, Brittain J, Pauly J, Nishimura D, Hu B, McConnell M. Spiral magnetic resonance coronary angiography--direct comparison of 1.5 Tesla vs. 3 Tesla. *J Cardiovasc Magn Reson* 2004 ;6:877–884.
16. Stuber M, Botnar RM, Danias PG, Kissinger KV, Manning WJ. Submillimeter three-dimensional coronary MR angiography with real-time navigator correction: comparison of navigator locations. *Radiology* 1999 ;212:579–587.
17. Botnar RM, Stuber M, Danias PG, Kissinger KV, Manning WJ. Improved coronary artery definition with T2-weighted, free-breathing, three-dimensional coronary MRA. *Circulation* 1999 ;99:3139–3148.
18. Bi X, Li D. Coronary arteries at 3.0 T: Contrast-enhanced magnetization-prepared three-dimensional breathhold MR angiography. *J Magn Reson Imaging* 2005 ;21:133–139.

4

Improved Signal-to-Noise in Proton Spectroscopy of the Human calf Muscle at 7 Tesla Using Localized B_1 Calibration

*Maarten J. Versluis
Hermien E. Kan
Mark A. van Buchem
Andrew G. Webb*

ABSTRACT

Large variations of tip angle within a slice can lead to suboptimal pulse power optimization using standard techniques, which measure the average tip angle over a slice: this effect is especially pronounced at fields of 7 T and above. A technique is introduced that performs a volume-selective power optimization in less than 10 seconds, and automatically calibrates the radio-frequency (RF) pulses for subsequent spectroscopy scans. Using this technique, MR spectra were acquired in the human calf of seven healthy volunteers with a partial volume Tx / Rx coil. Increases in signal-to-noise-ratio (SNR) based upon the unsuppressed water signal between $22 \pm 5\%$ and $166 \pm 42\%$, compared to spectra obtained with the conventional power calibration technique, were measured in different regions of the calf muscle. This new technique was able to measure the inhomogeneous RF field at 7 T and resulted in a considerable SNR increase.

INTRODUCTION

Human MRI at high magnetic fields, i.e., 7T and above, has to overcome a large variation in the strength of the radiofrequency field (B_1) over the imaging volume. The primary, intrinsic reason is that the wavelength of the corresponding radiofrequency (RF) excitation and reception is less than, or comparable to, the dimensions of the body. The second, more practical reason is that the lack of a body coil, particularly on commercial systems, leads to a more frequent use of local Tx / Rx surface coils than at lower field. Both of these factors result in accurate tip angle calibration techniques being very important for obtaining the optimal SNR. Conventional methods used commonly at lower field strengths, which measure the tip angle averaged over a slice or over the complete sensitive volume of the coil (1, 2) lead to suboptimal results at high field, as outlined by a recent article on 7 T cardiac imaging (3).

Many different approaches have been proposed for B_1 mapping, including those based on repeated measurements with different tip angles (4–6), different repetition times (7), measuring the ratio between the signal intensity from spin echoes and stimulated echoes (1, 2, 8, 9), and detecting tip angle related phase changes (10). These methods can be divided in two categories: first, those that use gradients to encode the entire volume and calculate the tip angle on a pixel-by-pixel basis (4–10), and second, those that measure the tip angle over a large volume using non-selective, or slice-selective RF pulses (1, 2). Methods in the first category tend to be lengthy procedures and are therefore not suitable for use as a calibration sequence in a clinical setting. Methods in the second category are fast but lead to inaccurate results when the B_1 distribution is very inhomogeneous.

In this work, a simple technique is introduced that measures the tip angle in a small volume of interest (VOI) using four slice-selective RF pulses. The method, which we have called volume-selective power optimization (PO_{volume}), measures the ratio of the signal from two stimulated echoes (STE) to calculate the average tip angle in the VOI. The optimal value is found by an iterative approach, and this value is used to automatically calibrate the RF amplifier. Since only a small volume is measured, the technique is very fast (2s per iteration). Experiments such as single voxel spectroscopy are expected to benefit most because of the high sensitivity of the signal intensity to suboptimal power settings of the three RF pulses used for localization.

In this study, we compared the SNR of localized MR spectra in the calf acquired with this new technique with a conventional three pulse calibration

technique (PO_{slice}), the standard on most commercial MR systems that averages the measured tip angle over a slice through the center of the VOI (2).

METHODS

All experiments were performed on a commercial 7 T Philips Achieva MRI scanner (Philips Healthcare, Best, The Netherlands). A quadrature half-volume Tx/Rx coil was constructed for the human calf. Two square loops of dimensions 10 cm were constructed from copper tape (1 cm wide, 25 μm thick), which was fixed to a flexible Teflon former (2 mm thickness). The loops were capacitively split into sections ~ 5 cm in length, corresponding to $1/20^{\text{th}}$ of the RF wavelength at 7 T. The two loops were overlapped by $\sim 10\%$ to minimize mutual inductance. Balanced impedance matching using variable capacitors and a lattice balun were used for each excitation port, which were fed from the quadrature outputs of the Philips transmit/receive interface box. The entire coil assembly was mounted on a rigid semi-cylindrical plexiglass former (thickness 5 mm, inner diameter 15 cm). A layer of foam, ~ 1 cm thick, was placed inside the cylinder, and the subject's lower leg lay on top of this foam layer.

Subjects

Seven volunteers (6 males, 1 female, age 37 ± 9 years) were scanned and localized spectra were obtained at multiple locations with respect to the coil. In addition, a B_1 map was obtained from one volunteer to show the RF homogeneity of the coil. Informed consent was obtained from all subjects in accordance with guidelines of the local medical ethics committee.

Calibration sequence

The power of the RF amplifier was calibrated by measuring the tip angle in a VOI using the ratio of the signal intensities from two stimulated echoes for the four-pulse sequence shown in Figure 1. A three-dimensional volume was selected using four slice-selective RF pulses. The first three pulses were applied with the gradients in orthogonal directions, with the fourth RF pulse applied simultaneously with the gradient in the same direction as during the third RF pulse. The resulting stimulated echo signals were acquired. All other free induction decay and echo pathways were carefully spoiled using crusher gradients.

The ratio of the two STE signals, I_{STE2} and I_{STE1} , is given by (11):

$$\frac{I_{STE_2}}{I_{STE_1}} = \frac{\sin\alpha_3 \cos\alpha_2 \exp\left(\frac{-(\tau_2 + \tau_3)}{T_1}\right)}{\sin\alpha_2 \exp\left(\frac{-\tau_2}{T_1}\right)} \quad [1]$$

where α_i denotes the RF pulse angle for the different pulses, and τ_i denotes the time at which each RF pulse is applied. When α_2 equals α_3 Eq. [1] reduces to:

$$\frac{I_{STE_2}}{I_{STE_1}} = \cos\alpha_2 \exp\left(\frac{-\tau_3}{T_1}\right) \quad [2]$$

The value of τ_3 is chosen such that $\tau_3 \ll T_1$ (12). Therefore the tip angle can be accurately estimated for the selected volume using the following equation:

$$\alpha_2 \approx \cos^{-1}\left(\frac{I_{STE_2}}{I_{STE_1}}\right) \quad [3]$$

For the pulse sequence in Figure 1, the maximum signal intensity for the STE₂ signal occurs when the tip angle for α_0 and α_1 is 90°, and 45° for α_2 and α_3 .

The volume for the PO_{volume} was identical to the VOI of the spectroscopy experiment that followed the calibration sequence. The following parameters were used: repetition time (TR) / TE_{STE1} / TE_{STE2} = 2000 ms / 31 ms / 51 ms. The tip angle in the VOI was calculated online and was used for the next iteration to set the RF amplifier. When the measured tip angle deviated more than 3 degrees from the requested tip angle a new iteration was performed with updated settings based on the last iteration: a maximum of 5 iterations was used to reach the desired tip angle. Regions with low signal can lead to an invalid signal ratio ($I_{STE_2} / I_{STE_1} > 1$) due to noise influences. These values were not accepted and the sequence was performed again with higher RF amplifier power settings; in this way each region produced results consistent with equation [3].

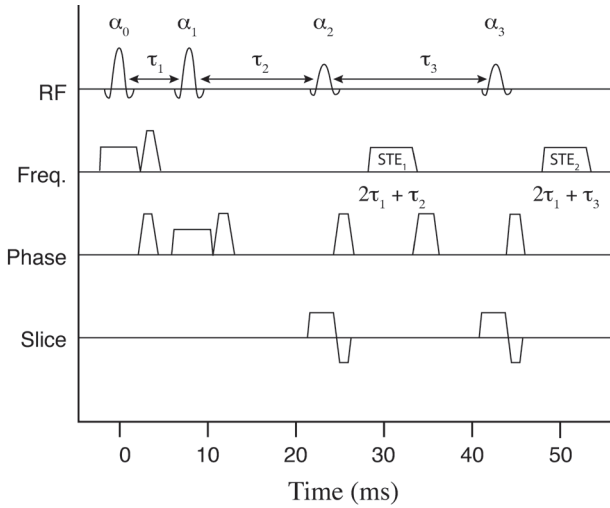


Figure 1: Sequence diagram of the volume selective RF calibration technique.

A volume is selected using four RF pulses and gradients. Targeted angles for maximum signal intensity of STE_2 are $\alpha_0 = \alpha_1 = 90^\circ$ and $\alpha_2 = \alpha_3 = 45^\circ$. Two stimulated echoes are acquired (STE_1 and STE_2) at times $2\tau_1 + \tau_2$ and $2\tau_1 + \tau_3$ respectively, while the spin-echo and free induction decay pathways are spoiled using crusher gradients on all three axes. The intervals between the RF pulses are: $\tau_1 = 8$ ms, $\tau_2 = 15$ ms and $\tau_3 = 19.5$ ms.

The sequence was performed twice, both before and after shimming and determination of the water resonance frequency (f_0). Both shimming and f_0 determination were performed using adiabatic pulses, which are relatively insensitive to variations in RF power. Image based shimming (13) as provided by the manufacturer was used for regions where conventional shimming failed.

The conventional slice-selective calibration method was measured with the slice oriented along the slice selection direction of the VOI, which was, depending on the exact orientation of the voxel, approximately perpendicular to the coil.

Localized spectroscopy

The new calibration technique was evaluated in several stimulated echo acquisition mode (STEAM) MR spectra of the calf muscle. The following scan parameters were used: $10 \times 10 \times 10$ mm³ voxel, TR = 2000 ms, mixing time (TM) = 25 ms, echo time (TE) = 25 ms, 64 averages. The total scan duration including optimization of the water suppression was approximately 4 minutes, a clinically acceptable timeframe for patient studies. The coil was placed on the posterior side of the leg and positioned approximately at the location of the largest circumference of the calf. MR spectra were obtained at different

locations in the calf muscles, one set using the standard power calibration sequence over the entire slice, and the other set with the new four-pulse volume-selective calibration technique. In addition, for both scans a non-water suppressed scan with the same settings as the water suppressed scan was acquired to measure SNR using eight averages. The VOIs for the spectroscopy scans were positioned in the central zone of the soleus muscle (SOL), the medial side of the gastrocnemius muscle (GM) and in two different locations in the medial side of the soleus muscle (SM) based on a T_1 -weighted anatomical image acquired with the following parameters: TR / TE / flip angle (FA) = 300 ms / 5.2 ms / 30° , voxel = $0.5 \times 0.5 \times 4 \text{ mm}^3$, field-of-view (FOV) = $180 \times 180 \times 66 \text{ mm}^3$, 15 slices, scan duration is two minutes.

The spectra were viewed in jMRUI (14) and the AMARES algorithm (15) was used to fit the water peak based on a Lorentzian line shape. The SNR of the spectra was measured by dividing the integrated area under the fitted water peak of the non-water-suppressed scans by the standard deviation of the last 200 points of the time-domain signal, which contained only noise. The water signal was chosen because the intensity is much larger than that of any metabolite and since residual dipolar couplings and bulk susceptibility effects can hamper accurate quantification of metabolite signals in muscle (16).

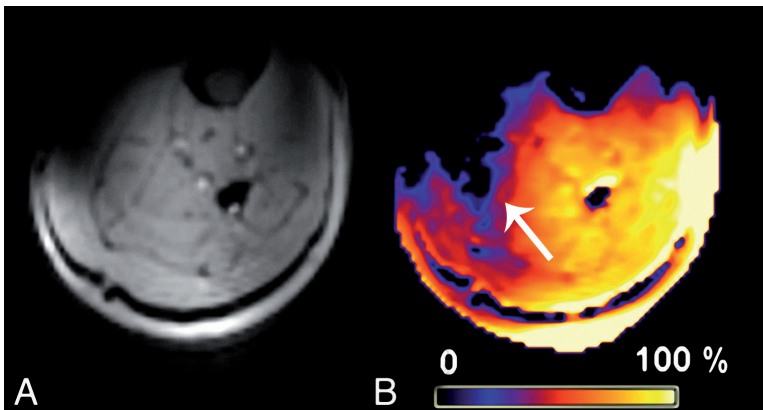


Figure 2: Coverage and B_1 -profile of coil.

The left image (a) shows a single slice from a low resolution 3D gradient echo sequence of the calf muscle. The right image (b) shows the corresponding B_1 map scaled as a percentage of the target B_1 . There is substantial variation of B_1 over the leg as would be expected for the partial volume Tx / Rx coil that was used in the experiments. Especially towards the medial side of the leg the B_1 inhomogeneity is particularly pronounced as depicted by the arrow.

B₁ mapping

A B_1 map was acquired using a 3D spoiled gradient echo sequence with two interleaved repetition times (TR_1 and TR_2) with the following parameters: $TR_1 / TR_2 / TE / FA = 20 \text{ ms} / 100 \text{ ms} / 1.8 \text{ ms} / 30^\circ$, voxel = $2 \times 2 \times 4 \text{ mm}^3$, FOV = $180 \times 180 \times 116 \text{ mm}^3$, total scan duration is two-and-a-half minutes. The ratio of the resulting images with different TR yields a tip angle distribution map (7).

RESULTS

Figure 2 shows a single slice from the 3D B_1 map illustrating that the tip angle varies considerably over the field-of-view, and that the excitation pattern is not symmetric. The latter observation is in line with several previous studies carried out at high field (17). The sensitive region of the coil is large enough to almost completely cover the soleus and gastrocnemius muscles, and the tip angle varies by more than a factor-of-two over this region. Toward the SM on the medial side of the leg there is a region where the B_1 inhomogeneity is particularly pronounced. Differences were found in the result of the calibration sequence before and after f_0 determination and shimming when the VOI was moved from the SOL to the SM.

Figure 3a shows the approximate locations of three volumes from which localized spectra were obtained. For all volunteers, the PO_{volume} calibration sequence iteratively arrived at the desired pulse angle for the selected volume. At the location of the SM conventional volume shimming failed due to the high B_1 inhomogeneities, therefore image based shimming was used. MR spectra in the SM were acquired at two different locations within the same volunteer because of the high variability in B_1 in that region. Increases in SNR were found in all locations when compared to the standard PO_{slice} technique. The amount of SNR increase was dependent on the location with respect to the coil. Representative spectra from the SOL are shown in figure 3b and spectra from the SM are shown in figure 3c. The bottom spectrum is acquired with the PO_{slice} technique, whereas the one at the top is acquired with the PO_{volume} technique. The PO_{volume} technique results in an increase in SNR of 24% and 224% for SOL and SM, respectively, in this volunteer, based upon the unsuppressed water signal.

Figure 4 shows the SNR increases averaged over all volunteers for different regions in the calf muscles. The measured increases in SNR were $34 \pm 5\%$ in the GM, $22 \pm 5\%$ in the SOL and $166 \pm 42\%$ in the SM based upon the unsuppressed water signal.

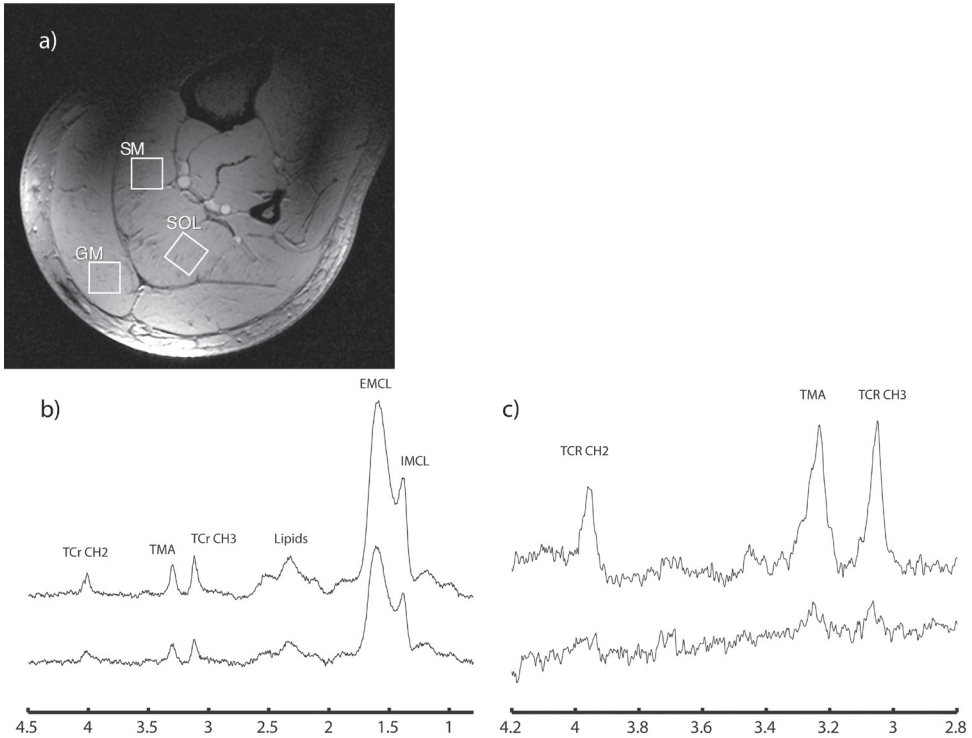


Figure 3: Anatomic image and acquired MR spectra.

(a) T_1 -weighted anatomical image for reference showing the locations where the MR spectra were obtained. (b) Localized MR spectra of the SOL of a volunteer, top: PO_{volume} , bottom: PO_{slice} . (c) Localized MR spectra of the SM, top: PO_{volume} , bottom: PO_{slice} . Note the clear increase in SNR of the spectra from the new volume-selective power optimization method. Based on the signal intensity of the water peak (not displayed) an SNR increase of 24% was found in (b) and 224% in (c). Scan parameters: STEAM sequence, $10 \times 10 \times 10 \text{ mm}^3$ voxel, $TR/TM/TE = 2000 \text{ ms}/25 \text{ ms}/25 \text{ ms}$, 64 averages. Volumes were placed in the central zone of the soleus muscle (SOL), the medial side of the gastrocnemius muscle (GM) and the medial side of the soleus muscle (SM).

DISCUSSION

Partial volume Tx/Rx coils are consistently used for studies at high field (18), particularly those aimed at very high spatial resolution and/ or reduced specific absorption rate. In addition to the intrinsic non-uniformity of the B_1 field from such coils, asymmetries in the transmit field are induced by the interaction of the RF field with the dielectric properties of the tissue. The resulting B_1 fields are not easy to predict, and so experimental procedures for optimizing local tip angles are important. Since most MRS studies involve multiple-pulse localized spectroscopy experiments, sub-optimal pulse calibration in the volume of interest can reduce signal intensities significantly.

This is particularly important in clinical studies, where total data acquisition times are typically limited both by institutional review boards and by patient comfort. Using a new four-pulse volume-selective optimization method consistent increases in SNR of the MR spectra were found compared to the standard slice-selective method (1, 2). When the tip angle is averaged over a large area the calibration is strongly biased toward the area with the highest B_1 , which is not necessarily near the VOI. This is particularly true for partial volume and surface Tx/Rx coils, which have a highly non uniform excitation profile. Using the four-pulse volume-selective optimization method we were able to locally measure the B_1 field. In contrast to many other B_1 mapping procedures (4–10) only signal originating from the VOI was acquired and therefore the calculations required for iterative convergence to the optimal tip angle are simple and can be performed real-time. The procedure was fast enough (less than 10 s) to be used as a calibration sequence before the actual MRS sequence.

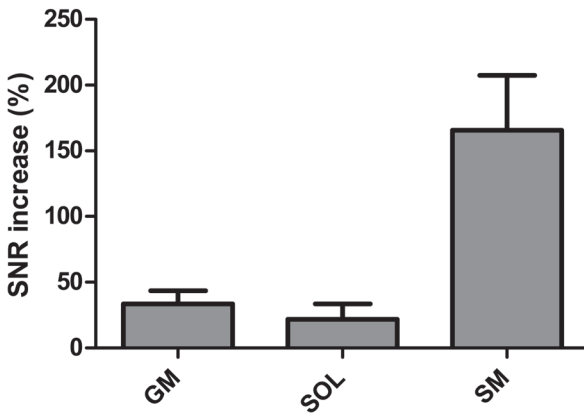


Figure 4: SNR comparisons of the unsuppressed water spectra.

Spectra were acquired in different locations in the calf muscle, GM ($n = 4$), SOL ($n = 5$) and SM ($n = 4$) subjects. For the SM two different locations within the same volunteer were measured. A large variation in SNR increase was measured in the SM because of the very high B_1 inhomogeneities at that location. The SNR was determined using the area under the water peak of a non-water suppressed spectrum divided by the standard deviation of the last 200 points of the time signal. Error bars represent standard error of the mean.

The technique is valid under the assumption that T_1 decay between the two stimulated echoes can be neglected. This is usually valid in vivo where T_1 values of tissue are typically two orders of magnitude larger than the time between the first and second stimulated echo signal (12, 19). Therefore, the method is not only limited for use in the calf muscle but could also be used in the human brain. However if the technique is applied in tissues with very

short T_1 values such as fat, it may be necessary to correct for the T_1 decay during the calibration sequence. Both stimulated echo signals have identical T_2 decay, and therefore no errors are introduced for tissues with different T_2 values. However tissues with very short T_2 values will result in lower SNR and therefore increase the difficulty in obtaining a reliable tip angle estimation. The TE of the calibration sequence was 16 ms which was short enough to reliably measure signal in the human calf muscle.

The first iteration of the volume-selective technique is performed using the f_0 and shim settings of the previous scan. Therefore a large change in the location of the VOI can lead to a large change in f_0 and shim settings. This was the case when the VOI was moved from the SOL to the SM, and so it was necessary to repeat the PO_{volume} sequence again after shimming and frequency adjustment

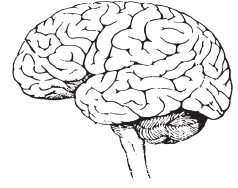
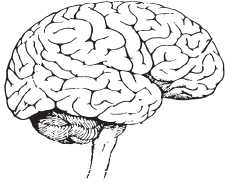
The SNR gain for the SOL was measured to be the smallest compared to the other two locations. This part of the muscle is located in a rather homogeneous sensitivity region of the coil and the difference between PO_{slice} and PO_{volume} is therefore small, but nevertheless significant, corresponding to a reduction in scan time of approximately 40% to achieve a given SNR. The GM is located closer to the coil but within a more inhomogeneous region and consequently a larger SNR increase is both expected and measured when comparing the two techniques. The B_1 inhomogeneity around the SM is very pronounced and therefore the largest SNR increases are found in this region because the slice-selective power calibration method is not able to accurately measure the local B_1 field. The increase in SNR in the SM is therefore also strongly dependent on the exact location of the VOI, but is typically substantial. The reported SNR increases are measured using the unsuppressed water signals for improved accuracy: however, the metabolite SNR should increase proportionally given the similar relaxation properties of the metabolites and water (12). Visual inspection of the spectra in the figures does indeed show this increase.

In summary, increases of up to 166% in SNR based upon the unsuppressed water signal were found in calf spectra of five healthy volunteers. This results in significant reduction in scan time, while maintaining the same SNR, an important factor when obtaining spectra in a clinical setting. Even with “homogeneous” transmit coils, the variation in tip angles is known to be pronounced and patient-specific, and so simple experimentally-based power optimization schemes are valuable in realizing the full signal-to-noise potential of high field.

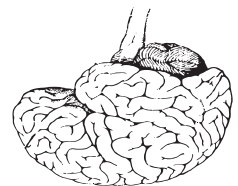
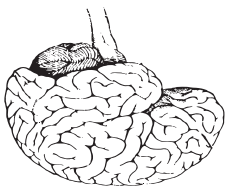
REFERENCES

1. Carlson JW, Kramer DM. Rapid radiofrequency calibration in MRI. *Magn Reson Med* 1990 ;15:438–45.
2. Perman WH, Bernstein MA, Sandstrom JC. A method for correctly setting the rf flip angle. *Magn Reson Med* 1989 ;9:16–24.
3. Snyder CJ, DelaBarre L, Metzger GJ, Moortele P-F van de, Akgun C, Ugurbil K, Vaughan JT. Initial results of cardiac imaging at 7 tesla. *Magnetic Resonance in Medicine* 2009 ;61:517–524.
4. Insko EK, Bolinger L. Mapping of the Radiofrequency Field. *Journal of Magnetic Resonance, Series A* 1993 ;103:82–85.
5. Stollberger R, Wach P. Imaging of the active B1 field in vivo. *Magn Reson Med* 1996 ;35:246–51.
6. Wang J, Qiu M, Yang QX, Smith MB, Constable RT. Measurement and correction of transmitter and receiver induced nonuniformities in vivo. *Magnetic Resonance in Medicine* 2005 ;53:408–417.
7. Yarnykh VL. Actual flip-angle imaging in the pulsed steady state: A method for rapid three-dimensional mapping of the transmitted radiofrequency field. *Magnetic Resonance in Medicine* 2007 ;57:192–200.
8. Counsell CJR. Stimulated Echoes and Spin Echoes. Simultaneous Determination of T2, Diffusion Coefficient, and RF Homogeneity. *Journal of Magnetic Resonance, Series B* 1993 ;101:28–34.
9. Akoka S, Franconi F, Seguin F, Le Pape A. Radiofrequency map of an NMR coil by imaging. *Magnetic Resonance Imaging* 1993 ;11:437–441.
10. Oh CH, Hilal SK, Cho ZH, Mun IK. Radio frequency field intensity mapping using a composite spin-echo sequence. *Magnetic Resonance Imaging* 1990 ;8:21–25.
11. Liang Z-P, Lauterbur PC. *Principles of Magnetic Resonance Imaging: A Signal Processing Perspective*.
12. Wang L, Nouha Salibi, Yan Wu, Mark E. Schweitzer, Ravinder R. Regatte. Relaxation times of skeletal muscle metabolites at 7T. *Journal of Magnetic Resonance Imaging* 2009 ;29:1457–1464.
13. Schär M, Kozerke S, Fischer SE, Boesiger P. Cardiac SSFP imaging at 3 Tesla. *Magnetic Resonance in Medicine* 2004 ;51:799–806.
14. Naressi A, Couturier C, Devos JM, Janssen M, Mangeat C, de Beer R, Graveron-Demilly D. Java-based graphical user interface for the MRUI quantitation package. *MAGMA* 2001 ;12:141–52.
15. Vanhamme, van den Boogaart A, Van Huffel S. Improved method for accurate and efficient quantification of MRS data with use of prior knowledge. *J Magn Reson* 1997 ;129:35–43.
16. Boesch C. Musculoskeletal spectroscopy. *J Magn Reson Imaging* 2007 ;25:321–338.
17. Collins CM, Smith MB. Calculations of B1 distribution, SNR, and SAR for a surface coil adjacent to an anatomically-accurate human body model. *Magnetic Resonance in Medicine* 2001 ;45:692–699.
18. Ren J, Dimitrov I, Sherry AD, Malloy CR. Composition of adipose tissue and marrow fat in humans by ^1H NMR at 7 Tesla. *J. Lipid Res.* 2008 ;49:2055–2062.

19. Wright P, Mougin O, Totman J, Peters A, Brookes M, Coxon R, Morris P, Clemence M, Francis S, Bowtell R, Gowland P. Water proton T₁ measurements in brain tissue at 7, 3, and 1.5T using IR-EPI, IR-TSE, and MPRAGE: results and optimization. *Magnetic Resonance Materials in Physics, Biology and Medicine* 2008 ;21:121–130.



Technical developments Brain imaging



5

Origin and reduction of motion and f_0 artifacts in high resolution T_2^* -weighted magnetic resonance imaging: application in Alzheimer's disease patients

*M.J. Versluis
J.M. Peeters
S. van Rooden
J. van der Grond
M.A. van Buchem
A.G. Webb
M.J.P. van Osch*

ABSTRACT

The altered iron concentration in many neurodegenerative diseases such as Alzheimer's disease (AD) has led to the development of MRI sequences that are sensitive to the accompanying changes in the transverse relaxation rate. Heavily T_2^* -weighted imaging sequences at high magnetic field strength (7 Tesla and above), in particular, show potential for detecting small changes in iron concentration. However, these sequences require a long echo time in combination with a long scanning time for high resolution and are therefore prone to image artifacts caused by physiological fluctuations, patient motion or system instabilities. Many groups have found that the high image quality that was obtained using high resolution T_2^* -weighted sequences at 7 T in healthy volunteers, could not be obtained in AD patients. In this study the source of the image artifacts was investigated in phantom and in healthy volunteer experiments by incorporating movement parameters and resonance frequency (f_0) variations which were measured in AD patients. It was found that image degradation caused by typical f_0 variations was a factor-of-four times larger than artifacts caused by movement characteristic of AD patients in the scanner. In addition to respiratory induced f_0 variations, large jumps in the f_0 were observed in AD patients. By implementing a navigator echo technique to correct for f_0 variations, the image quality of high resolution T_2^* -weighted images increased considerably. This technique was successfully applied in five AD patients and in five subjective memory complainers. Visual scoring showed improvements in image quality in 9 out of 10 subjects. Ghosting levels were reduced by $24 \pm 13\%$.

INTRODUCTION

Many neurodegenerative diseases, such as Alzheimer's, Huntington's and Parkinson's disease are accompanied by local changes in iron concentration (1–3). In Alzheimer's disease (AD) recent developments suggest that iron is bound to amyloid beta plaques in the grey matter (GM) (4, 5). Tissues with elevated iron concentration generate magnetic field inhomogeneities which can be visualized with MRI using, for example, heavily T_2^* -weighted sequences. In samples from deceased AD patients it has been shown that the increased concentration of iron leads to significant signal loss on high resolution T_2^* -weighted images (4, 6). The typical size of amyloid beta plaques ranges from 16 to 150 μm (7), which makes direct in-vivo visualization of individual plaques within a clinically-acceptable scan time highly unlikely. However, whole body high field (7 T and above) MRI scanners might enable the indirect detection of small changes in iron concentration in vivo due both to the intrinsic higher signal-to-noise, which can be used to increase the resolution, and the increased sensitivity to magnetic field inhomogeneities. Very high resolution (up to 0.2 mm in-plane resolution) T_2^* -weighted images at 7 T have been reported recently in young healthy volunteers (8–12), showing an increased contrast between GM and white matter (WM) regions compared to lower field strengths. However, there are potential problems in applying these types of sequences in patients. Heavily T_2^* -weighted sequences require a long echo time (TE) to generate sufficient T_2^* contrast and, because of the high spatial resolution, the scan duration is typically long. As a result of these two factors the images are very sensitive to physiological fluctuations, patient motion and system instabilities, potentially causing blurring, signal cancellation and ghosting. Many of these effects are particularly pronounced at high magnetic field (13). Results obtained at our institution in normal healthy volunteers at 7 T are comparable to the high quality anatomical images that have been reported by other authors using a similar sequence (10, 11, 13). However, application of the same sequence in AD patients and in subjects with subjective memory complaints (SMC) showed a dramatically reduced image quality.

This study is divided into two parts. First, the source of the image artifacts in AD patients was investigated. Using phantom and healthy volunteer scans the different contributions of translational motion, rotational motion, and time-dependent f_0 variations to image artifacts were measured. Secondly, based on the results of the first part (which showed that f_0 variations were dominant), a navigator-echo based correction technique was designed and implemented to improve the image quality in AD patients and SMC subjects.

Qualitative assessment of image quality was achieved using scoring by three observers and quantitative measures of the reduction in ghosting levels were reported.

MATERIALS AND METHODS

Informed consent was obtained from all subjects and this study was approved by the local ethics committee. All experiments were performed on a whole body 7 T system (Philips Healthcare, Best, The Netherlands).

Synthesized motion and f_0 variations

Among the factors that influence the image quality in brain exams, are physiologically induced f_0 changes (13–17) and patient motion (18–21). The influence of these factors on high resolution T_2^* -weighted images was investigated using phantom and healthy volunteer scans. Experiments were performed in which the off-center position, angulations and f_0 of the imaging volume were changed for each acquired k-line during scanning to simulate the effects of respiration and motion. This was achieved by dynamically changing the demodulation frequency and phase for each k-space line via the software interface. This process was termed “synthesized” motion and f_0 variations. The particular motion parameters used were taken from 4 AD patients that had previously participated in an unrelated resting-state functional MRI (fMRI) study performed previously at 3 T in our institution. The motion parameters were interpolated to match the repetition time (TR) of the high resolution T_2^* -weighted sequence. Resonance frequency variations were measured in two healthy subjects and in two AD patients at 7 T using a navigator echo technique (see navigator echoes section).

The effects of synthesized motion and f_0 variations in phantom experiments

A manufacturer provided aqueous phantom consisting of different sized structures was used for the phantom experiments in combination with a quadrature transmit-receive birdcage coil. A T_2^* -weighted sequence with scan parameters: TR / TE / flip angle = 796 ms / 25 ms / 45°, voxel size = 0.24 x 0.24 x 1 mm³, FOV = 240 x 180 mm², 3 slices and 2 averages was used for the following experiments: 1) a normal sequence with no synthesized motion or f_0 variations, 2) synthesized translations in the frequency encoding direction, 3) synthesized translations in the phase encoding direction, 4) synthesized rotations in all three directions, 5) the combination of both synthesized translations and rotations, and 6) the combination of synthesized translations, rotations and f_0 variations. The artifact power was quantified

by calculating the sum-of-squares differences (SSD) between the obtained image and a repeat of scan 1.

The effects of synthesized motion and f_0 variations in healthy volunteers

To investigate the type of artifacts that resulted from motion and f_0 variations on in-vivo images, several of the synthesized experiments described in the phantom experiments section were repeated in three healthy volunteers (2 females, age 24 ± 4 years). The sequence described in the previous section was used with 20 axial slices and no signal averages, resulting in a total scan duration of 9 minutes. Frequency and phase encoding direction were along the anterior-posterior (AP) and right-left (RL) axes, respectively. A Nova Medical quadrature transmit, 16 channel phased array receive coil was used. The following experiments were performed, 1) no synthesized motion, 2) synthesized translation and rotation in both the frequency and phase encoding direction, and 3) synthesized translation and rotation including f_0 variations. To keep the total time for the in-vivo experiments within acceptable limits, we chose to only use a single motion parameter dataset (obtained in one AD patient as was described in the previous section), and a single f_0 parameter set (from another AD patient, also described in the previous section). In addition a respiratory belt was used to measure respiration-induced abdominal movements.

Navigator echoes:

Based on the results from the phantom and healthy volunteer experiments (see results section) it was found that f_0 variations had the greatest contribution to the image artifacts. Therefore, a navigator echo correction technique was designed to measure and correct for f_0 variations (22–24). A navigator echo was acquired through the center of k-space before the phase encoding gradient but after flow compensation gradients in the frequency encoding and slice selective dimensions. No flow compensation on the phase encoding axis was applied to limit eddy current induced phase variations resulting from the temporally-varying flow compensation gradients. The phase of the navigator signal is given by (15):

$$\varphi(\tau) = 2\pi f_0 \tau + \varphi_{system} \quad [1]$$

where τ is the time after excitation, and φ_{system} is an TE independent phase term which is caused by system instabilities such as eddy currents. The phase was calculated after Fourier transformation (20) and was weighted by the signal magnitude.

The phase difference ($\Delta\varphi_j$) was measured using the difference between the first navigator echo and the j^{th} navigator. $\Delta f_{0,j}$ can then be calculated:

$$\Delta f_{0,j} = \frac{\Delta\varphi_j(\tau)}{2\pi\tau} \quad [2]$$

where $\Delta f_{0,j}$ is the difference in resonance frequency between the j^{th} navigator and the first navigator. It was assumed that the f_0 does not change during the time between excitation and acquisition of a single k-space line, and also that no motion takes place during this time. Therefore $\Delta\varphi_j(\tau)$ increases linearly with time and each phase encoded (k_y) imaging echo can be corrected by:

$$S_{corr}(x, k_y) = S(x, k_y)e^{-i2\pi\Delta f_{0,j}TE} \quad [3]$$

where $S_{corr}(x, k_y)$ and $S(x, k_y)$ are the corrected and acquired signal, respectively, after Fourier transform along the frequency direction and TE is the echo time of the acquisition echo.

In vivo experiments:

Five AD patients (79 ± 4 years) and five SMC subjects (62 ± 10 years) were scanned using a flow compensated T_2^* -weighted sequence with the following parameters: TR / TE / flip angle = 796 ms / 25 ms / 45° , voxel size = $0.24 \times 0.24 \times 1 \text{ mm}^3$, FOV = $240 \times 180 \text{ mm}^2$, 20 axial slices with a gap of 0.1 mm. The bandwidth per pixel was 46 Hz, corresponding to a readout length of approximately 22 ms. Frequency and phase encoding direction were along the AP and RL axes, respectively. A navigator echo was acquired along the same direction as the read out gradient at time $TE_{nav} = 9.5$ ms, before the phase encoding gradient was applied. The navigator was sampled at an increased bandwidth to reduce the TE of the acquisition: the duration of the acquisition window for the navigator echo was 4.3 ms. The total scan duration was approximately 10 minutes. Shimming up to third order was performed using an image based shimming approach (25). The images were reconstructed with and without navigator echo correction. Qualitative visual grading of the images was performed by three observers blinded to which dataset was reconstructed with or without navigator echo correction. Each pair of images was evaluated based on the appearance of artifacts and the image with the highest image quality was selected. Interobserver agreement was calculated using the kappa-statistic (26). Ghosting levels for each pair of corrected and uncorrected images were determined by calculating the average signal intensity outside the brain anatomy.

RESULTS

Figure 1 compares the image quality obtained from a healthy volunteer and an AD patient. It is clear that the image quality from the AD patient is considerably poorer than that obtained in the healthy volunteer. In addition differences in image contrast, ventricular size and brain morphology can be observed which can be attributed to the disease and aging process.

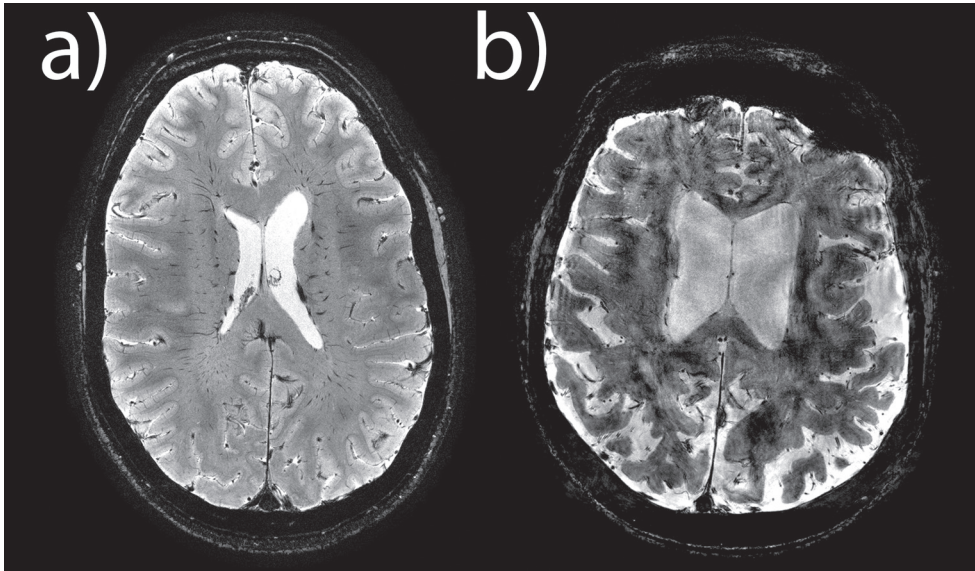


Figure 1: Comparison of T_2^* -weighted images.

Images obtained in a 22 year old healthy volunteer (a) and in a 86 year old AD patient (b) using the same sequence. Image quality is reduced considerably in the image on the right. Scan parameters: TR / TE / flip angle = 796 ms / 25 ms / 45°, voxel size = 0.24 x 0.24 x 1 mm³, FOV = 240 x 180 mm², 20 slices with a gap of 0.1 mm.

Figures 2a and (b) show the estimated time-series of translational and rotational motion measured in an AD patient in the separate study at 3T. The maximum translational motion for the four AD patients was found to be less than 1.5 mm and rotations were typically less than 1 degree. Figure 2c shows the time-dependent f_0 variations measured in one AD patient at 7 T. The amplitude of respiration-induced f_0 variations was considerably different between subjects but was typically about 6 Hz, which was larger than previously reported values (13, 15, 23) at 3T (about 1.25 Hz) and at 7 T (about 1.5 – 3.5 Hz). The reported f_0 changes were calculated with respect to a reference navigator signal for each slice. The displayed f_0 fluctuations include f_0 changes from all slices (2.2 cm coverage in the feet-head direction). Based on these calculations it is not possible to measure the spatial dependency of the amplitude of f_0 changes, which was shown to be present for respiratory f_0 chan-

ges (15). The temporal resolution of each individual slice is too low (TR = 796 ms) to adequately sample the respiration pattern on a slice by slice basis.

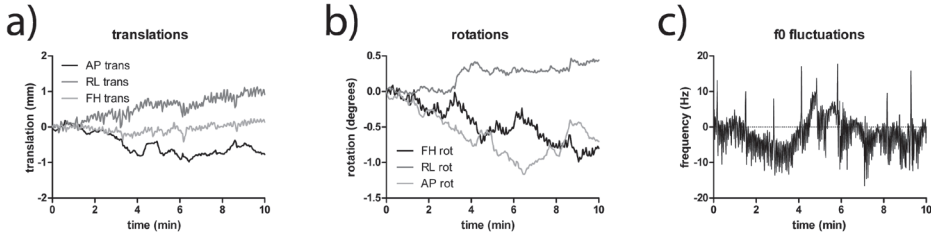


Figure 2: Translational and rotational motion and f_0 fluctuations in an AD patient.

(a) and (b) show typical time-series of translational and rotational motion as measured in AD patients in a separate study at 3T. (c) Shows the time-dependent f_0 variations measured in an AD patient at 7 T.

The time-dependent motion and f_0 values were incorporated into the phantom studies, with motion and f_0 effects being synthesized via changes in the transmit and receive offset frequency and phase for each acquired k-space line. The results are shown in Figure 3a, which illustrates that there is a linear relationship between the artifact power and the degree of linear motion and that the contribution to the artifact level of rotational motion is much less than translational motion. It can also be seen that translational motion in the AP and RL direction had a very similar effect on the amount of artifacts. When the translational motions in the AP and RL direction are combined the artifact power is approximately the sum of both directions individually. Figure 3b shows that the contribution of f_0 fluctuations is the most important factor in the value of the artifact power. The SSD increases from $64 \pm 22\%$ when only translational motion and rotations are considered, to $193 \pm 14\%$ when f_0 variations from healthy volunteers are included, to $376 \pm 15\%$ when f_0 variations from AD patients are included. It can be concluded that the f_0 variations had the largest effect on the amount of artifacts compared to translation or rotations. In addition, the increase in the SSD scales linearly with the amount of motion and f_0 variations ($p < 0.0003$).

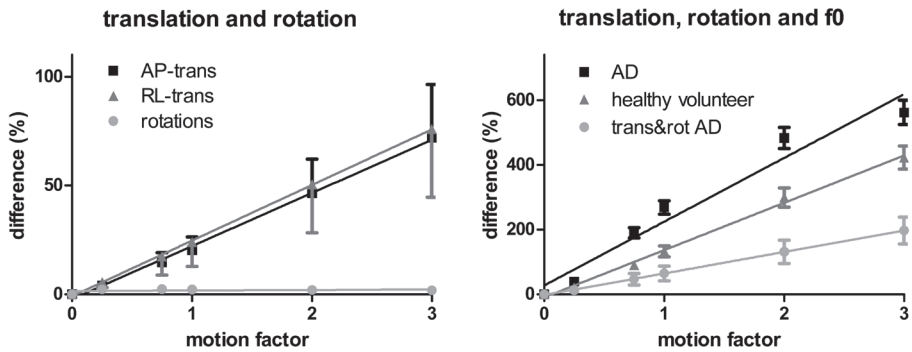


Figure 3: Relative contributions to amount of artifacts.

(a) The effect of translation and rotation on the artifact power for synthesized motion in a phantom. A motion factor of 1 corresponds to the motion parameters from Figure 2(a), a motion factor of 2 doubles these values and so on. It can be seen that there is a linear relationship between the artifact power and the motion factor. (b) Shows the artifact power for translational motion and rotation combined (light gray line), when f_0 variations of healthy volunteers are included (medium gray line) and when f_0 variations of AD patients are included (black line). Note the different scale y-axis of a) and b), error bars display standard error of the mean.

The effect of translational, rotational and f_0 variations on in-vivo images was investigated using the same approach. A single slice is shown from a 28 year old volunteer without any visible motion corruption in figure 4a. When the data are acquired with added synthesized motion and rotation parameters (figure 4b) the image quality is slightly decreased. When f_0 variations from an artifact corrupted scan acquired in an AD patient are added in addition to the translation and rotation parameters severe artifacts occur (figure 4c).

The f_0 variations measured during the complete sequence are displayed in figure 5, for a healthy volunteer (a) and for two AD patients (b,c). Corresponding zoomed regions are shown in (d-f). The relation between respiration and the phase of the navigator was evaluated using a respiratory belt, figure 5 (d), in a healthy volunteer. Both AD patients show large jumps in f_0 in addition to the sinusoidal respiratory induced f_0 variations.

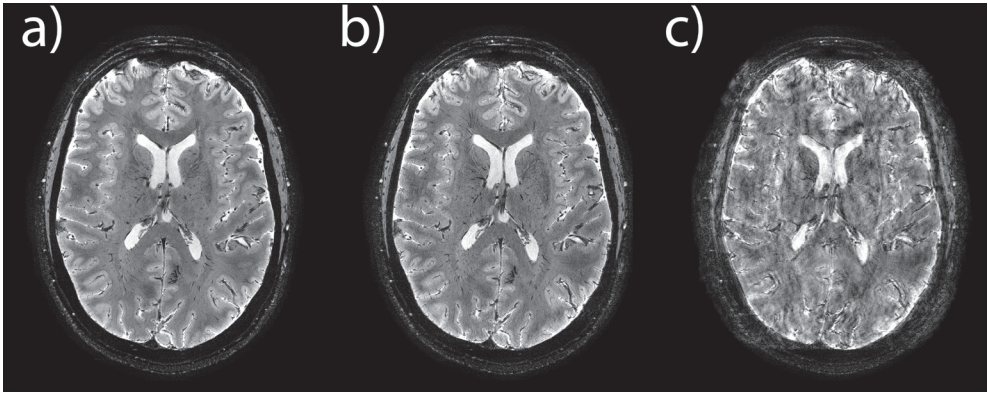


Figure 4: Images acquired from a young healthy volunteer at 7 T.

(a) Standard T_2^* -weighted imaging sequence. (b) Imaging sequence with the translational and rotational values from figure 2(a) and (b) incorporated by varying the demodulation frequency and phase for each k-space line. (c) As for (b) but with the f_0 fluctuations shown in figure 2(c) incorporated into the imaging sequence for each k-space line. Scan parameters: TR / TE / flip angle = 796 ms / 25 ms / 45° , voxel size = $0.24 \times 0.24 \times 1 \text{ mm}^3$, FOV = $240 \times 180 \text{ mm}^2$, 20 slices with a gap of 0.1 mm.

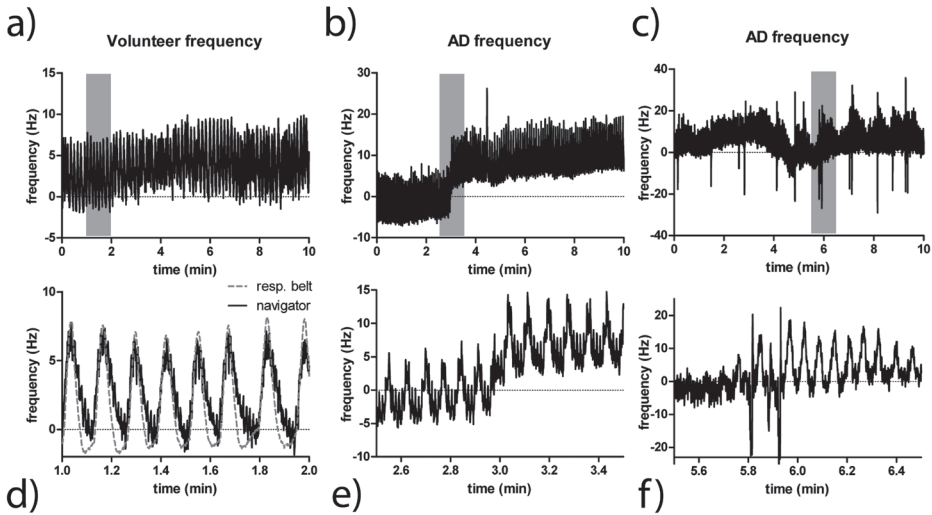


Figure 5: Resonance frequency fluctuations during acquisition.

The top row shows the f_0 variations measured during the complete sequence for a healthy volunteer (a) and two AD patients (b and c). The bottom row shows corresponding zoomed in regions (d-f). The signal from the respiratory belt and the f_0 variations combined for a healthy volunteer is shown in (d). In addition to the sinusoidal respiratory fluctuation jumps (e), or spikes (f) in the f_0 are visible for scans in AD patients.

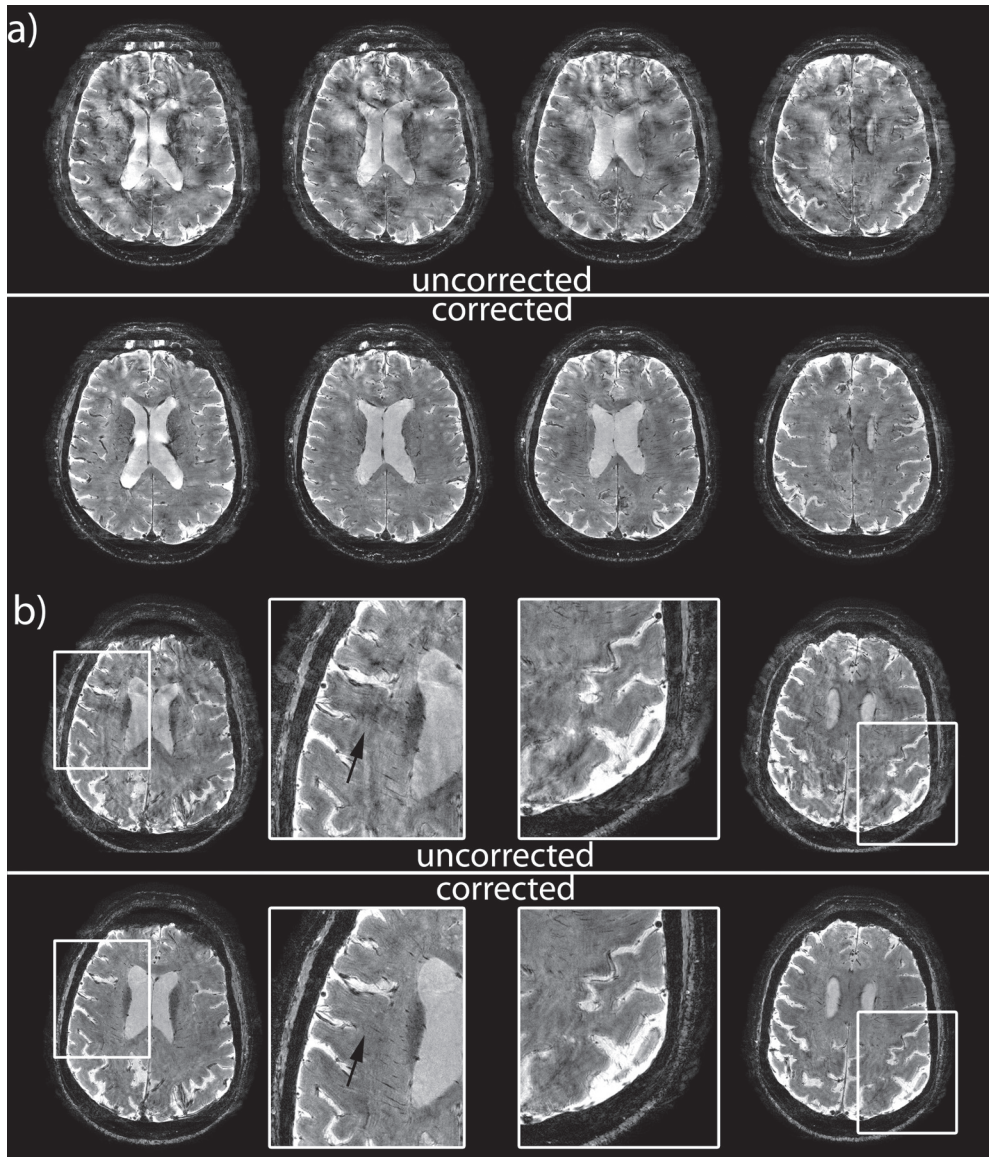


Figure 6: Images reconstructed with and without navigator correction.

The top row shows slices without navigator echo correction. The bottom row shows the same slices reconstructed with navigator echo correction. Four sections from one SMC subject (a) and two sections including corresponding zoomed in regions from an AD patient (b) are shown. The black arrows point to regions with artifacts. The reduction in ghosting level was 38 % for (a), and 28% for (b).

Figure 6 shows examples from one SMC subject (a) and one AD patient (b) without and with navigator echo correction (top and bottom row for each subject, respectively). A clear reduction of the artifacts was visible when nav-

igator echo correction was applied. The amount and severity of many of the artifacts decreased (represented by the black arrows) and ghosting artifacts were reduced. In addition, areas close to regions with a high magnetic field inhomogeneity, such as frontally in the brain also showed improvements. Image quality improvements were found in 9 out of 10 subjects, based on the results of the visual grading. An excellent interobserver agreement was found ($\kappa = 0.86$). Average ghosting levels were reduced with $24 \pm 13\%$ (range 8-46%) when navigator echo correction was applied. No images reconstructed with navigator echo correction were of poorer quality than those without correction. The cases, which showed low reductions in ghosting levels, corresponded to images that already had little artifacts before application of the navigator echo correction.

DISCUSSION

The most important findings of this study were threefold. First the contributions of translational motion and rotation to the amount of artifacts in a T_2^* -weighted sequence were found to be minimal. Second, the decreased image quality in AD patients and SMC subjects results mainly from fluctuations in f_0 during the acquisition. Third, using navigator echoes it is possible to correct for these f_0 fluctuations resulting in a substantial increase in image quality.

The amount of artifacts in many AD and SMC subjects was found to be severe, as is shown in figure 1, making it difficult to interpret the resulting images. Using synthesized motion and f_0 variations in phantom experiments the origin of the artifacts was investigated. It was found that f_0 variations were causing the majority of the image artifacts. In fact, the degree of subject translation and rotation could have been multiplied by a factor-of-three compared to normal AD patient movement before it would have generated the same amount of differences as normal f_0 variations, as indicated in figure 3. This supports the assumption that head motion is not likely to be the main cause of the typical artifacts seen in high resolution T_2^* -weighted sequences of AD patients and SMC subjects. No motion in the foot-head direction was synthesized, but since the slice thickness is much larger than the in-plane resolution it is not likely that these movements will produce significant image artifacts (19). When the same synthesized motion and f_0 parameters were applied to a scan of a healthy volunteer, comparable artifacts occurred as were observed in AD patients (figure 4c). However, when synthetic motion without f_0 variations was included, the image quality was only slightly degraded (figure 4b). Hence the effect of translational motion and rotation can be considered to be minimal. It is, therefore, highly proba-

ble that f_0 variations play the most important role in the artifacts found in AD patients. Previous reports have shown that respiration leads to f_0 changes in the head (13, 15, 23, 27) that are most likely due to volume changes of the chest (16). It is well-documented that the effect that respiration and other susceptibility-related changes have on the phase of MRI signal increases with magnetic field strength (13). In this present study, the measured sinusoidal phase variations in healthy volunteers were found to correspond well with the signal from the respiratory belt (figure 5d). However the large difference in image quality between healthy volunteers and AD patients is not likely to be caused simply by differences in respiration. This is confirmed by the f_0 patterns of two AD patients shown in figure 5, where the most notable differences between a healthy volunteer and two AD patients are the jumps in f_0 during acquisition. A possible explanation for the large variations in f_0 is subject motion (although this was not apparent during the experiment): for example, arm movements or swallowing can lead to substantial f_0 variations in the brain (14, 17).

The findings of our investigations led to the implementation of a navigator echo to correct for f_0 variations. By acquiring a navigator echo separately for each slice it is possible to measure the f_0 per slice for each k-space line. A necessary assumption of this approach was that f_0 variations within a slice are minimal. It has been shown previously that the spatial extent of the f_0 variations due to arm movements within a transverse slice in the brain is relatively small (14), which was also shown earlier for respiratory induced f_0 changes (15). A reduction in the amount and severity of artifacts is visible when performing the navigator echo correction (figure 6). Even though some remaining artifacts are still visible after navigator correction, the image quality is considerably improved. This is supported by the results of the visual evaluation, which showed an image quality improvement in 9 out of 10 subjects with excellent interobserver agreement and the reduction in ghosting levels of 24%. A potential confounding factor of using ghosting levels as a quantitative measure is that the reconstruction algorithm of the scanner masks areas outside the brain automatically, effectively reducing the absolute amount of visible ghosting. However, the relative measures of ghost-level reduction remain valid and these are reported.

Possible explanations for incomplete correction are spatially varying f_0 changes within the slice, or variations that occur between navigator acquisition and image acquisition: the latter is not very likely because of the small separation of approximately 16 ms between the two acquisitions. Future work will focus on measuring and correcting for the spatial distribution of f_0 changes.

Recently, a technique has been introduced that is able to correct for spatially varying f_0 variations within a slice and between slices (13). This technique, which is called “real-time shimming”, uses a calibration scan that relates the motion from the chest wall to the spatially varying magnetic field. During acquisition the shim and f_0 settings are updated dynamically and this technique has been applied successfully in high resolution T_2^* -weighted images at 7 T (9, 13). An advantage of this technique is that it also corrects for spatially varying f_0 differences within a slice, in contrast to the navigator echo technique presented here. However, the temporal behavior of the navigator signal in AD patients (see figure 5) showed that not all f_0 variations were caused by respiration alone. The heavily corrupted scans, in particular, show large jumps in f_0 that are not caused by respiration, which makes adequate suppression of the artifacts in these scans using the dynamic shimming approach unlikely.

Due to the long TE and small readout bandwidth of the acquisition window in most T_2^* -weighted sequences, the time that is needed to acquire a navigator echo is a small fraction of the total scan duration. In the sequence that was used in this study the inclusion of a navigator echo resulted in a scan duration increase of 30 s, which was small compared to the total scan duration of approximately 10 minutes.

In summary, this study has shown that the major source of artifacts in high resolution T_2^* -weighted images at 7 T in AD patients and SMC subjects is caused by variations in f_0 . These f_0 variations are a combination of sinusoidal respiratory induced fluctuations and jumps in f_0 . With the latter causing the majority of the image artifacts. Based on these experiments we have implemented a T_2^* -weighted sequence with navigator echo correction to measure and correct for f_0 variations during scanning. In 9 out of 10 subjects image quality improvements were found using visual scoring.

ACKNOWLEDGEMENT

This research was performed within the framework of CTMM, the Center for Translational Molecular Medicine (www.ctmm.nl), project LeARN (grant 02N-101).

REFERENCES

1. Pinero DJ, Connor JR. Iron in the Brain: An Important Contributor in Normal and Diseased States. *Neuroscientist* 2000 ;6:435–453.
2. Schenck JF, Zimmerman EA, Li Z, Adak S, Saha A, Tandon R, Fish KM, Belden C, Gillen RW, Barba A, Henderson DL, Neil W, O'Keefe T. High-field magnetic resonance imaging of brain iron in Alzheimer disease. *Top Magn Reson Imaging* 2006 ;17:41–50.
3. Stankiewicz J, Panter SS, Neema M, Arora A, Batt CE, Bakshi R. Iron in Chronic Brain Disorders: Imaging and Neurotherapeutic Implications. *Neurotherapeutics* 2007 ;4:371–386.
4. Meadowcroft MD, Connor JR, Smith MB, Yang QX. MRI and histological analysis of beta-amyloid plaques in both human Alzheimer's disease and APP/PS1 transgenic mice. *Journal of Magnetic Resonance Imaging* 2009 ;29:997–1007.
5. Cullen, K.M., Kócsi, Z. & Stone, J., 2006. Microvascular pathology in the aging human brain: evidence that senile plaques are sites of microhaemorrhages. *Neurobiology of Aging*, 27(12), 1786-1796.
6. van Rooden S, Maat-Schieman MLC, Nabuurs RJA, van der Weerd L, van Duijn S, van Duinen SG, Natté R, van Buchem MA, van der Grond J. Cerebral Amyloidosis: Postmortem Detection with Human 7.0-T MR Imaging System. *Radiology* 2009 ;253:788–796.
7. Benveniste H, Einstein G, Kim KR, Hulette C, Johnson GA. Detection of neuritic plaques in Alzheimer's disease by magnetic resonance microscopy. *Proceedings of the National Academy of Sciences of the United States of America* 1999 ;96:14079–14084.
8. Zhong K, Leupold J, von Elverfeldt D, Speck O. The molecular basis for gray and white matter contrast in phase imaging. *Neuroimage* 2008 ;40:1561–6.
9. Yao B, Li T-Q, Gelderen P van, Shmueli K, de Zwart JA, Duyn JH. Susceptibility contrast in high field MRI of human brain as a function of tissue iron content. *Neuroimage* 2009 ;44:1259–1266.
10. Duyn, J.H. et al., 2007. High-field MRI of brain cortical substructure based on signal phase. *Proceedings of the National Academy of Sciences of the United States of America*, 104(28), 11796-801.
11. Li, T. et al., 2006. Extensive heterogeneity in white matter intensity in high-resolution T_2^* -weighted MRI of the human brain at 7.0 T. *NeuroImage*, 32(3), 1032-1040.
12. Lee J, Hirano Y, Fukunaga M, Silva AC, Duyn JH. On the contribution of deoxy-hemoglobin to MRI gray-white matter phase contrast at high field. *NeuroImage* 2010 ;49:193–198.
13. Van Gelderen P, de Zwart JA, Starewicz P, Hinks R, Duyn JH. Real-time shimming to compensate for respiration-induced B_0 fluctuations. *Magnetic Resonance in Medicine* 2007 ;57:362–368.
14. Barry, R.L. et al., 2009. Evaluation of preprocessing steps to compensate for magnetic field distortions due to body movements in BOLD fMRI. *Magnetic Resonance Imaging*, In press, corrected proof.
15. Van de Moortele PF, Pfeuffer J, Glover GH, Ugurbil K, Hu X. Respiration-induced B_0 fluctuations and their spatial distribution in the human brain at 7 Tesla. *Magnetic Resonance in Medicine* 2002 ;47:888–895.

16. Raj D, Paley DP, Anderson AW, Kennan RP, Gore JC. A model for susceptibility artefacts from respiration in functional echo-planar magnetic resonance imaging. *Physics in Medicine and Biology* 2000 ;45:3809–3820.
17. Birn, R.M. et al., 1998. Magnetic field changes in the human brain due to swallowing or speaking. *Magnetic Resonance in Medicine*, 40(1), 55-60.
18. Norris DG. Implications of bulk motion for diffusion-weighted imaging experiments: Effects, mechanisms, and solutions. *Journal of Magnetic Resonance Imaging* 2001 ;13:486–495.
19. Anderson, A.W. & Gore, J.C., 1994. Analysis and correction of motion artifacts in diffusion weighted imaging. *Magnetic Resonance in Medicine*, 32(3), 379-387.
20. Crespigny, A.J.D. et al., 1995. Navigated Diffusion Imaging of Normal and Ischemic Human Brain. *Magnetic Resonance in Medicine*, 33(5), 720-728.
21. Ordidge RJ, Helpert JA, Qing ZX, Knight RA, Nagesh V. Correction of motional artifacts in diffusion-weighted MR images using navigator echoes. *Magnetic Resonance Imaging* 1994 ;12:455–460.
22. Durand E, Van de Moortele PF, Pachot-Clouard M, Le Bihan D. Artifact due to B0 fluctuations in fMRI: Correction using the k-space central line. *Magnetic Resonance in Medicine* 2001 ;46:198–201.
23. Wowk B, McIntyre M C, Saunders J K. k-space detection and correction of physiological artifacts in fMRI. *Magnetic Resonance in Medicine* 1997 ;38:1029–1034.
24. Brau, A.C.S. & Brittain, J.H., 2006. Generalized self-navigated motion detection technique: Preliminary investigation in abdominal imaging. *Magnetic Resonance in Medicine*, 55(2), 263-270.
25. Schär M, Kozerke S, Fischer SE, Boesiger P. Cardiac SSFP imaging at 3 Tesla. *Magnetic Resonance in Medicine* 2004 ;51:799–806.
26. Watkins MW, Pacheco M. Interobserver Agreement in Behavioral Research: Importance and Calculation. *Journal of Behavioral Education* 2000 ;10:205–212.
27. Hu X, Kim S-G. Reduction of signal fluctuation in functional MRI using navigator echoes. *Magnetic Resonance in Medicine* 1994 ;31:495–503.

6

Retrospective image correction in the presence of non linear temporal magnetic field changes using multi-channel navigator echoes

*M.J. Versluis
B.P. Sutton
P.W. de Bruin
P. Börnert
A.G. Webb
M.J. van Osch*

ABSTRACT

Spatio-temporal magnetic field changes in the brain caused by breathing or body movements can lead to image artifacts. This is especially a problem in T_2^* -weighted sequences. With the acquisition of an extra echo (navigator) it is possible to measure the magnetic field change induced frequency offset for a given slice during image acquisition. However, substantial local variation across a slice can occur. This work describes an extension of the conventional navigator technique that improves the estimation of the magnetic field distribution in the brain during strong field fluctuations. This is done using the combination of signals from multiple coil elements, the coil sensitivity profiles and frequency encoding; termed sensitivity encoded (SENSE) navigator echoes. In vivo validation was performed in subjects who performed normal breathing, nose touching and deep breathing during scanning. The SENSE navigator technique leads to an error reduction in estimating the field distribution in the brain of $73 \pm 16\%$ compared to $56 \pm 14\%$ for conventional estimation. Image quality can be improved via incorporating this navigator information appropriately into the image reconstruction. When the SENSE navigator technique was applied to a T_2^* -weighted sequence at 7 Tesla a ghosting reduction of $47 \pm 13\%$ was measured during nose touching experiments compared to no correction.

INTRODUCTION

Magnetic resonance imaging (MRI) is ideally performed in a spatially and temporally stable and homogeneous magnetic field, especially when using gradient echo sequences in which magnetic field inhomogeneities lead to loss of phase coherence. It has been shown previously that body movements and respiration lead to substantial variations of the magnetic field in the brain (1–6). These effects are significantly more pronounced at high magnetic field strengths. One of the sequences frequently used at 7 Tesla is a strongly T_2^* -weighted gradient echo, because of the high intrinsic contrast in both magnitude and phase which allows differentiation of cortical layers, as well as detection of diffuse depositions of iron associated with various neurodegenerative diseases (7–10). Due to the sensitivity of this sequence to spatial and temporal variations in both T_2^* and phase (through changes in the resonance frequency), changes in these parameters that are not related to tissue properties can have a large detrimental effect on image quality.

Variations in the local magnetic field can be separated into static inhomogeneities, i.e. those that remain constant during the experiment, and dynamic inhomogeneities, i.e. those that fluctuate throughout the experiment. On most current systems up-to-third order shimming is available to compensate at least partially for static inhomogeneities. In contrast, dynamic magnetic field changes, such as caused by respiration and body movements cannot be corrected using static shimming approaches.

Several methods, either prospective or retrospective, exist to measure and correct partially for these dynamic field variations. It has been shown that a reference scan can be used to relate field changes caused by normal respiration to the chest motion (1). By measuring the chest motion during image acquisition prospective correction was possible by dynamically switching the shim values. Using this approach, however, only periodic field fluctuations due to respiration can be corrected while non-periodic fluctuations due to cardiac pulsations and body movements, for example, lead to fluctuations that are not corrected. Others have used external magnetic field probes to sample the magnetic field changes at several spatial locations during image acquisition, an approach that is also capable of measuring non-periodic fluctuations, but requires dedicated hardware (11, 12).

Another approach to compensate for dynamic field variations is to sample an extra navigator echo before phase encoding (6, 13–17), or to use special sequences capable of self-navigation (18–20). Based on the difference between successive navigator signals the temporal magnetic field disturbance can be

estimated and corrected during image reconstruction. An advantage of the navigator echo approach is that it does not require dedicated hardware. So far this technique has mostly been used to correct for zeroth order temporal changes in the magnetic field. This can be sufficient to correct for magnetic field changes induced by normal respiration when axial images through the brain are considered (2, 4). Substantial improvements in image quality of high resolution T_2^* -weighted images have been shown in Alzheimer's disease patients, where the changes in the magnetic field were measured for each axial slice separately and used to correct the phase of each acquired k-space line retrospectively (6). However, residual image artifacts still remain, which were hypothesized to arise from spatio-temporal magnetic field fluctuations *within* a slice.

The aim of this work is to address and correct for the artifacts that are caused by these within-slice dynamic magnetic field fluctuations. A prerequisite for this approach is that information about the magnetic field distribution must be available at a sufficiently high temporal and spatial resolution. In this work the field map information is derived by integrating frequency-encoded navigators with the intrinsic spatial information from the coil sensitivity profiles of the individual elements of the receive array (21–23). Subsequently this information was used to correct retrospectively the corrupted images. To test the robustness of this correction approach strong spatio-temporal magnetic field inhomogeneities were produced by having subjects perform nose touching and deep breathing tasks during image acquisition. This was used to model the worst case fluctuations that can occur during patient examinations. Additionally, the method was evaluated in cooperative subjects instructed to remain still and breathe normally.

MATERIALS AND METHODS

All experiments were performed on a 7 T whole body system (Philips Healthcare, Best, The Netherlands), equipped with a quadrature transmit and 32-channel phased array head coil (Nova Medical, USA). All subjects gave written informed consent prior to the study in compliance with local ethics regulations.

This study is divided into two parts, in the first part the accuracy of the spatial field estimations is investigated using very fast imaging as a ground truth. In the second part a reconstruction framework is developed to correct retrospectively the data using the measured dynamic field fluctuation information.

Spatial field estimations

The navigator echo was acquired immediately after each RF excitation using 32 receive channels; see Figure 1 for more details. A complex difference signal was calculated between the first and the successively acquired navigator echoes, which is subsequently converted to a frequency shift for each channel ($f_{0,nav}$). The navigator echo was acquired once for every excitation, and a phase correction was applied to all k-space lines following the same excitation, either one gradient echo, or the entire echo planar imaging (EPI) train.

Four different methods were investigated for spatial field mapping based on this one-dimensional navigator. The first method consists of a complex summation over the individual channels and temporal sampling points, resulting in a global estimation of the frequency shifts: this is the zeroth order approach outlined in ref. (6) and is used as a reference. The second method consists of a coil sensitivity weighted summation over the channels and summation over all temporal sampling points: this is termed the sensitivity encoded (SENSE) navigator approach. The third method is similar to the second method but in addition includes the spatial information of the frequency encoding gradient in the anterior/ posterior direction: this is termed the frequency encoded SENSE navigator. The fourth method includes the frequency encoding gradient after averaging all channels, this is called the frequency encoded navigator.

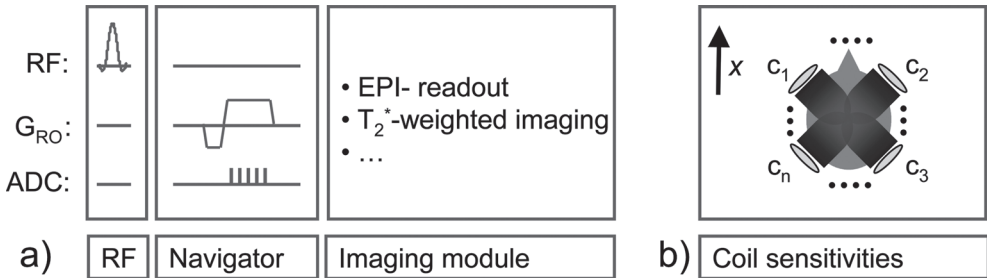


Figure 1: SENSE navigator sequence details.

(a) The acquisition of the navigator is shown schematically in a sequence diagram. The navigator echo is acquired after slice selection prior to phase encoding and is followed by an imaging module. G_{RO} is the navigator readout gradient, and ADC is the analog-to-digital converter. (b) Multiple coil elements with different coil sensitivities are used to sample the navigator echo simultaneously (depicted schematically as $c_1 - c_n$). Four different navigators have been studied. In the first a complex summation of all temporal sampling points is performed and all coil signals are simply added before evaluation. Also in the second the sampling points are summed, but all coil signals are added including spatial coil sensitivity weighing, while the third is equal to the second one, but taking into account the spatial frequency encoding gradient (G_{RO}) along the x direction to increase the spatial definition. The fourth approach only uses the G_{RO} after adding all individual coil signals.

All four types of field map reconstruction (zeroth order, frequency encoded

and both SENSE navigator estimations) use exactly the same acquired data, allowing the results for the different approaches to be compared.

For the SENSE navigator field techniques the individual field estimations ($f_{0,nav}$) were weighted according to a separately acquired coil sensitivity map (CSM) that describes the spatially varying sensitivity of each receive coil element, to produce a dynamic low resolution two dimensional field distribution map ($f_{0,nav}(x, y, t)$) (22):

$$f_{0,nav}(x, y, t) = \sum_{ch} f_{0,nav}(x, t, ch) \cdot CSM(x, y, ch) \quad [1]$$

Where x and y are the frequency- and phase encoding directions, respectively and ch denotes the receive coil element. The CSM was calculated on the scanner using a manufacturer provided method that uses the ratio between an image acquired with the 32 channel receive array and the quadrature transmit-receive coil as receive coil in order to limit the effect of T_2 differences on the CSM.

The amplitudes of the CSMs are normalized voxelwise such that each voxel location, when summed over the channels, adds up to unity. For the frequency encoded SENSE navigator, first a Fourier transform was applied along this direction to resolve the spatial dependence. The phase difference signal in the frequency encoding direction was fitted using a polynomial of 2nd order to reduce the effects of noise, after which the previously described steps were performed. This was empirically found to be the lowest polynomial order that matched the observed magnetic field distribution patterns adequately. For the SENSE navigator $f_{0,nav}(x, t, ch)$ reduces to $f_{0,nav}(t, ch)$ and for the frequency encoded navigator to $f_{0,nav}(x, t)$. The zeroth order navigator results in a single frequency change value for each time point: $f_{0,nav}(t)$.

To estimate and assess the accuracy of these four navigator-based field estimations the following experiment was conducted. A fast single shot EPI sequence was run with the following parameters: repetition time (TR) /echo time (TE)/flip angle (FA) = 65 ms/ 25 ms/ 25°, EPI factor = 27, SENSE factor 2.3, voxel size = 3.3x3.3x3 mm³, bandwidth per pixel = 23 Hz. Before image acquisition the navigator echo was acquired using 32 coil elements at $TE_{nav}=2.1$ ms. A total of 4000 images were acquired resulting in 4'20'' scanning time. Four subjects performed the following tasks during scanning: touching their nose, moving one arm, touching their neck, and taking deep breaths. The first image was taken as a reference and the phase difference with respect to

subsequent images was calculated. These measurements were considered the ground truth and were compared to the navigator based estimations of the spatio-temporal field variations. Head motion was minimized using foam padding and was visually monitored.

To assess the error for each of the three approaches sum-of-square difference (SSD) maps were generated between the ground truth measurements and the navigator based estimations. The maps were summed over all voxels and timepoints to yield a single number indicating the accuracy of the specific navigator approach. A reduction in the SSD (RSSD), defined as $(SSD_{navigator} - SSD_{no\ correction}) / SSD_{no\ correction}$ will be reported.

Image artifact correction

The second component of the study consists of using the different navigator field estimation approaches for image artifact correction in a T_2^* -weighted sequence. The following sequence was used to demonstrate the effects that magnetic field variations can have on image quality. Six subjects were scanned using a 2D gradient echo sequence with the following parameters: TR/TE/FA = 400 ms/20 ms/ 30°, the navigator was acquired at $TE_{nav} = 10$ ms, voxel size $0.42 \times 0.42 \times 3$ mm³, and data matrix size of 480x480. Three separate scans were acquired: 1) subject lying still, 2) subject touching nose at approximately 10 s intervals, and 3) subject taking deep breaths. The first scan is considered as a reference image and is used to compare the performance of the navigator based reconstructions of images acquired during intentional magnetic field variations. For each acquired k-space line an estimation of the magnetic field change was made using the previously described navigator techniques. The resulting phase errors can be incorporated in the image encoding equation (11, 24), written in matrix form:

$$\mathbf{k} = \mathbf{E} \mathbf{m} \tag{2}$$

Where \mathbf{k} is the k-space data, \mathbf{m} is the image space data, both stored as a column vector of size $[N_x N_y]$, where N_x is the number of frequency encodings and N_y is the number of phase encodings, or voxels along the respective dimensions. \mathbf{E} is the encoding matrix, containing both the Fourier encoding terms as well as the derived phase errors for each shot and location. If parallel imaging is not considered \mathbf{E} is of size $[N_x N_y \times N_x N_y]$ and becomes prohibitively large even for moderate imaging resolutions. Therefore an iterative approach based on a conjugate gradient solver was used that calculates only the relevant parts of \mathbf{E} and the complex conjugate \mathbf{E}^H to solve this problem efficiently (24–26). Equation 2 can be rewritten as:

$$\mathbf{k} = \sum_i \{[\mathbf{M}_i \mathbf{F} \mathbf{P}_i] \mathbf{m}\} \quad [3a]$$

and,

$$\mathbf{k} = \sum_i \{[\mathbf{P}_i^H \mathbf{F}^{-1} \mathbf{M}_i^H] \mathbf{m}\} \quad [3b]$$

Where equation 3a calculates $\mathbf{E} \mathbf{m}$ and equation 3b calculates $\mathbf{E}^H \mathbf{m}$. \mathbf{M}_i is a diagonal matrix of size $[N_x N_y \times N_x N_y]$ that selects the data for the i^{th} shot. \mathbf{F} is the Fourier transformation, \mathbf{F}^{-1} is the inverse Fourier transformation and \mathbf{P}_i is a diagonal matrix of size $[N_x N_y \times N_x N_y]$ that contains the phase variations for the i^{th} shot. The summation is performed over the number of shots. Based on visual inspection the maximum number of iterations was set to 3, to limit reconstruction times. Data for multiple coils were reconstructed separately and combined using the coil sensitivity maps (27). Images were reconstructed both with and without navigator echo correction. Phase images were unwrapped using k-space based high-pass filtering, as detailed in ref. (28)

Overall reconstruction times were 1 minute per channel for a single slice on an 8 core Intel 2.27 GHz processor with 12 GB internal memory, using Matlab 2009a (Mathworks, USA)..

To assess image quality, difference images were generated between the separately acquired non-corrupted image (where the subject was asked to lie still in the scanner) and the images where movements were intentionally made. A large percentage reduction in the difference image corresponds to a small difference between the reference image and the retrospectively corrected image, which is a measure for how well the navigator reconstruction performed. In four subjects the reference scan was repeated while the subject was lying still, in order to assess the stability of the navigator based approaches with respect to very small magnetic field fluctuations.

RESULTS

Figure 2 is an example of a single time frame of the spatial magnetic field distribution and illustrates the performance of the different approaches during touching of the nose. Figure 2a displays the “ground truth” magnetic field distribution. The corresponding estimated field change maps using the navigator echo based approaches are shown in Figure 2b for zeroth order, Figure 2c for SENSE navigator estimation without frequency encoding, 2d for frequency encoded navigator estimation and in 2e for SENSE navigator estimation with frequency encoding information. In Figure 2a a spatially inhomogeneous magnetic field distribution is observed with a spread of up to

20 Hz between the anterior and posterior regions. The zeroth order navigator measured a global frequency offset of -6.5 Hz, approximately the average frequency offset over the entire slice. Visually it can be appreciated that both SENSE navigator approaches and the frequency encoded estimation lead to an improved field estimation compared to the zeroth order technique. The low bandwidth of the EPI sequence leads to geometric distortions on the order of 1 to 2 pixels in the phase encoding direction for the observed field variations during the nose touching experiments.

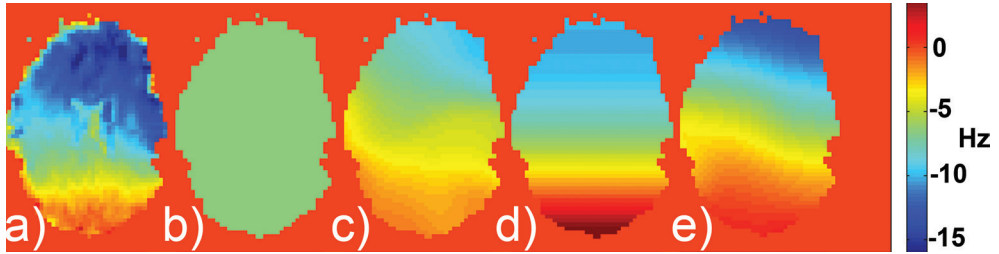


Figure 2: Magnetic field changes during nose touching.

Field changes in an axial brain slice during nose touching measured using an EPI sequence (a) which is considered to be the ground truth field change measurement. b-e) show the navigator based field change estimations. b) is the result of the conventional zeroth order navigator, a global frequency offset of -6.5 Hz is estimated for the entire slice with no spatial resolution. c) is estimated using the SENSE navigator. (d) is estimated using only frequency encoding, and (e) is estimated using the frequency encoded SENSE navigator. The magnetic field varies substantially over the slice between -20 Hz frontally to +5 Hz posterior. Table 1 shows a quantitative summary of the results.

To assess the accuracy of the different approaches quantitatively, SSD maps are generated over the complete time course. The RSSD for the different navigator estimations compared to no estimation is calculated. The zeroth order navigator results in a reduction of $56 \pm 14\%$ ($p = 0.02$). Further reductions are found for SENSE navigator estimation: $70 \pm 14\%$ ($p = 0.02$), for the frequency encoded navigator estimation: $70 \pm 16\%$ ($p = 0.02$) and $73 \pm 16\%$ ($p = 0.02$) is found for the frequency encoded SENSE navigator estimation (see table 1 for details).

Table 1: Reduction in sum of squared difference (RSSD) values.	
Zeroth order navigator	56 ± 14% †
SENSE navigator (no FE)	70 ± 14% †,‡
FE navigator	70 ± 16 % †,‡
SENSE navigator (with FE)	73 ± 16% †,‡

RSSD values for each navigator echo based approach compared to no navigator correction. (no FE): no frequency encoding gradient information is used; (with FE): frequency encoding information of the navigator echo is used. P-values are calculated using a paired t-test, comparing RSSD values between no correction and the different navigator techniques. † denotes significantly different from no correction; ‡ denotes significantly different from zeroth order navigator correction, $p < 0.05$.

The application of the navigator based field estimations for retrospective image correction is shown in Figure 3. Images from the T_2^* -weighted sequence are shown for two slice locations in the brain during nose touching at an interval of approximately 10 s. Figures 3a and 3f show the results when no correction is applied. Severe image artifacts are observed, resulting from the strong dynamically varying magnetic field changes during acquisition. When the image is corrected using a single phase offset for each acquired k-space line (Figures 3b and 3g, zeroth order correction) the image quality is improved, but artifacts still remain. When coil-based SENSE navigator correction is applied image quality is further improved. Figures 3c and 3h show the corresponding results for SENSE navigator correction. Figures 3d and 3i show the resulting images for the frequency encoded navigator correction and Figures 3e and 3j show the results for frequency encoded SENSE navigator correction. Most image quality improvements are observed in the anterior part of the brain. Visually the best image quality is obtained for frequency encoded navigator field estimation and frequency encoded SENSE navigator estimation. The bottom row shows the difference images compared to an artifact free image when no intentional subject motion was introduced. A reduction of differences is visible when navigator correction is applied. Histograms of the difference image values are shown in Figure 3 as an inset on the difference maps. The histograms corresponding to the SENSE and frequency encoded navigator corrected data show a narrower distribution compared to no correction, or zeroth order correction histograms.

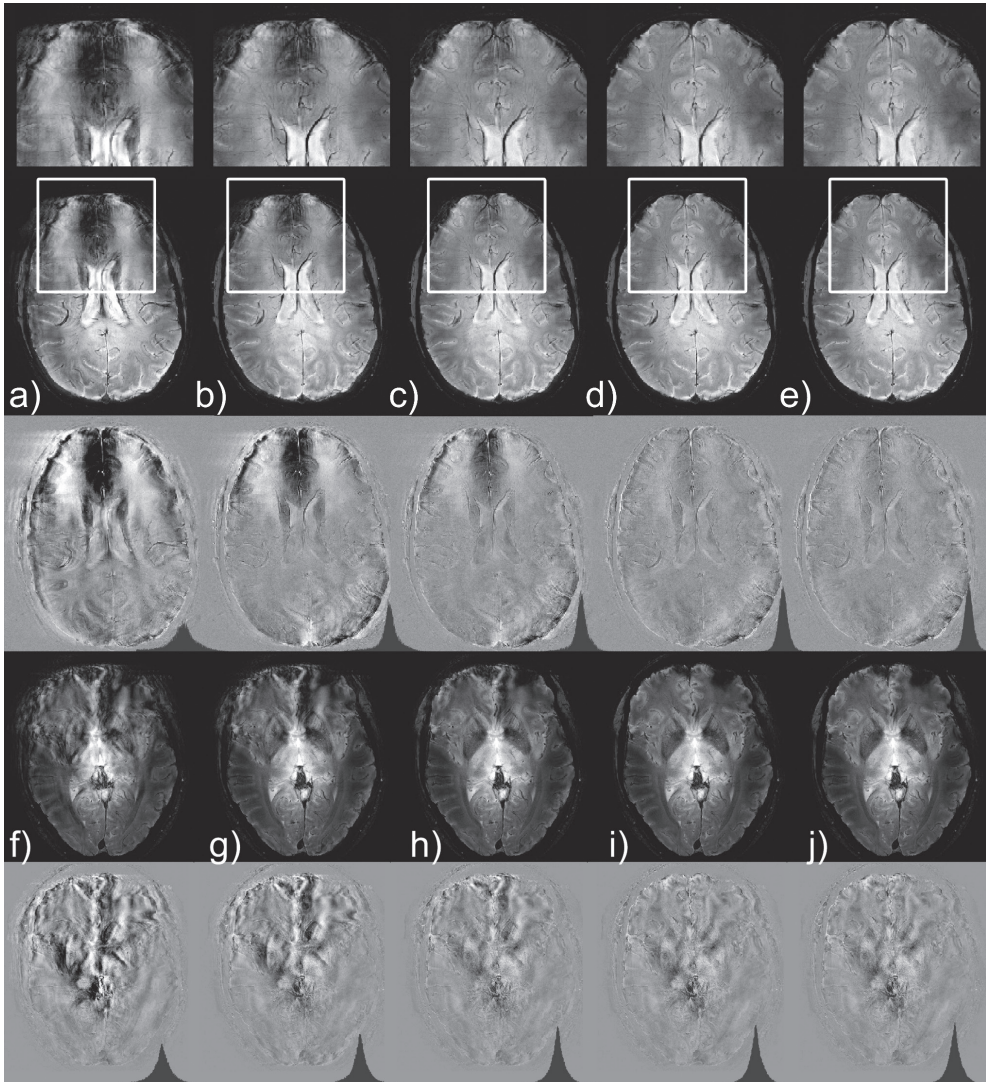


Figure 3: Navigator corrected T_2^* -weighted imaging during nose touching.

Different reconstructions are shown for two slice locations in the brain (a-e) and (f-j), respectively. Below each image the difference image is shown between the corresponding reconstructions and an artifact-free image (no nose touching). Histograms of the difference values are displayed as an inset in the bottom left corner of the difference images. a, f) the original dataset without correction. b, g) Image corrected using conventional (zeroth order) navigator correction. Artifacts in the frontal part of the brain are reduced (see zoomed in sections), c, h) image after SENSE navigator correction. d, i) Image using the frequency encoded navigator correction, without using coil sensitivity information, e, j) image after frequency encoded SENSE navigator reconstruction. The histograms of the difference values show that the distribution of values becomes narrower when navigator correction is applied. Results are summarized in table 2

With the proposed reconstruction methods the complex MRI signal is preserved and therefore both magnitude and phase images can be reconstructed. Unwrapped phase images for a single subject are shown in Figure 4 during a nose touching experiment. The image quality improves when navigator correction is applied (Figures 4a – e), with the most pronounced reduction in image artifacts for frequency encoded SENSE navigator correction. In addition improved phase unwrapping is observed, depicted by the arrow in the zoomed in sections of the anterior part of the brain. This is particularly apparent in Figures 4d and 4e.

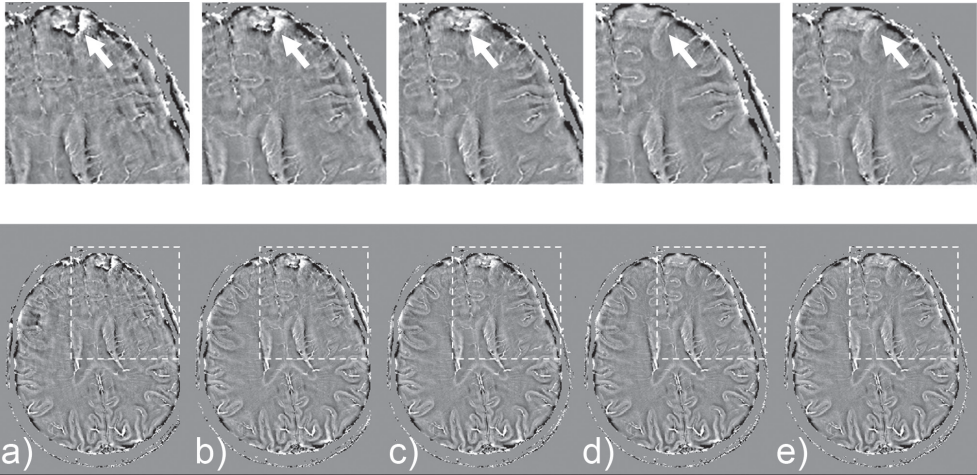


Figure 4: Navigator corrected phase images during nose touching.

Unwrapped phase images during nose touching. a) no correction, b) zeroth order correction, c) SENSE navigator correction, d) frequency encoded navigator correction and e) frequency encoded SENSE navigator correction. Similar to the results of figure 3 much improved image quality is visible for the frequency encoded and SENSE navigator approaches, resulting in clearer phase images. Phase images were unwrapped using a homodyne high-pass filter with a kernel size of 80. The top row shows a zoomed section of the anterior part outlined by the white box. The arrow points to an area that significantly improves. Images are scaled between $-\pi/5$ and $\pi/5$.

Figure 5 shows images of a different subject while performing deep breathing. Again the best results are obtained for frequency encoded and SENSE navigator correction, however in this case the improvements compared to the other approaches are less pronounced. The middle row shows a zoomed section of the posterior part, the arrow points to one of the artifacts that is resolved only when SENSE navigator correction is applied. The bottom row shows the difference images compared to an artifact free image. The difference images are scaled differently compared to Figure 3. Histograms of the difference images show a narrower distribution of values when navigator correction is applied compared to no correction. The differences in histo-

grams between the zeroth order correction and other navigator techniques are less pronounced.

Table 2: Reduction in difference images comparing the navigator approaches.

	0th order correction	SENSE navigator	Frequency encoded navigator	Frequency encoded SENSE navigator
Nose touching	22 ± 9% †	36 ± 13% †,‡	46 ± 14% †,‡	47 ± 13% †,‡
Deep breathing	11 ± 12%	13 ± 12% †,‡	14 ± 12% †,‡	15 ± 12% †,‡
Normal breathing	15 ± 14%	15 ± 14%	15 ± 15%	15 ± 15%

Percentage reduction in difference between image acquired when subjects (n=6) were lying still and when subjects were performing nose touching, deep breathing or normal breathing for the different navigator correction approaches. P-values are calculated using a paired t-test, comparing absolute SSD maps between the artifact free image and the different navigator techniques. † denotes significantly different from no correction; ‡ denotes significantly different from zeroth order navigator correction; p<0.05.

The improvement in image quality was quantified by taking the difference between the corrupted image of a single slice and the separately acquired reference image when the subject was asked to lie still in the scanner. A percentage reduction in the difference image of up to 47 ± 13% (p = 0.01) is obtained for nose touching experiments and up to 15 ± 12% (p = 0.04) for the experiments consisting of deep breathing (see table 2 for details). When no artificial field fluctuations were introduced navigator correction resulted in a reduction in the amount of differences of 15 ± 14 % (p=0.08), irrespective of the navigator correction technique used, compared to when no correction is performed.

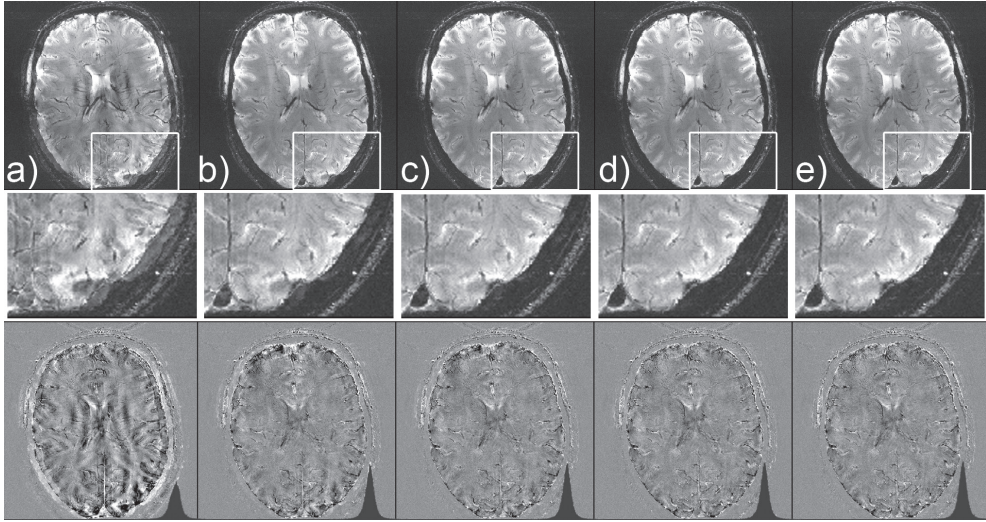


Figure 5: Navigator corrected T_2^* -weighted imaging during deep breathing.

Different reconstructions are shown. a) Uncorrected image, b) image using zero order correction, c) using SENSE navigator correction, d) using frequency encoded correction and e) using frequency encoded SENSE navigator correction. The bottom row shows difference images between the corresponding reconstructions and an artifact-free image. Histograms of the difference values are displayed as an inset in the bottom left corner of the difference images. Compared to nose touching experiments the increase in image quality between the zero order approach and the SENSE navigator approaches is less pronounced. The arrow points to an artifact at the posterior side of the brain that is reduced by SENSE navigator correction. Data are summarized in table 2 showing that frequency encoded and SENSE navigator correction leads to the best results.

DISCUSSION

The most important findings of this study are twofold. First, the use of sensitivity encoded and frequency encoded phase navigators leads to an improved estimation of inhomogeneous spatio-temporal magnetic field disturbances in the human brain compared to a conventional zeroth order navigator approach when strong field distortions are introduced. Second, it was shown that the image quality of heavily T_2^* -weighted acquisitions can be improved considerably by correcting for these inhomogeneities, caused primarily by patient motion outside of the imaging region.

The field map obtained during nose touching, see Figure 2 shows that the magnetic field disturbance is not homogeneous over the slice. There is a large variation between the anterior and posterior part of the brain. Consequently a global frequency estimate for the complete slice, as is obtained by a conventional zeroth order navigator, does not describe this magnetic field distribution adequately under this particular type of experiment. All the sig-

nals from the different receive coil elements that might reflect local changes, are effectively averaged in this case. Since the individual coil elements of the receive array sample only a small part of the brain, temporal changes in magnetic field can be detected and spatially resolved. If the coil elements are weighted according to their spatial sensitivity profile, low resolution spatio-temporal field change maps can be obtained, resulting in a more realistic estimation of the inhomogeneous field. When, in addition, frequency encoding of the navigator echo is used, field change estimations can be further improved. The field fluctuations introduced by nose touching are mainly oriented in the anterior-posterior direction. Therefore a frequency encoded navigator along that same direction without using coil sensitivity information already results in substantial improvements in estimating the magnetic field. In the present work significant improvements in the RSSD have been demonstrated for the SENSE and frequency encoded navigators. It should be noted that the EPI based method used to serve as a “ground truth” cannot be used for measuring magnetic field fluctuations in practical imaging studies because of the amount of time it takes to acquire the extra data. In addition the introduction of an extra RF pulse needed for the EPI readout also influences the magnetization, which is unwanted in most experiments. A navigator echo, on the other hand, can be used in a variety of imaging experiments through minor sequence adaptations. In the imaging experiments that are performed in this study, the navigator echo is acquired before the actual frequency encoding readout because of the long TE of the sequence and is part of a pre-phaser gradient already present in the sequence (see Figure 1). It does however limit the total time available for the imaging acquisition, therefore resulting in a signal-to-noise penalty. The time needed for the navigator can be minimized by sampling the navigator echo at a higher bandwidth (6) or by reducing the number of samples when no frequency encoding is required (19, 23). Due to the long imaging time needed for the EPI readout the TE_{nav} of the ground truth measurements is different from the imaging experiments

The artificially-induced changes in magnetic field distributions in this study were used to mimic (and amplify) spatio-temporal magnetic field fluctuations within a slice that have been observed in previous studies and serve as a worst case (2, 5, 6). Nose touching experiments result in substantial image degradation, as is shown in Figure 3 and 4, which result from the large variations in resonance frequency (up to 20 Hz). The image quality is considerably improved when zeroth order navigator echo correction is applied in line with previous findings in Alzheimer’s disease patients using a comparable sequence (6). However, some artifacts still remain after zeroth order navigator correction, which is indicative of a spatial distribution of the magnetic field

changes that is not captured accurately using the zeroth order navigator approach. The remaining artifacts are substantially reduced when a SENSE navigator or frequency encoded navigator correction technique was employed. The best performance was observed when frequency encoding of the coil sensitivity navigator was included. The artifacts caused by deep breathing were, in general, less severe than during nose touching and the improvements between SENSE navigator correction and zeroth order correction are less pronounced. This is likely due to the relatively homogeneous magnetic field distribution that is induced by breathing for transverse slices through the brain (1, 2, 5) and smaller amplitude of the magnetic field changes (typically less than 10 Hz). In the absence of artificially introduced magnetic field fluctuations, such as nose touching or deep breathing, small image quality improvements were observed for navigator correction compared to no correction: however, no differences were found between the performance of the different navigator techniques. Another advantage of the improved navigator approaches is that the unwrapped phase images, also show fewer artifacts when correction is applied and in addition improved performance of the phase unwrapping algorithm is observed. When navigator correction is applied, artifacts arising from rapid spatial phase variations are reduced and fewer remaining phase wraps are observed. These improved phase images can be particularly helpful in applications such as susceptibility weighted imaging.

It should be noted that, in order to enable the direct comparison of the different navigator techniques the zeroth order and SENSE navigator have been acquired in a suboptimal manner in the sense that although no frequency encoding information is required, all data are actually acquired using a frequency encoding gradient followed by complex summation in the spatial-temporal or temporal domains respectively, resulting in a reduction in SNR and increased sensitivity to motion.

The concept of acquiring navigator echoes using multiple receive channels is not entirely new. Non-phase encoded free induction decay signals, similar to navigator echoes have been used in recent publications for high temporal imaging, or B_0 shimming (21–23). Others have shown that by using multi-coil navigators, improvements in image quality could be obtained by retrospectively discarding and re-measuring k-space lines that contain signal corruption exceeding a certain threshold (29). In this case the navigator echoes were acquired using a dedicated RF excitation pulse interleaved with the imaging sequence. In our approach, rather than discarding and re-measuring data, the navigator based spatial field estimations are used for retrospective ima-

ge correction and therefore require no extra scanning time. It is expected that an even higher number of elements will result in further improvements in estimating the spatial magnetic field distribution.

Methods other than navigator echoes can be used to measure dynamic magnetic field fluctuations. External field probes positioned around the subject can be used to sample dynamically magnetic field changes using free induction decay signals (11, 12). These field probes can operate at a different resonance frequency (e.g. fluorine) than the imaging sequence, limiting the interaction with the imaging sequence and therefore requiring no additional scanning time (11). However the phase changes are measured outside of the brain and data are fitted to provide the field changes within the head (11, 12), leading to a possible reduction in accuracy. Furthermore, the hardware effort needed to support these field probes is substantial potentially limiting wide applicability. An advantage of the proposed navigator approach is that the phase changes are measured *within* the brain and that no additional hardware components are necessary.

Another method to measure dynamically fluctuations in the magnetic field is to relate the phase of the respiratory cycle to a certain magnetic field distribution. A calibration scan is used to measure the magnetic field distribution at different phases of the respiration cycle using an external belt. During imaging the shim settings are adjusted according to the respiration cycle (1). However, using this approach non-periodic field changes, such as body movements, yawning and coughing cannot be corrected. Our proposed method differs in that it does not make an assumption of the periodicity or origin of the magnetic field fluctuations since it measures the field distribution for each RF excitation. Furthermore, no additional calibration scan is needed. Care needs to be taken that the echo time of the navigator (TE_{nav}) is sufficiently small such that, given the amplitude of the expected magnetic field variations, no phase wraps occur. However, for very small values of TE_{nav} the sensitivity to magnetic field variations is reduced. The maximum detectable range of magnetic field variations corresponding to $TE_{nav} = 10$ ms is ± 50 Hz, conservatively set to be approximately twice the estimated/observed magnetic field changes.

The proposed reconstruction framework is similar to the technique described by Liu et al. (24) in the “extreme” form where each shot comprises the acquisition of only a single k-space line. Their technique has been implemented for self-navigated sequences, such as spiral or PROPELLOR (30), whereas in our case a separate navigator echo is acquired. The approach that is used in this study incorporates the spatial sensitivity information of multiple coils

in a receive array to improve the spatial reconstruction of a magnetic field distribution map. This has been shown using a similar acquisition approach with FID navigators before, but without using the application in retrospective image correction and without using frequency encoded navigators (23). Future work will focus on implementing this method to include a frequency encoding gradient to further increase the accuracy of the dynamic field estimations. Most sequences can be modified to allow for the inclusion of a navigator echo, especially when only a limited number of points are sampled (19), whereas only certain sequences can be modified to be self-navigated. Instead of using Cartesian navigators, spiral navigators have been used to dynamically measure low resolution field maps either by self-navigation through oversampling of the center of k-space (20, 24), through the separate acquisition of a spiral navigator echo (16, 31), or orbital navigators (32). These techniques have been applied successfully in diffusion weighted imaging to correct for phase errors or in structural imaging to correct for subject motion. However in these cases the spatial dependency of the individual coil elements is not taken into account and the proposed Cartesian navigators can be acquired in a shorter amount of time, especially when no frequency encoding gradient is required.

So far, most applications of phase correction have been in the field of diffusion weighted imaging (15, 16, 20, 31) or functional imaging (13, 14, 17, 18). Both applications are very sensitive to magnetic field induced phase changes or motion. However, as was shown previously, high field (i.e. 7 Tesla) causes more sequences to be sensitive to magnetic field induced phase changes (1, 6) because the amount of phase change is directly related to the magnetic field strength. Therefore, correction for magnetic field induced phase changes becomes important also for structural imaging at high field.

In principle the proposed technique is not limited to simple gradient echo sequences, but can easily be extended to other types of data acquisition. The reconstruction framework can be used with any method that estimates dynamic field changes. Although in this study the actual imaging sequence was not accelerated by parallel imaging, the iterative image reconstruction approach is also applicable to undersampled k-space data as was shown previously (24, 33)

CONCLUSION

Changes in the magnetic field distribution in the brain, caused by physiological and/or patient motion can seriously affect high field image quality. Correcting for these artifacts is important to obtain consistent image quality

in patient studies performed at high field. By intentionally introducing strong magnetic field distortions the performance of different navigator techniques was investigated. It was found that the combination of frequency encoded navigator echoes and coil sensitivity information (SENSE navigator echoes) improved the spatial and temporal estimation of the magnetic field distribution under these exaggerated conditions, such as nose touching and deep breathing, compared to conventional zeroth order navigator estimation. Prior information about the expected direction of strongest field gradients was used for the frequency encoded techniques. Under normal conditions in cooperative subjects all investigated navigator correction approaches worked equally well.

Therefore, the proposed SENSE and frequency navigator based image correction techniques are particularly valuable in T_2^* -weighted sequences at high magnetic field strengths acquired in non-cooperative subjects.

ACKNOWLEDGMENTS

The authors thank Jorik Blaas for helpful discussions on implementing the reconstruction algorithm.

REFERENCES

1. Van Gelderen P, de Zwart JA, Starewicz P, Hinks R, Duyn JH. Real-time shimming to compensate for respiration-induced B0 fluctuations. *Magnetic Resonance in Medicine* 2007 ;57:362–368.
2. Van de Moortele PF, Pfeuffer J, Glover GH, Ugurbil K, Hu X. Respiration-induced B0 fluctuations and their spatial distribution in the human brain at 7 Tesla. *Magnetic Resonance in Medicine* 2002 ;47:888–895.
3. Raj D, Anderson AW, Gore JC. Respiratory effects in human functional magnetic resonance imaging due to bulk susceptibility changes. *Physics in Medicine and Biology* 2001 ;46:3331–3340.
4. Birn RM, Bandettini PA, Cox RW, Jesmanowicz A, Shaker R. Magnetic field changes in the human brain due to swallowing or speaking. *Magnetic Resonance in Medicine* 1998 ;40:55–60.
5. Barry RL, Williams JM, Klassen LM, Gallivan JP, Culham JC, Menon RS. Evaluation of preprocessing steps to compensate for magnetic field distortions due to body movements in BOLD fMRI. *Magnetic Resonance Imaging* 2010 ;28:235–244.
6. Versluis MJ, Peeters JM, van Rooden S, van der Grond J, van Buchem MA, Webb AG, van Osch MJP. Origin and reduction of motion and f0 artifacts in high resolution T2*-weighted magnetic resonance imaging: Application in Alzheimer's disease patients. *NeuroImage* 2010 ;51:1082–1088.
7. Conijn MMA, Geerlings MI, Luijten PR, Zwanenburg JJM, Visser F, Biessels GJ, Hendrikse J. Visualization of cerebral microbleeds with dual-echo T2*-weighted magnetic resonance imaging at 7.0 T. *J. Magn. Reson. Imaging* 2010 ;32:52–59.
8. Marques JP, van der Zwaag W, Granziera C, Krueger G, Gruetter R. Cerebellar Cortical Layers: In Vivo Visualization with Structural High-Field-Strength MR Imaging. *Radiology* 2010 ;254:942–948.
9. Yao B, Li T-Q, Gelderen P van, Shmueli K, de Zwart JA, Duyn JH. Susceptibility contrast in high field MRI of human brain as a function of tissue iron content. *NeuroImage* 2009 ;44:1259–1266.
10. Zwanenburg JJM, Versluis MJ, Luijten PR, Petridou N. Fast high resolution whole brain T2* weighted imaging using echo planar imaging at 7 T. *NeuroImage* 2011 ;56:1902–1907.
11. Wilm BJ, Barmet C, Pavan M, Pruessmann KP. Higher order reconstruction for MRI in the presence of spatiotemporal field perturbations. *Magnetic Resonance in Medicine* 2011 ;65:1690–1701.
12. Barmet C, Zanche ND, Pruessmann KP. Spatiotemporal magnetic field monitoring for MR. *Magnetic Resonance in Medicine* 2008 ;60:187–197.
13. Barry RL, Martyn Klassen L, Williams JM, Menon RS. Hybrid two-dimensional navigator correction: A new technique to suppress respiratory-induced physiological noise in multi-shot echo-planar functional MRI. *NeuroImage* 2008 ;39:1142–1150.
14. Wowk B, McIntyre M C, Saunders J K. k-space detection and correction of physiological artifacts in fMRI. *Magnetic Resonance in Medicine* 1997 ;38:1029–1034.
15. Anderson AW, Gore JC. Analysis and correction of motion artifacts in diffusion weighted imaging. *Magn Reson Med* 1994 ;32:379–387.
16. Miller KL, Pauly JM. Nonlinear phase correction for navigated diffusion imaging. *Magnetic Resonance in Medicine* 2003 ;50:343–353.

17. Hu X, Kim S-G. Reduction of signal fluctuation in functional MRI using navigator echoes. *Magnetic Resonance in Medicine* 1994 ;31:495–503.
18. Durand E, Van de Moortele PF, Pachot-Clouard M, Le Bihan D. Artifact due to B0 fluctuations in fMRI: Correction using the k-space central line. *Magnetic Resonance in Medicine* 2001 ;46:198–201.
19. Brau ACS, Brittain JH. Generalized self-navigated motion detection technique: Preliminary investigation in abdominal imaging. *Magnetic Resonance in Medicine* 2006 ;55:263–270.
20. Liu C, Bammer R, Kim D, Moseley ME. Self-navigated interleaved spiral (SNAILS): Application to high-resolution diffusion tensor imaging. *Magnetic Resonance in Medicine* 2004 ;52:1388–1396.
21. Lin F, Wald LL, Ahlfors SP, Hämäläinen MS, Kwong KK, Belliveau JW. Dynamic magnetic resonance inverse imaging of human brain function. *Magnetic Resonance in Medicine* 2006 ;56:787–802.
22. Hennig J, Zhong K, Speck O. MR-Encephalography: Fast multi-channel monitoring of brain physiology with magnetic resonance. *NeuroImage* 2007 ;34:212–219.
23. Splitthoff DN, Zaitsev M. SENSE shimless (SSH): A fast approach for determining B0 field inhomogeneities using sensitivity coding. *Magn. Reson. Med.* 2009 ;62:1319–1325.
24. Liu C, Moseley ME, Bammer R. Simultaneous phase correction and SENSE reconstruction for navigated multi-shot DWI with non-cartesian k-space sampling. *Magnetic Resonance in Medicine* 2005 ;54:1412–1422.
25. Sutton BP, Noll DC, Fessler JA. Fast, iterative image reconstruction for MRI in the presence of field inhomogeneities. *IEEE Trans Med Imaging* 2003 ;22:178–188.
26. Fong D, Saunders M. LSMR: An iterative algorithm for sparse least-squares problems [Internet]. arXiv:1006.0758 2010 ;
27. Roemer PB, Edelstein WA, Hayes CE, Souza SP, Mueller OM. The NMR phased array. *Magn Reson Med* 1990 ;16:192–225.
28. Rauscher A, Barth M, Herrmann K-H, Witoszynski S, Deistung A, Reichenbach J. Improved elimination of phase effects from background field inhomogeneities for susceptibility weighted imaging at high magnetic field strengths. *Magnetic Resonance Imaging* 2008 ;26:1145–1151.
29. Kober T, Marques JP, Gruetter R, Krueger G. Head motion detection using FID navigators. *Magnetic Resonance in Medicine* 2011 ;66:135–143.
30. Pipe JG, Farthing VG, Forbes KP. Multishot diffusion-weighted FSE using PROPELLER MRI. *Magn Reson Med* 2002 ;47:42–52.
31. Van A, Hernando D, Sutton B. Motion-Induced Phase Error Estimation and Correction for 3D Diffusion Tensor Imaging [Internet]. *IEEE Trans Med Imaging* 2011 ;
32. Moriguchi H, Lewin JS, Duerk JL. Novel interleaved spiral imaging motion correction technique using orbital navigators. *Magnetic Resonance in Medicine* 2003 ;50:423–428.
33. Pruessmann KP, Weiger M, Börner P, Boesiger P. Advances in sensitivity encoding with arbitrary k-space trajectories. *Magnetic Resonance in Medicine* 2001 ;46:638–651.

7

Fast high resolution whole brain T_2^* weighted imaging using echo planar imaging at 7 Tesla

*J.J.M. Zwanenburg
M.J. Versluis
P.R. Lijten
N. Petridou*

ABSTRACT

Magnetic susceptibility based (T_2^* -weighted) contrast in MRI at high magnetic field strength is of great value in research on brain structure and cortical architecture, but its use is hampered by the low signal-to-noise ratio (SNR) efficiency of the conventional spoiled gradient echo sequence (GRE) leading to long scan times even for a limited number of slices. In this work, we show that high resolution (0.5 mm isotropic) T_2^* -weighted images of the whole brain can be obtained in 6 min by utilizing the high SNR efficiency of echo-planar imaging (EPI). A volumetric (3D) EPI protocol is presented and compared to conventional 3D GRE images acquired with the same resolution, amount of T_2^* -weighting, and imaging duration. Spatial coverage in 3D EPI was increased by a factor of 4.5 compared to 3D GRE, while also the SNR was increased by a factor of 2. Image contrast for both magnitude and phase between gray and white matter was similar for both sequences, with enhanced conspicuity of anatomic details in the 3D EPI images due to the increased SNR. Even at 7 T, image blurring and distortion is limited if the EPI train length remains short (not longer than the T_2^* of the imaged tissue). 3D EPI provides steps (speed, whole brain coverage, and high isotropic resolution) that are necessary to utilize the benefits of high field MRI in research that employs T_2^* -weighted imaging.

INTRODUCTION

Magnetic resonance imaging (MRI) with susceptibility-based contrast at high magnetic field strength has allowed the visualization of human brain anatomy in vivo with exceptional detail. Variations in magnetic susceptibility of tissue (manifested as T_2^* and frequency variations) yield clear contrast between different anatomical structures in T_2^* -weighted magnitude images both in white matter (e.g. fiber bundles (1)) and gray matter (e.g. basal ganglia (2)). The phase of T_2^* weighted images is even more sensitive to magnetic susceptibility variations. Using the phase, it is possible to depict exquisite details of cortical structure and substructure, including the line of Gennari in the visual cortex (3–5). The magnetic susceptibility of tissue depends on the presence and arrangement of, amongst others, lipids, proteins and (non-heme) iron in the tissue (6, 7). T_2^* -weighted imaging at high field is, therefore, sensitive to the tissue composition at a cellular level, yielding a powerful tool to study normal and pathological tissue (8–11).

T_2^* -weighted imaging is conventionally performed using a spoiled gradient echo (GRE) sequence (12). At the high resolutions employed to image structural detail ($\ll 1$ mm³ voxel volume), however, imaging time is long, even for a limited number of slices (3). As a result, the imaging volume is typically limited since full brain coverage requires excessively long scan times of 1 h or more for a single acquisition. This hampers the practical use of T_2^* -weighted imaging for fundamental research of normal physiology or disease. Long imaging times are also problematic because they increase the possibility of subject motion during the scan duration resulting in blurring or unusable images (13). The long imaging times are due to the relatively low signal-to-noise ratio (SNR) efficiency of the spoiled GRE sequence. For sufficient T_2^* weighting, a long echo time (TE) is needed, which leads to 'dead' time in the sequence during which no signal is acquired.

In this work, we show that high resolution T_2^* -weighted images of the whole brain can be obtained in 6 min based on volumetric (3D) echo-planar imaging (EPI) by utilizing the high SNR efficiency of EPI (14). By using a multi-shot approach with short EPI train lengths, the common artifacts related to EPI (distortion and blurring) are limited, and images with a considerable gain in both SNR and coverage as compared to GRE imaging can be obtained within a given amount of scan time. The contrast in the phase and magnitude 3D EPI images and the distortion are compared with 3D GRE images, acquired with the same acquisition parameters in terms of resolution, amount of T_2^* -weighting, and imaging duration.

MATERIALS AND METHODS

Imaging was performed on 8 healthy subjects (4 male, 4 female, age 27 ± 4 years) who gave written informed consent, in accordance to the Institutional Review Board of the University Medical Center Utrecht. Images were acquired using a 7 T MRI system (Philips Healthcare, Cleveland, USA) with a 16 channel receive coil and a volume transmit coil (Nova Medical, Wilmington, MA). Maximum gradient strength and slew rate were 33 mT/m and 166 T/m/s, respectively. For all sequences 3rd order B_0 shimming was performed using an image based approach with an adapted version of the tool developed by (15). The amplitude of the RF transmit field (B_1) was measured with actual flip angle imaging in the pulsed steady state (16) in order to assess the spatial variations in the RF transmit field across the brain, using the following parameters: TR1/TR2/TE 25/125/2.5 ms, flip angle 50°, voxel size $3.8 \times 3.7 \times 4$ mm³, 20 slices, field of view 240×195 mm². For good T_2^* contrast, the TE of the T_2^* -weighted sequences was chosen to be equal to the average T_2^* of white matter at 7 T: 27 ms (17), which is in between the (on average longer) T_2^* of cortical gray matter and the (on average shorter) T_2^* of the iron containing nuclei of the basal ganglia.

3D EPI protocol

A 3D T_2^* -weighted protocol was set up with 0.5 mm isotropic resolution (125 nl voxel volume) and whole brain coverage, with a total scan duration of less than 6 min. Multi-shot 3D EPI was used with a conventional Cartesian interleaved k -space trajectory. During each EPI shot, the y gradient (left–right (LR) encoding) was stepped, for a given k_z (linearly increasing phase encoding step in the feet–head direction). The EPI factor was set to 13, leading to an EPI train length of 23 ms, below the average T_2^* for gray and white matter (17). Fat-suppression was applied to avoid possible artifacts that may arise from a shifted fat signal in combination with sensitivity encoding (SENSE) with the small receive coils, which have a rapidly varying sensitivity at the location of the subcutaneous fat. For fat-suppression Spectral Presaturation Inversion Recovery (SPIR) was applied with a non-selective RF pulse of 110° flip angle, 679 Hz BW and a frequency offset of 1.1 kHz. The flip angle of the imaging sequence was set to a value which was 33% larger than the Ernst angle for gray matter given the TR (see Table 1). This choice was made to partly compensate for the fact that the actual B_1 as assessed from the B_1 maps was about 80% of the nominal value (20 μ T) in the center of the brain, and even less elsewhere. The Ernst angle was computed using the T_1 value for cortical gray matter at 7T, $T_1 = 2132$ ms (18). The flip angle was optimized for gray matter (GM), as GM has a longer T_1 and thus less signal, relative to white

matter (WM). The imaging parameters are shown in Table 1.

Table 1: Imaging parameters.				
	3D EPI	3D GRE	2D EPI	2D GRE
FOV (mm ²)	240 × 192	240 × 192	240 × 190	240 × 190
Matrix (AP × RL)	480 × 381	480 × 384	300 × 234	300 × 237
Resolution (mm ²)	0.5 × 0.5	0.5 × 0.5	0.8 × 0.8	0.8 × 0.8
Slice thickness (mm)	0.5	0.5	2	2
Nr slices	300	66	1	1
Coverage (FH direction, mm)	150	33	2	2
Flip angle	19°	13°	15°	15°
TR/TE (ms)	70/27	32/27	70/27	70/27
BW readout direction (Hz/pixel)	677	203	997	1080
BW phase encoding direction (Hz/pixel)	41	–	57	–
EPI factor	13	–	13	–
Repetitions ^a	–	–	26	2
Slice-oversampling factor	1.28	1.28	–	–
k-space shutter (sampled fraction of k-space)	1.0	0.78	1.0	1.0
SENSE (LR)	2.3	2.3	1.0	1.0
Fat suppression	SPIR	None	SPIR	SPIR
Scan time (s)	350	354	33.3	33.9

FOV: field-of-view, AP: anterior–posterior, RL: left–right, FH: feet–head, TR: repetition time, TE: echo time, BW: bandwidth, SENSE: parallel imaging acceleration factor (sensitivity encoding), SPIR: spectral presaturation by inversion recovery. ^a Last repetition is performed without applying any RF or gradient pulses in order to measure the noise.

3D GRE protocol

As a reference for image quality, a GRE imaging protocol was set up with the same resolution, TE and scan duration as the EPI protocol (Table 1). The bandwidth was chosen to obtain optimal SNR for the GRE images, and was equivalent to that used for the combined time-of-flight/susceptibility weighted clinical imaging protocols in our hospital (19). Given the scan duration, coverage for the GRE protocol was maximized by choosing the shortest possible repetition time (TR), and adapting the flip angle accordingly. Fat suppression was omitted to further shorten the TR within the specific absorption rate (SAR) constraints. A vendor supplied elliptical shutter in k -space was

applied with GRE, which means that approximately 22% of the data in the edges with both high k_y and high k_z values were not sampled. Given the scan duration, this allows to further increase the coverage with a limited cost in resolution.

Quantitative comparison between 3D EPI and 3D GRE images

The 3D EPI and GRE images were reconstructed with image homogeneity correction, using the standard reconstruction software of the scanner. Both magnitude and phase images were stored. Phase images were high-pass filtered by subtracting a 2nd order polynomial fit from the phase data in order to remove large length-scale fields over the whole image. Varying fields toward the edge of the image were filtered by modeling these fields with dipole point sources parallel to the main field (B_0) and subtracting a least-squares fit from the phase data, as described in Wharton et al. (20) The 3D EPI images were compared to the GRE images to assess the image quality and contrast, for both magnitude and phase.

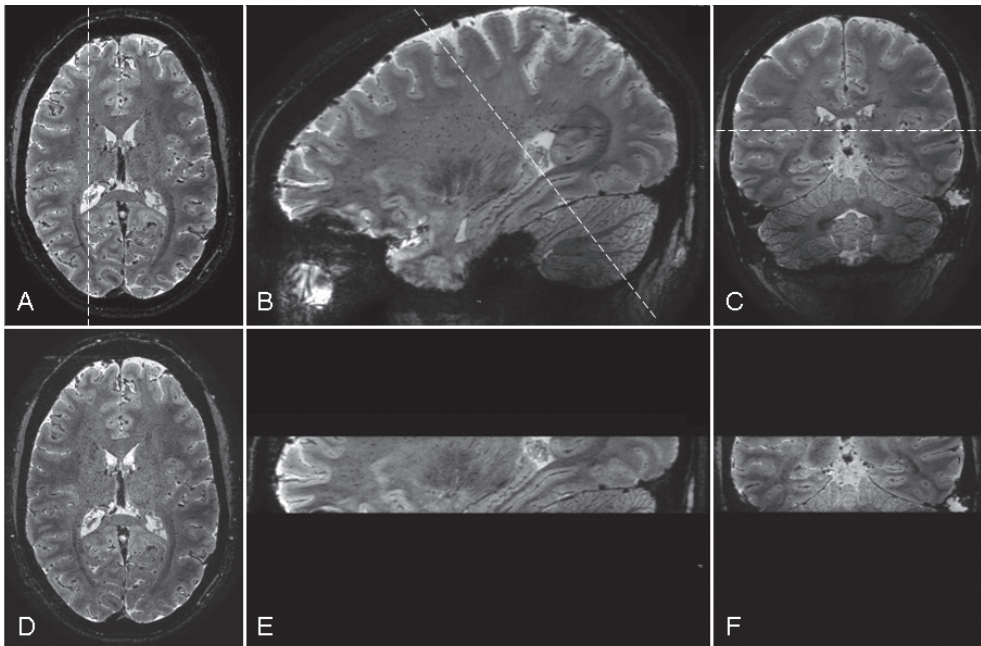


Figure 1: Magnitude images of the 3D EPI protocol

(A: transverse, B: sagittal, C: coronal orientation), showing the gain in coverage and SNR as compared to the 3D GRE imaging protocol (D, E and F). Note that the EPI and GRE images are acquired with the same scan duration and resolution. The dotted lines indicate the perpendicular cross-sections of the different orientations. Some blurring can be seen for the GM just above the nasal cavity in panel B.

The contrast between GM and WM in the two sequences was compared for regions of interest (ROIs) in three different regions (GM vs. WM): cingulate gyrus vs. corpus callosum, putamen vs. internal capsule, and GM vs. WM in the primary visual cortex. The contrast in the magnitude images was defined as the signal of GM divided by the signal of WM. This signal ratio was chosen, because the conventional measure of contrast, $SNR_{GM} - SNR_{WM}$ is directly affected by the overall difference in SNR between the two sequences. The contrast in the phase images was quantified as the frequency difference in Hz, which was obtained by dividing the phase in radians by $2\pi TE$.

The distortion in the EPI images was assessed by overlaying the outer contour of the GM in the 3D GRE image over the corresponding 3D EPI image. To remove any contribution from head motion between the scans, the 3D GRE images were registered to the 3D EPI images with rigid body registration using the FSL software package (FSL 4.1, FMRIB's Software Library, Oxford (21)). After registration, the maximum mismatch between the GRE contour and the EPI image was measured in the phase encoding (LR) direction for both the lowest and the highest slice in the GRE dataset.

To confirm that the EPI and GRE performance is equivalent if all imaging parameters are the same, we performed a 2D experiment where the only difference was the scan duration (due to the EPI factor). The imaging parameters are given in Table 1. The noise level was measured by repeating the data acquisition with the same receiver gain and bandwidth for data sampling, without applying any RF or gradient pulses. The EPI scan was repeated multiple times in dynamic mode, in order to obtain a steady state signal for correct comparison of the SNR level between EPI and GRE imaging. The 2D EPI and GRE images were used to measure the SNR in an ROI covering the complete brain. The noise level was quantified as the standard deviation in a corresponding ROI in the image with sampled noise.

RESULTS

The image quality was consistent for all volunteers for both the 3D EPI and the 3D GRE protocol. The remarkable improvements in both coverage and SNR that are obtained with the 3D EPI protocol are illustrated in Fig. 1. Note the clear depiction of the cerebellum, and the clear visualization of the hippocampus in the 3D EPI images. The contrast in both the magnitude and phase images between GM and WM was similar between 3D EPI and 3D GRE, as shown in Table 2. Fig. 2 and Fig. 3 illustrate the improved image SNR with 3D EPI, for sample areas in the basal ganglia and the visual cortex. The higher SNR in the 3D EPI magnitude images yields improved visualization of tissue

borders, for example between white matter and the putamen, hippocampus and substantia nigra (Fig. 2). Also the optic radiations are delineated more clearly as they fuse into the primary visual cortex (Fig. 3). In analogy to the magnitude images, the higher SNR obtained with 3D EPI yields clearer phase images, which allows enhanced visualization of subtle details such as the line of Gennari in the visual cortex (Fig. 3). Artifacts from incomplete phase unwrapping are similar between both protocols, e.g. posteriorly around the edges of the cortex (Fig. 2 and Fig. 3).

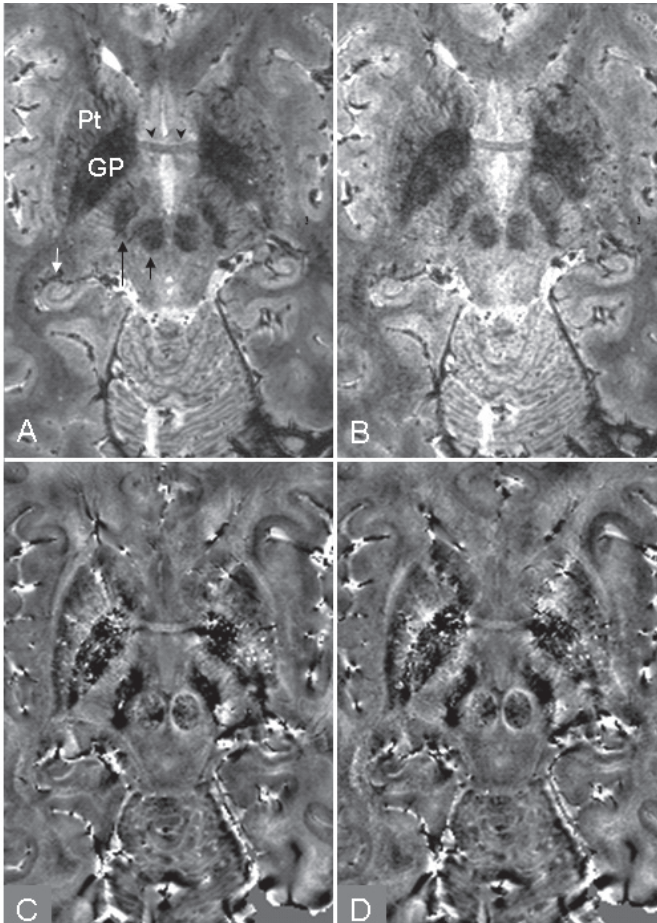


Figure 2: Detail of transverse 3D EPI vs. 3D GRE images.

Visible are many anatomical structures, including the putamen (Pt) and globus pallidus (GP) in the lentiform nucleus, the anterior commissure (black arrow heads), substantia nigra (long black arrow), the nucleus ruber (short black arrow) and the hippocampus (white arrow). Left: 3D EPI magnitude (A) and phase (C). Right: 3D GRE magnitude (B) and phase (D).

Maximum image distortions measured in the 3D EPI images, were 2.2 ± 0.5 mm and 1.1 ± 0.2 mm for the slice corresponding to the lowest and

highest slice in the 3D GRE volume, respectively. The maximum distortion was usually observed as a very localized distortion (as illustrated in Fig. 4). In many cases, particularly away from bone/air-tissue interfaces, the distortion (if present) was less than 0.5 mm (pixel size). An example of the distortion is given in Fig. 4. In the slices close to the skull base, the border between GM and WM appeared less sharp in the EPI images, as can be seen in the frontal area above the nasal cavities in Fig. 1.

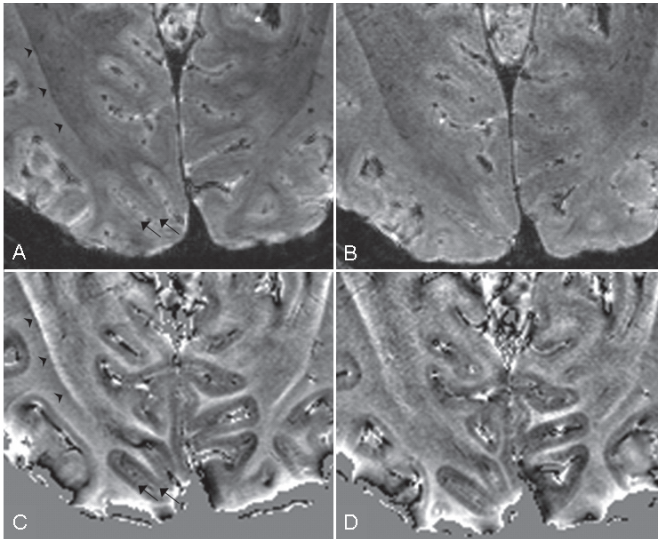


Figure 3: Detail of transverse 3D EPI vs. 3D GRE images, showing part of the visual cortex. Left: 3D EPI magnitude (A) and phase (C). Right: 3D GRE magnitude (B) and phase (D). The black arrows in the EPI phase image (C) indicate the line of Gennari, and the arrow heads point to the clear delineation of the optic radiations.

The 2D EPI images had similar SNR (15.8 ± 0.6) as the 2D GRE images (14.9 ± 0.5) (mean \pm standard deviation across subjects, $n = 8$), despite the fact that they were acquired 13 times faster. Hence, the SNR efficiency of the 2D EPI protocol was approximately $\sqrt{13}$ larger than that of 2D GRE protocol, as expected.

DISCUSSION

The high SNR efficiency of EPI was used to develop a fast 3D T_2^* -weighted anatomical imaging protocol, providing whole brain coverage with 0.5 mm isotropic resolution in less than 6 min. Given a fixed amount of scan time, the 3D EPI protocol yields more than a four-fold increase in coverage (150 mm vs. 33 mm for 3D GRE imaging), and also higher SNR. The higher SNR allows enhanced visualization of fine anatomical detail (Fig. 2 and Fig. 3), while the

isotropic resolution allows reformatting of the data in any desired orientation (Fig. 1).

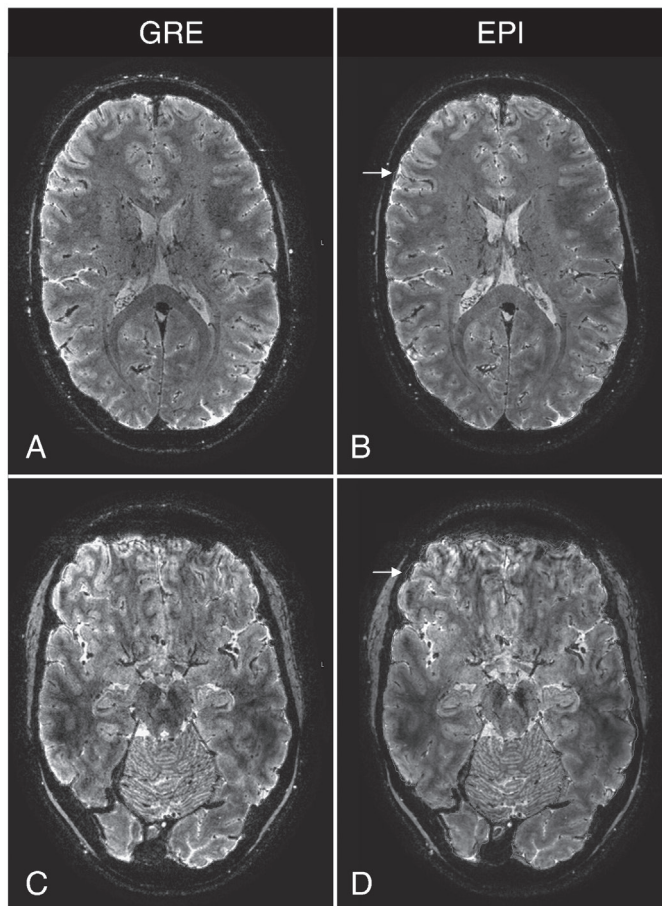


Figure 4: Amount of distortions on GRE and EPI dataset.

Example data showing the highest and lowest slices of a 3D GRE data set (panels A and C, respectively) and the corresponding slices in the 3D EPI data set (panels B and D, respectively). The outer contours of the brain as drawn on the GRE images are superimposed on the EPI images to assess the amount of distortion. The arrows indicate the location of maximum distortion in the phase encoding direction (1.4mm for the highest slice, B, and 2.7 mm for the lowest slice, D).

To date, the high SNR efficiency of EPI is almost exclusively used for functional MRI (fMRI), to capture the dynamic signal changes associated with brain activity. Recently, it was shown that 3D EPI imaging is more efficient than multi-slice (2D) EPI, in the context of fMRI applications (22). The current results show that the high SNR efficiency of 3D EPI is also valuable for application in structural imaging, an application for which the use of EPI seems to be underappreciated.

Table 2. Contrast between GM and WM for both 3D EPI and 3D GRE images.

	3D EPI magnitude	3D GRE magnitude	3D EPI phase (Hz)	3D GRE phase (Hz)
CG vs. CC	1.7 ± 0.2	1.7 ± 0.2	- 0.3 ± 0.7	- 0.2 ± 0.5
Pt vs. IC	0.8 ± 0.1	0.8 ± 0.1	- 2.6 ± 0.4	- 2.4 ± 0.5
GM _{vc} vs. WM _{vc}	1.2 ± 0.2	1.1 ± 0.1	- 3.4 ± 1.0	- 3.5 ± 1.2

CG: cingulated gyrus, CC: corpus callosum, Pt: putamen, IC: internal capsule, GM_{vc}/WM_{vc}: gray matter/white matter of visual cortex. For magnitude: ratio of gray matter signal over white matter signal, for phase: difference in phase, expressed as a frequency difference (using TE = 27 ms).

SNR efficiency, point spread broadening and distortion

The SNR efficiency of the 3D EPI protocol presented here (Table 1) resulted in a gain in SNR by a factor of 2 relative to the 3D GRE protocol. The relative SNR was calculated by $s = (1 - E_1) E_2 \sin \alpha / (1 - E_1 \cos \alpha)$ (23) and the dependency of the SNR on voxel volume (Δxyz), number of samples acquired ($N_x N_y N_z$) and bandwidth (BW): $S \Delta xyz \sqrt{((N_x N_y N_z)/BW)}$, where $E_1 = \exp(- TR/T_1)$, $E_2 = \exp(- TE/T_2^*)$ and α is the flip angle.

The main reason why GRE imaging has a much lower SNR efficiency than EPI, is that GRE imaging performs data sampling only during a fraction of the ‘lifetime of the signal’, T_2^* , while EPI samples the signal over a much longer duration. The limiting factor for imaging speed with EPI is, therefore, the T_2^* of the tissue. We chose an EPI factor of 13, leading to an EPI train length of 23 ms, which is just below the T_2^* for most brain tissues. Long echo trains will reduce the efficiency of EPI, because in the extreme case, only noise is sampled, while shorter echo trains are still sub-optimal. There is a trade-off between EPI train length and image blurring or point spread widening, due to T_2^* decay during the readout. Using an EPI train length equal to the T_2^* of the imaged tissue, the broadening of the point spread function is less than 5% (24). For longer train lengths, or for tissues with shorter T_2^* , for example as may occur in regions with poor shimming such as above the nasal cavities

(Fig. 1), blurring can become noticeable.

The 3D GRE bandwidth could be reduced to such extent that the SNR efficiency of the 3D GRE protocol would become equal to that of the 3D EPI protocol (3). However, the total scan time for whole brain coverage would still be long, as the increased SNR efficiency obtained in this way cannot be traded off directly against imaging speed, as is the case for EPI.

The 3D EPI images showed only limited distortion, with a maximum observed distortion of 2.5 ± 0.5 mm for the lowest slice of the 3D GRE volume. This might be counter-intuitive, as EPI is well known to suffer from distortion. However, the amount of distortion depends strongly on the echo train length. With the echo train length used in this study, the BW in the phase encoding direction is 41 Hz, which corresponds to a displacement of 2.5 pixels (1.25 mm) per 100 Hz off-resonance. In our experience, using image based shimming at 7 T, the standard deviation of the off-resonance frequency distribution in the shimmed brain volume is around 60 Hz after shimming. In regions close to the nasal cavity and petrous bones, distortion will be strongest, and local gradients will lead to an apparently shorter T_2^* and hence to noticeable blurring, which can be problematic for studies involving these regions.

The lower bandwidth for EPI sequences in the phase encoding direction results in larger water–fat shifts, which can be a disadvantage. However, because of the increased TR and the acquisition of multiple lines with each RF excitation, it is possible to include fat suppression or saturation slabs while still remaining within the SAR constraints, which are more easily reached at higher magnetic field strengths.

Implications

T_2^* -weighted imaging provides valuable information in the study of both normal brain physiology and disease, as these images reflect brain tissue microstructure (4, 6, 25, 26). Neurodegenerative diseases in particular are associated with elevated iron depositions to which T_2^* -weighted imaging is extremely sensitive (8–11). Unfortunately, patients with neurodegenerative diseases often have difficulties lying still for more than a few minutes, while T_2^* weighted imaging is prone to motion artifacts (13). The proposed protocol is fast and will, hence, allow increased coverage in acceptable scanning time, or fast scanning of a limited brain area with lower chance of motion artifacts. Further reduction in scan time is expected from coils with more receive elements, which will allow for higher acceleration factors from parallel imaging. 3D EPI allows fast mapping of phase contrast and can hence con-

tribute to research on the origins of this contrast (27), as well as to accurate susceptibility mapping (20). 3D EPI using non-isotropic voxel sizes may prove beneficial for venography based on susceptibility-weighted imaging (28).

CONCLUSION

Fast T_2^* -weighted anatomical imaging with high resolution and full brain coverage was obtained with 3D multi-shot EPI imaging. Spatial coverage and image signal to noise ratio is markedly improved compared to conventional 3D GRE imaging, given a fixed scan time and resolution, while image blurring and distortion are limited if the EPI train length remains short (not longer than the T_2^* of the imaged tissue). 3D EPI provides steps (speed, whole brain coverage, and high isotropic resolution) that are necessary to utilize the benefits of high field MRI in research that employs T_2^* -weighted imaging.

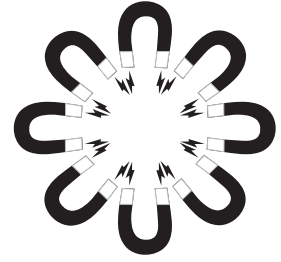
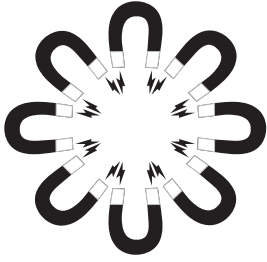
ACKNOWLEDGMENTS

The authors would like to thank F. Visser and Dr. J.J.M. Hoogduin for the constructive discussions on this topic.

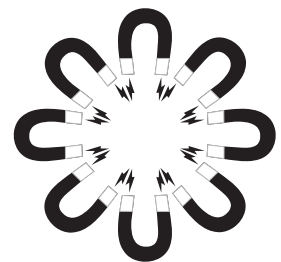
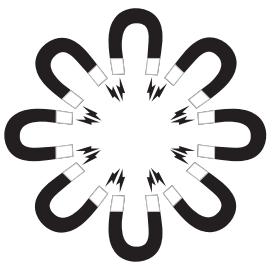
REFERENCES

1. Li T-Q, van Gelderen P, Merkle H, Talagala L, Koretsky AP, Duyn J. Extensive heterogeneity in white matter intensity in high-resolution T2*-weighted MRI of the human brain at 7.0 T. *NeuroImage* 2006 ;32:1032–1040.
2. Cho Z-H, Min H-K, Oh S-H, Han J-Y, Park C-W, Chi J-G, Kim Y-B, Paek SH, Lozano AM, Lee KH. Direct visualization of deep brain stimulation targets in Parkinson disease with the use of 7-tesla magnetic resonance imaging. *Journal of Neurosurgery* 2010 ;113:639–647.
3. Duyn JH, van Gelderen P, Li T-Q, de Zwart JA, Koretsky AP, Fukunaga M. High-field MRI of brain cortical substructure based on signal phase. *Proceedings of the National Academy of Sciences* 2007 ;104:11796–11801.
4. Fukunaga M, Li T-Q, van Gelderen P, de Zwart JA, Shmueli K, Yao B, Lee J, Maric D, Aronova MA, Zhang G, Leapman RD, Schenck JF, Merkle H, Duyn JH. Layer-specific variation of iron content in cerebral cortex as a source of MRI contrast. *Proceedings of the National Academy of Sciences* 2010 ;107:3834 –3839.
5. Haacke EM, Cheng NYC, House MJ, Liu Q, Neelavalli J, Ogg RJ, Khan A, Ayaz M, Kirsch W, Obenaus A. Imaging iron stores in the brain using magnetic resonance imaging. *Magnetic Resonance Imaging* 2005 ;23:1–25.
6. He X, Yablonskiy DA. Biophysical mechanisms of phase contrast in gradient echo MRI. *Proc Natl Acad Sci U S A* 2009 ;106:13558–13563.
7. Zhong K, Leupold J, von Elverfeldt D, Speck O. The molecular basis for gray and white matter contrast in phase imaging. *Neuroimage* 2008 ;40:1561–6.
8. Bartzokis G, Cummings J, Perlman S, Hance DB, Mintz J. Increased Basal Ganglia Iron Levels in Huntington Disease. *Arch Neurol* 1999 ;56:569–574.
9. Mainero C, Benner T, Radding A, van der Kouwe A, Jensen R, Rosen BR, Kinkel RP. In vivo imaging of cortical pathology in multiple sclerosis using ultra-high field MRI. *Neurology* 2009 ;73:941–948.
10. Stankiewicz J, Panter SS, Neema M, Arora A, Batt CE, Bakshi R. Iron in chronic brain disorders: imaging and neurotherapeutic implications. *Neurotherapeutics* 2007 ;4:371–86.
11. van Rooden S, Maat-Schieman MLC, Nabuurs RJA, van der Weerd L, van Duijn S, van Duinen SG, Natté R, van Buchem MA, van der Grond J. Cerebral Amyloidosis: Postmortem Detection with Human 7.0-T MR Imaging System. *Radiology* 2009 ;253:788–796.
12. Haase A, Frahm J, Matthaei D, Hanicke W, Merboldt K-D. FLASH imaging. Rapid NMR imaging using low flip-angle pulses. *Journal of Magnetic Resonance (1969)* 1986 ;67:258–266.
13. Versluis MJ, Peeters JM, van Rooden S, van der Grond J, van Buchem MA, Webb AG, van Osch MJP. Origin and reduction of motion and f0 artifacts in high resolution T2*-weighted magnetic resonance imaging: Application in Alzheimer’s disease patients. *NeuroImage* 2010 ;51:1082–1088.
14. Mansfield P, Maudsley AA, Bains T. Fast scan proton density imaging by NMR. *Journal of Physics E: Scientific Instruments* 1976 ;9:271.
15. Schär M, Kozerke S, Fischer SE, Boesiger P. Cardiac SSFP imaging at 3 Tesla. *Magnetic Resonance in Medicine* 2004 ;51:799–806.

16. Yarnykh VL. Actual flip-angle imaging in the pulsed steady state: A method for rapid three-dimensional mapping of the transmitted radiofrequency field. *Magnetic Resonance in Medicine* 2007 ;57:192–200.
17. Peters AM, Brookes MJ, Hoogenraad FG, Gowland PA, Francis ST, Morris PG, Bowtell R. T_2^* measurements in human brain at 1.5, 3 and 7 T. *Magnetic Resonance Imaging* 2007 ;25:748–753.
18. Rooney WD, Johnson G, Li X, Cohen ER, Kim S-G, Ugurbil K, Jr CSS. Magnetic field and tissue dependencies of human brain longitudinal H_2O relaxation in vivo. *Magnetic Resonance in Medicine* 2007 ;57:308–318.
19. Conijn MMA, Geerlings MI, Luijten PR, Zwanenburg JJM, Visser F, Biessels GJ, Hendrikse J. Visualization of cerebral microbleeds with dual-echo T_2^* -weighted magnetic resonance imaging at 7.0 T. *J. Magn. Reson. Imaging* 2010 ;32:52–59.
20. Wharton S, Schäfer A, Bowtell R. Susceptibility mapping in the human brain using threshold-based k-space division. *Magnetic Resonance in Medicine* 2010 ;63:1292–1304.
21. Jenkinson M, Bannister P, Brady M, Smith S. Improved optimization for the robust and accurate linear registration and motion correction of brain images. *Neuroimage* 2002 ;17:825–841.
22. Poser BA, Koopmans PJ, Witzel T, Wald LL, Barth M. Three dimensional echo-planar imaging at 7 Tesla. *NeuroImage* 2010 ;51:261–266.
23. Ernst RR, Anderson WA. Application of Fourier transform spectroscopy to magnetic resonance. *Review of Scientific Instruments* 1966 ;37:93–102.
24. Haacke EM. The effects of finite sampling in spin-echo or field-echo magnetic resonance imaging. *Magn Reson Med* 1987 ;4:407–421.
25. Lee J, Shmueli K, Fukunaga M, van Gelderen P, Merkle H, Silva AC, Duyn JH. Sensitivity of MRI resonance frequency to the orientation of brain tissue microstructure. *Proceedings of the National Academy of Sciences* 2010 ;107:5130–5135.
26. Reichenbach JR, Venkatesan R, Yablonskiy DA, Thompson MR, Lai S, Haacke EM. Theory and application of static field inhomogeneity effects in gradient-echo imaging. *J Magn Reson Imaging* 7:266–79.
27. Petridou N, Wharton SJ, Lotfipour A, Gowland P, Bowtell R. Investigating the effect of blood susceptibility on phase contrast in the human brain. *NeuroImage* 2010 ;50:491–498.
28. Haacke EM, Xu Y, Cheng Y-CN, Reichenbach JR. Susceptibility weighted imaging (SWI). *Magnetic Resonance in Medicine* 2004 ;52:612–618.



Clinical applications of 7 Tesla MRI



8

Cortical phase changes in Alzheimer's disease at 7 Tesla MRI: a novel imaging marker

*S. van Rooden
M.J. Versluis
M.K. Liem
J. Milles
A.B. Maier
A.M.Oleksik
A.G. Webb
M.A. van Buchem
J. van der Grond*

ABSTRACT

Background

Post mortem studies have indicated the potential of high-field magnetic resonance imaging (MRI) to visualize amyloid depositions in the cerebral cortex. The aim of this study is to test this hypothesis in patients with Alzheimer's disease (AD).

Methods

T_2^* -weighted MRI was performed in 15 AD patients and 16 control subjects. All MRI scans were scored qualitatively by visual assessment and quantitatively by measuring phase shifts in the cortical gray matter and hippocampus. Statistical analysis was performed to assess differences between groups.

Results

Patients with AD demonstrated an increased phase shift in the cortex in temporoparietal, frontal, and parietal regions ($p < 0.005$) and this was associated with the individual Mini Mental State Examination ($r = -0.54$, $p < 0.05$).

Discussion

Increased cortical phase shift in AD patients demonstrated on 7 Tesla T_2^* -weighted MRI is a potential new biomarker for AD, which may reflect amyloid pathology in the early stages.

INTRODUCTION

Alzheimer's disease (AD) can only be diagnosed with certainty at autopsy, based on the histological detection of senile plaques containing fibrillary amyloid- β (A β) and neurofibrillary tangles. Currently, due to the absence of validated sensitive and specific tests, the clinical diagnosis of AD can only be made at a late stage of disease progression and with a considerable degree of uncertainty, "probable AD" at best, and is based on criteria from the Diagnostic and Statistical Manual of Mental Disorders (DSM-IV) and the National Institute of Neurologic, Communicative Disorders and Stroke-AD and Related Disorders Association (NINCDS-ADRDA). Nevertheless, the histological hallmarks of AD pathology, comprising amyloid plaques and neurofibrillary tangles, are known to occur up to 10 to 20 years before the objective detection of cognitive decline (1). Recently, positron emission tomography (PET) using Pittsburgh compound-B (PiB) has been introduced as a diagnostic tool to detect cerebral amyloid in-vivo (2–8). The major disadvantages of PiB-PET are the need to use a radioactive tracer, the relative scarcity of institutions that can perform such scans due to the requirement for an on-site cyclotron, the inability to acquire anatomical and functional information in the brain during the same examination and the high prevalence of positive amyloid scans in asymptomatic individuals, especially in the elderly which hampers the use of this method as a diagnostic tool in the elderly (9).

Earlier research demonstrated the potential of high-field (7T) magnetic resonance imaging (MRI) in the diagnosis of AD by showing distinct intensity changes in the cortex on T_2^* -weighted images of post mortem brain specimens of AD patients. These features included hypointense foci and diffuse granular patterns of less distinct hypointense foci in the cerebral cortex (10). Similar patterns have been described in studies of AD transgenic mice and post mortem human AD, and were attributed to the presence of amyloid plaques using histological confirmation (11–19). It has been proposed that the visualization on MRI of plaques in humans and mice is based on the fact that these deposits co-localize with iron, which gives rise to magnetic susceptibility effects on T_2^* -weighted images over volumes that are much larger than the actual size of amyloid plaques (17, 19–24). An alternative method to measure these susceptibility changes in the brain is to measure the relative phase in regions of interest, since it has been shown that this is a reliable indicator of the iron content in the brain (25–28). Although previous studies have demonstrated the potential of this approach in high-field MRI (29, 30), no clinical studies have been performed yet on AD patients in-vivo for the detection of AD pathology.

The overall aim of the present study is to confirm previous post mortem findings, by detecting AD pathology in the cerebral cortex and hippocampus, using a novel in vivo 7T high-field MR approach.

MATERIALS AND METHODS

Participants

This study was approved by the local institutional review board. In all cases, informed consent was obtained according to the declaration of Helsinki (31). In total 16 AD patients with a mean age of 76.9 years (range 68 to 86 years, 10 male/6 female) and 15 control subjects with a mean age of 75.1 years (range 69 to 80 years, 10 male/5 female) were included.

The AD patients were recruited from the memory clinic of the Leiden University Medical Center. Memory clinic patients were referred to the hospital by their general practitioner or a medical specialist. Prior to the 7T study these patients all underwent a routine clinical protocol, comprising a whole brain MRI (3 Tesla), a battery of neuropsychological tests, and a general medical and neurological examination performed by a neurologist, psychiatrist or internist-geriatrician. The diagnosis was made in a multidisciplinary consensus meeting using the NINCDS-ADRDA criteria for diagnosing probable Alzheimer's disease (32). Participants with the diagnosis 'probable AD', who were capable of giving informed consent (Mini Mental State Examination (MMSE) ≥ 19) with late onset dementia (age > 67 year) were selected for inclusion in the 7T study either retrospectively within one year after attending the memory clinic, or prospectively.

Healthy control subjects were recruited by focussed advertisement. Subjects with an age between 69-80 years, who were living independently, had an MMSE ≥ 25 and a Geriatric Depression Scale (GDS) ≤ 4 were selected for inclusion. Subjects with the following diseases were excluded; stroke, morbus Parkinson, dementia, diabetes mellitus, rheumatoid arthritis, polymyalgia rheumatica, cancer, heart failure, and chronic obstructive pulmonary disease.

Image acquisition

MRI was performed on a whole body human 7 T MR system (Philips Healthcare, Best, the Netherlands) using a quadrature transmit and 16-channel receive head coil (Nova Medical, Wilmington, MA, USA). Participants were scanned using a 2D flow-compensated transverse T_2^* -weighted gradient-echo scan which included the frontal and parietal regions for amyloid detec-

tion with a total imaging duration of 10 minutes. Imaging parameters were: repetition time (TR)/echo time (TE) 794/25 ms, flip angle 45°, slice thickness 1.0 mm with a 0.1 mm interslice gap, 20 slices, 240 x 180 x 22 mm field of view, 1000 x 1024 matrix size – resulting in an in-plane nominal spatial resolution of 0.24 x 0.24 mm². Figure 1 shows a typical positioning of these 20 slices. The bandwidth per pixel was 46 Hz, corresponding to a readout length of approximately 22 ms. The frequency and phase encoding directions were along the anterior-posterior and right-left axes, respectively. Additionally, a coronal 2D flow-compensated T₂^{*}-weighted gradient echo scan covering the hippocampus with a total imaging duration of 6 minutes was performed. Imaging parameters were: TR/TE 624/14 ms, flip angle of 40°, slice thickness of 3.0 mm with no interslice gap, 32 slices, 240 x 180 x 96 mm field of view, 480 x 480 matrix size - resulting in a nominal in-plane spatial resolution of 0.5 x 0.5 mm². These sequences are very sensitive to image artifacts arising from resonance frequency fluctuations within the brain caused by slight patient movements, even in areas significantly away from the head. A navigator echo was included to correct for these artifacts (33). Shimming up to third order was performed using an image based shimming approach (34). The phase images were subsequently unwrapped by highpass filtering with a 92x92 kernel size (35).

Image analysis

First, the T₂^{*}-weighted gradient-echo images were evaluated, blinded for diagnosis, for hypointense foci by SvR and checked by MvB as described in a previous ex-vivo study (10).

Image phase values in the cortex were determined using the transverse 2D T₂^{*}-weighted gradient echo scans. Based on the visual observation on unwrapped phase images of a higher contrast between gray and white matter in AD patients than in controls, due to a higher signal intensity within the gray matter, the phase values of the cortical gray matter were determined in regions of interest (ROIs) in four different areas of the brain: temporoparietal left, temporoparietal right, frontal and parietal. Because of the laminar variation in the cortical areas (29), histograms perpendicular to the cortex within these regions were created to measure peak gray matter phase values, over at least 10 cortical regions per slice and per region. To correct for local macroscopic magnetic field inhomogeneities subcortical white matter phase values were measured and used as an internal reference value. Phase values for gray and white matter were measured in these four areas per MRI slice for every other slice (ten in total), resulting in 40 phase values for gray and white matter separately per subject. Phase values of the different ROIs of the four

regions were averaged. Per subject, the overall phase shift between cortical gray and subcortical white matter (cortical phase shift) was calculated for each region and expressed in radians.

Phase values of the hippocampus were determined using the coronal 2D T_2^* -weighted gradient echo scans. The hippocampus was manually segmented and phase values were determined on 5 consecutive slices, starting at the head of the hippocampus, for the right and left hippocampus separately. For each subject, these five measurements were averaged for each hippocampus. Phase values of the white matter were determined in three neighboring areas of subcortical white matter on each of the five slices and averaged per subject. The phase shift of the hippocampus was calculated by the difference in phase value of the hippocampus and white matter (hippocampal phase shift) and expressed in radians. Analysis of the hippocampus was only performed in 12 of the 16 AD patients and in 14 of the 15 controls, because of severe motion artifacts that could not be completely corrected for (three subjects) or because participants were not able to finish the whole scan protocol (two subjects).

Statistics

A Mann-Whitney U-test was used to assess differences in age, gender, MMSE and phase measurements between AD and control groups. Logistic regression analysis was used to assess the association between diagnosis and inter-tissue phase shifts in the cortex and hippocampus, corrected for age and gender. To assess the interaction between cortical gray matter/hippocampal and white matter phase values, both were also entered as covariates in one model. Receiver operating characteristic (ROC) analysis was performed to determine the area under the ROC curve and to assess the optimal cut-off phase shift in the cortex and hippocampus to detect AD with its corresponding sensitivity, specificity, positive predictive value, and negative predictive value. To determine the association between MMSE and phase shift in the cortex and hippocampus, a linear regression analysis including a Pearson correlation corrected for age and gender was performed. All statistical analyses were performed with the Statistical Package of Social Sciences (SPSS, version 17.0.1; SPSS, Chicago, Ill).

RESULTS

The characteristics of the participants are shown in Table 1. No difference in age or gender was found between patient and control groups. Scores for global cognitive functioning (MMSE score) were significantly higher in controls

(29.0 points) than in patients with AD (22.5 points), $p < 0.001$.

	AD (n = 16)	Controls (n = 15)
Mean age, years (range)	76.9 (68–86)	75.1 (69–80)
Male/female	10/6	10/5
Median MMSE, points (range)	22.5 (19–26)	29.0 (27–30)

AD = Alzheimer's Disease, MMSE = Mini Mental State Examination.

Figure 2 shows representative transverse T_2^* -weighted magnitude and phase images of the parietal region of a subject with AD (a and b) and a control subject (c and d). Figure 3 shows coronal T_2^* -weighted magnitude and phase images of the hippocampus of a subject with AD (a and b) and a control subject (c and d). In none of the subjects were small focal hypointensities found in either the cortex or hippocampus.

	AD (rad) (n = 16)	Control (rad) (n = 15)	p-value
Temporoparietal left	0.90 ± 0.08	$0.79 + 0.08$	0.001
Temporoparietal right	$0.97 + 0.10$	$0.85 + 0.09$	0.001
Frontal	0.70 ± 0.08	0.62 ± 0.07	0.004
Parietal	0.87 ± 0.10	0.74 ± 0.08	0.000
Hippocampus right	0.09 ± 0.04	0.07 ± 0.03	0.18
Hippocampus left	0.10 ± 0.04	0.08 ± 0.02	0.14

AD = Alzheimer's Disease, rad = radians.

Table 2 shows the mean phase shifts of the temporoparietal, frontal, parietal cortex and the right and left hippocampus. For the temporoparietal, frontal, and parietal cortex, a larger cortical phase shift ($p < 0.005$) was found in the AD patients compared to control subjects (adjusted for age and gender). For both hippocampi no difference in phase shifts between groups was observed. Analysis in which both gray and white matter values were entered in the logistic regression model showed that only the cortical gray matter phase value, and not the white matter phase value, was associated with diagnosis. For the hippocampus, both gray and white matter phase values were not associated with diagnosis.

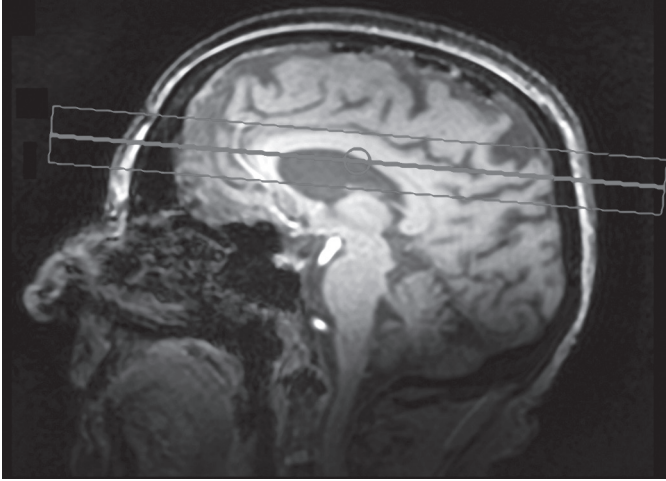


Figure 1: Sagittal survey image.

The stack position of the 2D T_2^* -weighted gradient-echo scan including the frontal and parietal regions for amyloid detection is shown. Image shows sagittal plane.

To determine the diagnostic value of the phase measurements in differentiating AD from control subjects, ROC analysis was performed for each region. Table 3 shows the area under the curve (AUC), cut-off value, sensitivity, specificity, positive and negative predictive values of all regions selected. For the temporoparietal, frontal, and parietal cortex an AUC between 0.79 and 0.85 was found, with the regions all having a high specificity (90-100%) and a moderate-to-high sensitivity (50-70%). Of these regions, the parietal cortex demonstrated the highest AUC (0.85) with a sensitivity of 69% and a specificity of 93%. The corresponding positive predictive value and negative predictive value were 92% and 74%. Both hippocampi demonstrated a lower AUC; right hippocampus 0.66 and left hippocampus 0.67. This resulted in a relatively lower specificity and positive predictive value. The sensitivity and negative predictive values were comparable with the regions in the cortex.

There was a significant negative correlation (adjusted for age and gender) between MMSE and phase shift in the left temporoparietal cortex, $r = -0.47$ ($\beta = -0.464$, $p < .05$), the right temporoparietal cortex, $r = -0.41$ ($\beta = -0.473$, $p < .05$), frontal cortex, $r = -0.44$ ($\beta = -0.404$, $p < .05$) and parietal cortex, $r = -0.54$ ($\beta = -0.501$, $p < .05$) (all: $P < 0.05$). For the right and the left hippocampus there was no correlation between MMSE and phase shift (right hippocampus, $r = -0.25$, $p = 0.21$ ($\beta = -0.168$, $p = .404$), left hippocampus, $r = -0.27$, $p = 0.19$ ($\beta = -0.190$, $p = .336$)).

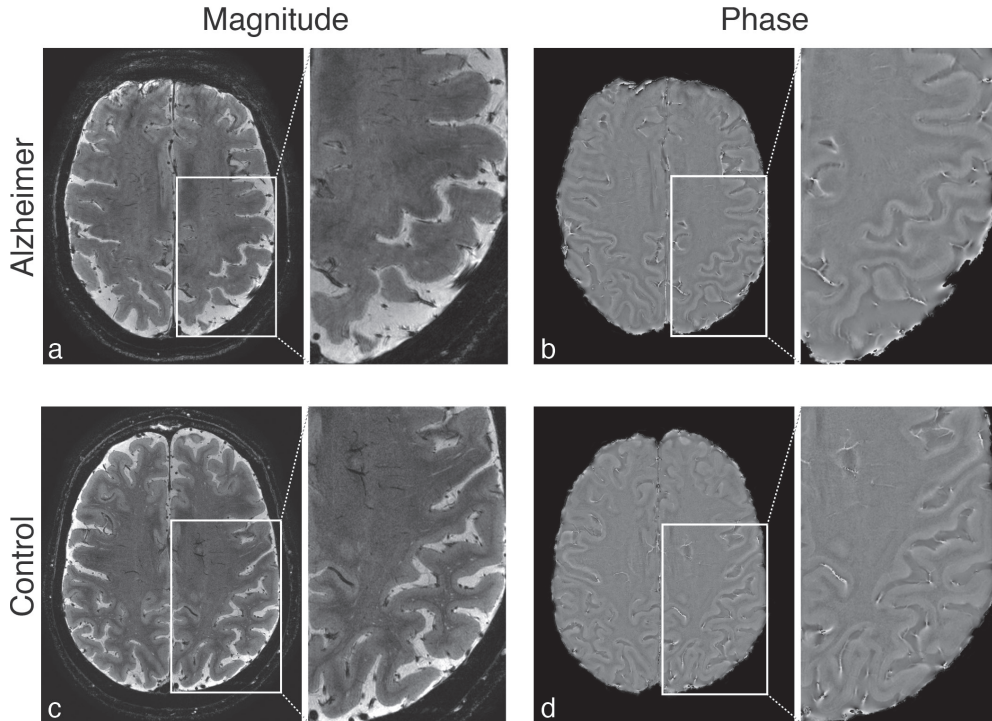


Figure 2: Cortex T_2^* -weighted images obtained in AD patient and control subject.

Representative $0.24 \times 0.24 \text{ mm}^2$ 2D T_2^* -weighted gradient echo images show an AD patient (A and B) and a control subject (C and D). Image A and C show magnitude images and image B and D phase images of the parietal region. No hypointense foci are seen on the magnitude images. The phase images show that the contrast between gray and white matter is enhanced in the AD patient in comparison to the control subject, indicating a larger cortical phase difference. Images show transverse planes.

DISCUSSION

This study shows that using a novel high-field imaging approach at 7T, patients with clinical symptoms of AD demonstrate an increased cortical phase shift on T_2^* -weighted images. These phase shifts between AD patients and control subjects have a high specificity, independent of age and gender. Moreover, these phase shifts correlated with individual MMSE scores. Of all cortical areas studied, the parietal cortex shows the highest specificity combined with the highest sensitivity for the diagnosis AD and the strongest correlation with MMSE. On the other hand, phase shifts in the hippocampus were not significantly increased in AD patients and did not correlate with MMSE.

High-field T_2^* -weighted MRI sequences are highly sensitive for iron depos-

its in the brain (36). In autopsy material of AD patients amyloid deposition and neurofibrillary tangles as well as tau deficiency were found to co-localize with neuronal iron accumulation (37–39). Therefore, it is likely that the increased cortical phase shift found on high-field T_2^* -weighted MRI in patients with AD indirectly reflect AD pathology. Our data also show that the particular distribution of the phase changes in the brain follows the known cerebral distribution of amyloid deposition in AD. In our data the neocortex, and more specifically the parietal lobes, allowed much better differentiating of AD patients from control subjects based on phase shift as compared to the hippocampus. In histological studies it was demonstrated that the neocortex is the first structure in the brain that is affected by amyloid depositions whereas the hippocampus is not only more mildly affected by amyloid plaques but also affected at a later stage of AD than the neocortex (40–42). This sequence of events has been confirmed by PiB-PET studies, showing high amyloid loads in the parietal and frontal lobes and not in hippocampus (5–7, 43, 44).

Phase measurement on T_2^* -weighted MRI at 7 Tesla has a high specificity for AD as compared to the reported specificity of the methods that are currently considered state of the art, such as cerebrospinal fluid (CSF) assay of the amyloid peptide or PiB PET imaging (9). Previous studies indicated that AD patients have reduced levels of A β 1-42 and increased levels of t-tau and p-tau181p in CSF compared to control subjects of which A β 1-42 is the most sensitive biomarker for AD of CSF samples. 7T MRI had lower sensitivity than these CSF analyses of A β 1-42 (69% vs. 96%) but had a higher specificity (93–100% vs. 77%) (45). PET studies using [11C] Pittsburgh Compound-B (PiB-PET) have shown the possibility of detecting cerebral amyloid accumulation, although the diagnostic utility is limited (46) and numbers on sensitivity and specificity are sparse. Mormino and coworkers (47) showed high sensitivity (90%) and specificity (90%) in differentiating AD patients from controls. However, within the group of healthy subjects the specificity drops with increasing age, because the percentage of positive PiB-PET scans increases rapidly with 12% of the people in their 60s, 30% in their 70s and 50% in their 80s giving “false positive” results (44, 48, 49). Our data show that measurement of phase shift using T_2^* -weighted MRI might improve the specificity of AD diagnosis.

Our study could not replicate the ex-vivo finding of hypointense foci, that might represent amyloid plaques (10). Although we corrected for resonance frequency variations, which are the main contributor to decreased image quality in AD patients, with a navigator echo (33) it is highly likely that even

sub-voxel degrees of motion blur the hypointense foci.

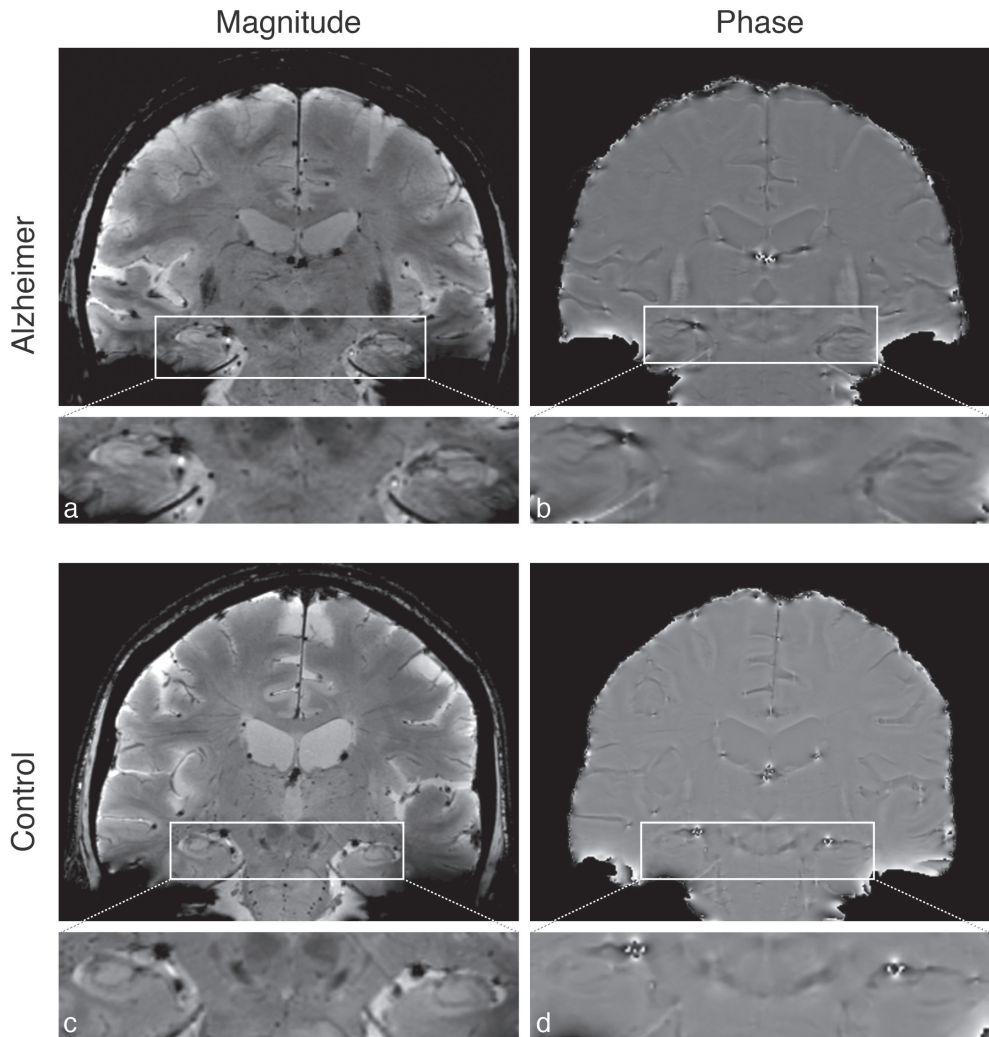


Figure 3: Hippocampus T_2^* -weighted images obtained in AD patient and control subject. Representative $0.5 \times 0.5 \text{ mm}^2$ $2D T_2^*$ -weighted gradient echo images show an AD patient (A and B) and a control subject (C and D). Image A and C show magnitude images and image B and D phase images of the hippocampal region. No hypointense foci are seen on the magnitude images. The phase images show no difference between the AD patient and the control subject in terms of image contrast between hippocampus and white matter.

Table 3: differentiating between AD patients and control subjects for the different regions.

	AUC	cut-off value (rad)	Sensitivity (%)	Specificity (%)	PPV+ (%)	NPV-(%)
Temporoparietal left	0.842	0.922	56 (9/16)	100 (15/15)	100 (9/9)	68 (15/22)
Temporoparietal right	0.823	0.985	50 (8/16)	100 (15/15)	100 (8/8)	65 (15/23)
Frontal	0.794	0.690	56 (9/16)	93 (14/15)	90 (9/10)	67 (14/21)
Parietal	0.854	0.817	69 (11/16)	93 (14/15)	92 (11/12)	74 (14/19)
Hippocampus right	0.655	0.074	75 (9/12)	71 (10/14)	69 (9/13)	77 (10/13)
Hippocampus left	0.673	0.095	58 (7/12)	86 (12/14)	78 (7/9)	71 (12/17)

AUC = area under the curve, PPV+ = positive predictive value, NPV- = negative predictive value.

A limitation of the present study is that phase measurements might also be influenced by the geometry and orientation of the scans (28). We limited these effects as much as possible by carefully positioning every participant in the same manner. Moreover, phase values were measured in the exact same way by using a standardized method. Furthermore, we averaged multiple measurements of phase values to cancel out the possible effects of geometry and orientation. A second limitation is that white matter phase values, which were used to correct for magnetic field inhomogeneities, might have an influence on the results. However, our data show that the observed phase changes were mainly caused by phase shifts in the gray matter. A third limitation is that we only included AD patients and healthy controls and therefore the diagnostic accuracy of our method in a group of memory clinic patients is unclear. The specificity of the presented method should be examined thoroughly by assessing different categories of neurodegenerative diseases to evaluate the ability to differentiate between different forms of dementia. Moreover, the value of our method should be investigated in the preclinical stages of AD in future studies to evaluate the possibility of detecting early AD pathology and to be used as an early treatment marker.

In conclusion, in this study we introduced a novel approach to detect cortical changes in AD patients exploiting the increased sensitivity of 7T MRI for iron in brain tissue. Our current data demonstrate that cortical phase changes are a potential new biomarker for AD.

ACKNOWLEDGEMENTS

This research was performed within the framework of CTMM, the Center for Translational Molecular Medicine (www.ctmm.nl), project LeARN (grant 02N-101) and was supported by NGI/NWO (05040202, 050-060-810) and HEALTH-2007-2.4.5-10.

REFERENCES

1. Nelson PT, Braak H, Markesbery WR. Neuropathology and cognitive impairment in Alzheimer disease: a complex but coherent relationship. *J. Neuropathol. Exp. Neurol.* 2009 ;68:1–14.
2. Johnson KA, Gregas M, Becker JA, Kinnecom C, Salat DH, Moran EK, Smith EE, Rosand J, Rentz DM, Klunk WE, Mathis CA, Price JC, Dekosky ST, Fischman AJ, Greenberg SM. Imaging of amyloid burden and distribution in cerebral amyloid angiopathy. *Ann. Neurol.* 2007 ;62:229–234.
3. Lockhart A, Lamb JR, Osredkar T, Sue LI, Joyce JN, Ye L, Libri V, Leppert D, Beach TG. PIB is a non-specific imaging marker of amyloid-beta (A β) peptide-related cerebral amyloidosis. *Brain* 2007 ;130:2607–2615.
4. Ikonomic MD, Klunk WE, Abrahamson EE, Mathis CA, Price JC, Tsopelas ND, Lopresti BJ, Ziolkowski S, Bi W, Paljug WR, Debnath ML, Hope CE, Isanski BA, Hamilton RL, DeKosky ST. Post-mortem correlates of in vivo PiB-PET amyloid imaging in a typical case of Alzheimer's disease. *Brain* 2008 ;131:1630–1645.
5. Klunk WE, Engler H, Nordberg A, Wang Y, Blomqvist G, Holt DP, Bergström M, Savitcheva I, Huang G-F, Estrada S, Ausén B, Debnath ML, Barletta J, Price JC, Sandell J, Lopresti BJ, Wall A, Koivisto P, Antoni G, Mathis CA, Långström B. Imaging brain amyloid in Alzheimer's disease with Pittsburgh Compound-B. *Annals of Neurology* 2004 ;55:306–319.
6. Engler H, Forsberg A, Almkvist O, Blomqvist G, Larsson E, Savitcheva I, Wall A, Ringheim A, Långström B, Nordberg A. Two-year follow-up of amyloid deposition in patients with Alzheimer's disease. *Brain* 2006 ;129:2856–2866.
7. Rowe CC, Ng S, Ackermann U, Gong SJ, Pike K, Savage G, Cowie TF, Dickinson KL, Maruff P, Darby D, Smith C, Woodward M, Merory J, Tochon-Danguy H, O'Keefe G, Klunk WE, Mathis CA, Price JC, Masters CL, Villemagne VL. Imaging beta-amyloid burden in aging and dementia. *Neurology* 2007 ;68:1718–1725.
8. Bacskai BJ, Frosch MP, Freeman SH, Raymond SB, Augustinack JC, Johnson KA, Irizarry MC, Klunk WE, Mathis CA, Dekosky ST, Greenberg SM, Hyman BT, Growdon JH. Molecular imaging with Pittsburgh Compound B confirmed at autopsy: a case report. *Arch. Neurol.* 2007 ;64:431–434.
9. Rowe CC, Villemagne VL. Brain amyloid imaging. *J. Nucl. Med.* 2011 ;52:1733–1740.
10. van Rooden S, Maat-Schieman MLC, Nabuurs RJA, van der Weerd L, van Duijn S, van Duinen SG, Natté R, van Buchem MA, van der Grond J. Cerebral amyloidosis: postmortem detection with human 7.0-T MR imaging system. *Radiology* 2009 ;253:788–796.
11. Benveniste H, Einstein G, Kim KR, Hulette C, Johnson GA. Detection of neuritic plaques in Alzheimer's disease by magnetic resonance microscopy. *Proc. Natl. Acad. Sci. U.S.A.* 1999 ;96:14079–14084.
12. Zhang J, Yarowsky P, Gordon MN, Di Carlo G, Munireddy S, van Zijl PCM, Mori S. Detection of amyloid plaques in mouse models of Alzheimer's disease by magnetic resonance imaging. *Magn Reson Med* 2004 ;51:452–457.
13. Helpert JA, Lee S-P, Falangola MF, Dyakin VV, Bogart A, Ardekani B, Duff K, Branch C, Wisniewski T, de Leon MJ, Wolf O, O'Shea J, Nixon RA. MRI assessment of neuropathology in a transgenic mouse model of Alzheimer's disease. *Magn Reson Med* 2004 ;51:794–798.

14. Lee S-P, Falangola MF, Nixon RA, Duff K, Helpert JA. Visualization of beta-amyloid plaques in a transgenic mouse model of Alzheimer's disease using MR microscopy without contrast reagents. *Magn Reson Med* 2004 ;52:538–544.
15. Jack CR Jr, Garwood M, Wengenack TM, Borowski B, Curran GL, Lin J, Adriany G, Gröhn OHJ, Grimm R, Poduslo JF. In vivo visualization of Alzheimer's amyloid plaques by magnetic resonance imaging in transgenic mice without a contrast agent. *Magn Reson Med* 2004 ;52:1263–1271.
16. Braakman N, Matysik J, van Duinen SG, Verbeek F, Schliebs R, de Groot HJM, Alia A. Longitudinal assessment of Alzheimer's beta-amyloid plaque development in transgenic mice monitored by in vivo magnetic resonance microimaging. *J Magn Reson Imaging* 2006 ;24:530–536.
17. Vanhoutte G, Dewachter I, Borghgraef P, Van Leuven F, Van der Linden A. Noninvasive in vivo MRI detection of neuritic plaques associated with iron in APP[V717I] transgenic mice, a model for Alzheimer's disease. *Magn Reson Med* 2005 ;53:607–613.
18. Nakada T, Matsuzawa H, Igarashi H, Fujii Y, Kwee IL. In vivo visualization of senile-plaque-like pathology in Alzheimer's disease patients by MR microscopy on a 7T system. *J Neuroimaging* 2008 ;18:125–129.
19. Meadowcroft MD, Connor JR, Smith MB, Yang QX. MRI and histological analysis of beta-amyloid plaques in both human Alzheimer's disease and APP/PS1 transgenic mice. *J Magn Reson Imaging* 2009 ;29:997–1007.
20. Falangola MF, Lee S-P, Nixon RA, Duff K, Helpert JA. Histological co-localization of iron in A β plaques of PS/APP transgenic mice. *Neurochem. Res.* 2005 ;30:201–205.
21. Grundke-Iqbal I, Fleming J, Tung YC, Lassmann H, Iqbal K, Joshi JG. Ferritin is a component of the neuritic (senile) plaque in Alzheimer dementia. *Acta Neuropathol.* 1990 ;81:105–110.
22. El Tannir El Tayara N, Delatour B, Le Cudennec C, Guégan M, Volk A, Dhenain M. Age-related evolution of amyloid burden, iron load, and MR relaxation times in a transgenic mouse model of Alzheimer's disease. *Neurobiol. Dis.* 2006 ;22:199–208.
23. Exley C. Aluminium and iron, but neither copper nor zinc, are key to the precipitation of beta-sheets of A β_{42} in senile plaque cores in Alzheimer's disease. *J. Alzheimers Dis.* 2006 ;10:173–177.
24. Lovell MA, Robertson JD, Teesdale WJ, Campbell JL, Markesbery WR. Copper, iron and zinc in Alzheimer's disease senile plaques. *J. Neurol. Sci.* 1998 ;158:47–52.
25. Ogg RJ, Langston JW, Haacke EM, Steen RG, Taylor JS. The correlation between phase shifts in gradient-echo MR images and regional brain iron concentration. *Magn Reson Imaging* 1999 ;17:1141–1148.
26. Haacke EM, Cheng NYC, House MJ, Liu Q, Neelavalli J, Ogg RJ, Khan A, Ayaz M, Kirsch W, Obenaus A. Imaging iron stores in the brain using magnetic resonance imaging. *Magnetic Resonance Imaging* 2005 ;23:1–25.
27. Haacke EM, Ayaz M, Khan A, Manova ES, Krishnamurthy B, Gollapalli L, Ciulla C, Kim I, Petersen F, Kirsch W. Establishing a baseline phase behavior in magnetic resonance imaging to determine normal vs. abnormal iron content in the brain. *Journal of Magnetic Resonance Imaging: JMRI* 2007 ;26:256–64.
28. Yao B, Li T-Q, Gelderen P van, Shmueli K, de Zwart JA, Duyn JH. Susceptibility contrast in high field MRI of human brain as a function of tissue iron content. *Neuroimage* 2009 ;44:1259–1266.

29. Duyn JH, van Gelderen P, Li T-Q, de Zwart JA, Koretsky AP, Fukunaga M. High-field MRI of brain cortical substructure based on signal phase. *Proceedings of the National Academy of Sciences* 2007 ;104:11796–11801.
30. Fukunaga M, Li T-Q, van Gelderen P, de Zwart JA, Shmueli K, Yao B, Lee J, Maric D, Aronova MA, Zhang G, Leapman RD, Schenck JF, Merkle H, Duyn JH. Layer-specific variation of iron content in cerebral cortex as a source of MRI contrast. *Proceedings of the National Academy of Sciences* 2010 ;107:3834 –3839.
31. Lynöe N, Sandlund M, Dahlqvist G, Jacobsson L. Informed consent: study of quality of information given to participants in a clinical trial. *BMJ* 1991 ;303:610–613.
32. McKhann G, Drachman D, Folstein M, Katzman R, Price D, Stadlan EM. Clinical diagnosis of Alzheimer’s disease: report of the NINCDS-ADRDA Work Group under the auspices of Department of Health and Human Services Task Force on Alzheimer’s Disease. *Neurology* 1984 ;34:939–944.
33. Versluis MJ, Peeters JM, van Rooden S, van der Grond J, van Buchem MA, Webb AG, van Osch MJP. Origin and reduction of motion and f0 artifacts in high resolution T2*-weighted magnetic resonance imaging: Application in Alzheimer’s disease patients. *NeuroImage* 2010 ;51:1082–1088.
34. Schär M, Kozerke S, Fischer SE, Boesiger P. Cardiac SSFP imaging at 3 Tesla. *Magnetic Resonance in Medicine* 2004 ;51:799–806.
35. Haacke EM, Xu Y, Cheng Y-CN, Reichenbach JR. Susceptibility weighted imaging (SWI). *Magnetic Resonance in Medicine* 2004 ;52:612–618.
36. Duyn JH. The future of ultra-high field MRI and fMRI for study of the human brain. *Neuroimage* 2012 ;62:1241–1248.
37. Duce JA, Tsatsanis A, Cater MA, James SA, Robb E, Wikke K, Leong SL, Perez K, Johanssen T, Greenough MA, Cho H-H, Galatis D, Moir RD, Masters CL, McLean C, Tanzi RE, Cappai R, Barnham KJ, Ciccotosto GD, Rogers JT, Bush AI. Iron-export ferroxidase activity of β -amyloid precursor protein is inhibited by zinc in Alzheimer’s disease. *Cell* 2010 ;142:857–867.
38. Lei P, Ayton S, Finkelstein DI, Spoerri L, Ciccotosto GD, Wright DK, Wong BXW, Adlard PA, Cherny RA, Lam LQ, Roberts BR, Volitakis I, Egan GF, McLean CA, Cappai R, Duce JA, Bush AI. Tau deficiency induces parkinsonism with dementia by impairing APP-mediated iron export. *Nat. Med.* 2012 ;18:291–295.
39. Smith MA, Harris PL, Sayre LM, Perry G. Iron accumulation in Alzheimer disease is a source of redox-generated free radicals. *Proc. Natl. Acad. Sci. U.S.A.* 1997 ;94:9866–9868.
40. Braak H, Braak E. Neuropathological staging of Alzheimer-related changes. *Acta Neuropathol.* 1991 ;82:239–259.
41. Arnold SE, Hyman BT, Flory J, Damasio AR, Van Hoesen GW. The topographical and neuroanatomical distribution of neurofibrillary tangles and neuritic plaques in the cerebral cortex of patients with Alzheimer’s disease. *Cereb. Cortex* 1991 ;1:103–116.
42. Thal DR, Rüb U, Orantes M, Braak H. Phases of A beta-deposition in the human brain and its relevance for the development of AD. *Neurology* 2002 ;58:1791–1800.
43. Ng SY, Villemagne VL, Masters CL, Rowe CC. Evaluating atypical dementia syndromes using positron emission tomography with carbon 11 labeled Pittsburgh Compound B. *Arch. Neurol.* 2007 ;64:1140–1144.

44. Mintun MA, LaRossa GN, Sheline YI, Dence CS, Lee SY, Mach RH, Klunk WE, Mathis CA, DeKosky ST, Morris JC. [11C]PIB in a Nondemented Population Potential Antecedent Marker of Alzheimer Disease. *Neurology* 2006 ;67:446–452.
45. Shaw LM, Vanderstichele H, Knapik-Czajka M, Clark CM, Aisen PS, Petersen RC, Blennow K, Soares H, Simon A, Lewczuk P, Dean R, Siemers E, Potter W, Lee VM-Y, Trojanowski JQ. Cerebrospinal fluid biomarker signature in Alzheimer’s disease neuroimaging initiative subjects. *Ann. Neurol.* 2009 ;65:403–413.
46. Quigley H, Colloby SJ, O’Brien JT. PET imaging of brain amyloid in dementia: a review. *Int J Geriatr Psychiatry* 2011 ;26:991–999.
47. Mormino EC, Kluth JT, Madison CM, Rabinovici GD, Baker SL, Miller BL, Koeppe RA, Mathis CA, Weiner MW, Jagust WJ. Episodic memory loss is related to hippocampal-mediated beta-amyloid deposition in elderly subjects. *Brain* 2009 ;132:1310–1323.
48. Rowe CC, Ellis KA, Rimajova M, Bourgeat P, Pike KE, Jones G, Frripp J, Tochon-Danguy H, Morandea L, O’Keefe G, Price R, Raniga P, Robins P, Acosta O, Lenzo N, Szoeka C, Salvado O, Head R, Martins R, Masters CL, Ames D, Villemagne VL. Amyloid imaging results from the Australian Imaging, Biomarkers and Lifestyle (AIBL) study of aging. *Neurobiol. Aging* 2010 ;31:1275–1283.
49. Villemagne VL, Pike KE, Chételat G, Ellis KA, Mulligan RS, Bourgeat P, Ackermann U, Jones G, Szoeka C, Salvado O, Martins R, O’Keefe G, Mathis CA, Klunk WE, Ames D, Masters CL, Rowe CC. Longitudinal assessment of A β and cognition in aging and Alzheimer disease. *Ann. Neurol.* 2011 ;69:181–192.

9

High-field imaging of neurodegenerative diseases

*M.J. Versluis
J. van der Grond
M.A. van Buchem
P. van Zijl
A.G. Webb*

ABSTRACT

High field magnetic resonance imaging is showing potential for imaging of neurodegenerative diseases. 7 T MRI is beginning to be used in a clinical research setting and the theoretical benefits, i.e. higher signal-to-noise, sensitivity to iron, improved MRA and increased spectral resolution in spectroscopy are being confirmed. Despite the limited number of studies to date, initial results in patients with multiple sclerosis, Alzheimer's disease and Huntington's disease show promising additional features in contrast that may assist in better diagnosis of these disorders.

INTRODUCTION

The increase in static magnetic field strength (B_0) for clinical MRI scanners has resulted in significant improvements in image quality. There is almost universal improvement in the diagnostic value of 3 T vs. 1.5 T clinical neurological MRI scans and 3 T scanners are routinely used for a broad range of applications. The need for increased sensitivity to early indicators of neurodegeneration with the goal of identifying potential biomarkers for diagnosis and the monitoring of treatment is one of the driving forces behind the interest in increasing further the magnetic field strength. The well-characterized signal-to-noise ratio (SNR) increase with field strength can be used for reduced acquisition times or higher spatial resolution. The increased sensitivity of image contrast (particularly in T_2^* -weighted sequences) to tissue iron levels has great potential for detecting early diffuse depositions that may lead to neurotoxic effects. The longer T_1 value of both blood and tissue results in higher quality MR angiography (MRA) with improved background suppression. Furthermore, the increased chemical shift difference between the proton signals of different metabolites has an advantage for magnetic resonance spectroscopy (MRS) in quantifying more metabolites than previously possible (1, 2).

Initial imaging studies of multiple sclerosis (MS) patients at 7 T appear promising in detecting more lesions with higher structural detail (3–5), especially in gray matter. In addition to the improved spatial resolution and signal-to-noise, the increased contrast in MR angiography (6) and cortical layer contrast in T_2^* -weighted imaging (7) have already demonstrated the potential of 7 T MRI. However, many intrinsic challenges remain to obtaining high quality MR data at field strengths of 7 T and above.

Challenges

The main challenges are related to creating a homogeneous magnetic field (B_0) and radiofrequency (RF) field B_1 over the entire brain. A higher magnetic field strength results in increased sensitivity to magnetic susceptibility induced field variations. On a microscopic scale this effect enhances the contrast within cortical layers (7, 8), basal ganglia (9), small venous structures (10–12) and results in greater white matter heterogeneity (13). However large-scale magnetic field variations induced by e.g. air-tissue interfaces (static) or respiration (dynamic) can lead to undesired signal loss and image deformations. Most modern high field MRI scanners are equipped with higher order shim gradients to improve the static field homogeneity. Careful optimization of sequence parameters and image correction algorithms has shown that it is

possible to acquire high quality images even from sequences such as echo planar imaging, which are particularly susceptible to static magnetic field inhomogeneities. Equally problematic, the amplitude of dynamically fluctuating magnetic fields caused by respiration or body movements also increases with field strength. It has been shown that corrections for these dynamic effects are possible both prospectively and retrospectively. Using dedicated hardware or sequences (14–16) image quality can be restored reasonably well.

Another fundamental challenge at 7 T is producing a highly homogeneous RF field, B_1 , with high efficiency in order to minimize tissue heating. B_1 inhomogeneities are due primarily to the dielectric properties of tissue, which result in partial constructive and destructive interactions from RF wave behavior (17). Tissue conductivity produces conduction currents in tissue, which dampens the electromagnetic (EM) field as it penetrates through tissue, producing a phase shift in the travelling RF. This not only results in significant image inhomogeneity and areas of signal loss but may also give rise to local heating, expressed as the specific absorption rate (SAR) from interaction with the electric field. The dielectric properties of tissue produce displacement currents in tissue, as well as inductive losses caused by eddy currents, and also alter the RF wavelength in tissue. The effective wavelength of electromagnetic energy in tissue is ~ 13 cm at 7 T. The brain has dimensions on the same order as the wavelength. This limits the applicability of conventional volume coils, such as the birdcage (18) and transverse electromagnetic (TEM) resonator (19), which produce homogeneous transmit fields at 1.5 T and 3 T, but cannot produce the same homogeneous fields at 7 T (17). The inhomogeneous RF field in combination with increased tissue heating leads to important sequence considerations. SAR intensive protocols involving sequences such as fast spin echo and fluid attenuated inversion recovery (FLAIR) cannot simply be copied from lower field strengths. Solutions will be discussed in the section “Future prospects and challenges”.

Despite these challenges 7 T MRI is beginning to be used in a clinical setting and the theoretical benefits of 7 T, i.e. higher signal-to-noise, sensitivity to iron, improved MRA and spectroscopy are being confirmed. Although, so far only a limited number of patient studies have been performed at 7 T and many of the proposed techniques still need further validation. Initial imaging studies of multiple sclerosis (MS) patients at 7 T appear promising in detecting more lesions with higher structural detail (3–5), especially in gray matter. In addition to the improved spatial resolution and signal-to-noise, the increased contrast in MR angiography (6) and the detection of cortical

layer contrast in T_2^* -weighted imaging (7) have already demonstrated the potential of 7 T MRI.

NEURODEGENERATIVE DISEASES

This section describes some of the clinical studies with 7 T MRI that have performed so far in patients suffering from neurodegenerative diseases.

CADASIL

Cerebral autosomal dominant arteriopathy with subcortical infarcts and leukoencephalopathy (CADASIL) is a hereditary form of small vessel disease that is caused by a mutation in the Notch3 gene. Pathologically, degeneration of the small smooth vessels is observed together with fibrous thickening of the small vessels. Clinical characteristics of the disease comprise cognitive loss, migrainous headaches, stroke-like episodes and dementia. In addition, cerebral blood flow is known to be reduced in CADASIL patients. However, the exact mechanism remains unclear and most findings regarding vessel wall pathology come from *ex vivo* studies. *In vivo* MRA can potentially provide valuable information on the hemodynamic changes in CADASIL patients. The most affected vessels are the leptomeningeal arteries supplying the white matter and the lenticulostriate perforating arteries supplying the deep gray nuclei. At lower field strengths MRA has been unable to visualize these arteries because of its small diameter. However, recent studies performed at 7 T show sufficient enhancements in resolution and contrast enabling visualization of the lenticulostriate arteries (6, 20, 21). The method that is most suited is time-of-flight (TOF) MRA, where the contrast is generated by the fresh inflow of blood with a gradient echo sequence that is relatively SAR friendly. The prolonged T_1 relaxation times at 7 T result in improved background saturation compared to lower field strengths, increasing the contrast between the vessel lumen and surrounding tissue. In addition the increase in SNR can be traded for a very high spatial resolution. In a recent study this was confirmed by visualization of significant lengths of the lenticulostriate arteries (22) in patients with CADASIL and control subjects. Figure 1 shows an example of a coronal maximum intensity projection of the lenticulostriate arteries in a healthy control subject and in a patient with CADASIL. The arrows point towards the lenticulostriate arteries. A small field of view (FOV) 3D TOF MRA technique was used with an isotropic resolution of 0.23 mm and 161 slices, resulting in a scan duration of 11 minutes. From these datasets, the number of visible arteries at different locations with respect to the middle and anterior cerebral artery, the cross-sectional area and length of the arteries were determined. No significant differences were found bet-

ween patients and controls in any of the measures. In addition no association was found between the luminal diameters and lacunar infarct load in the basal ganglia and basal ganglia hypointensities on separately acquired T_2^- , T_2^* - or T_1^- -weighted scans (22). These results suggest that basal ganglia damage in CADASIL is likely not caused by vascular mechanisms. The lack of association between age and disease duration with these vascular measurements further supports the finding that generalized narrowing of luminal diameters of lenticulostriate arteries does not play a significant role in the pathophysiology of CADASIL.

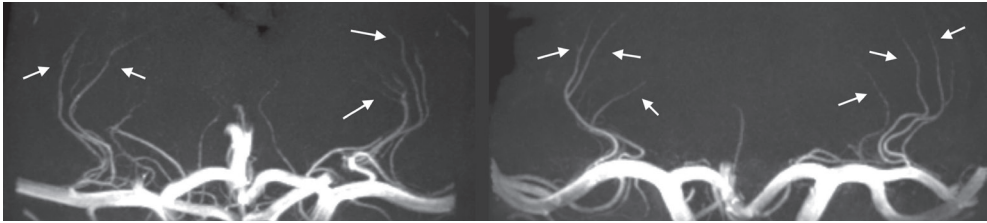


Figure 1: MRA of lenticulostriate arteries.

Coronal maximum intensity projections of a 32 year old healthy control (left) and 32 year old patient with CADASIL (right). The arrows point towards the lenticulostriate arteries. Excellent visualization of large portions of the lenticulostriate arteries was possible due to the high spatial resolution and contrast between the artery and surrounding tissue. No significant differences in length, diameter and number of lenticulostriate arteries was found, suggesting that basal ganglia damage in patients with CADASIL is not due to luminal narrowing of these vessels.

Another common MRI finding in patients with CADASIL are hypointensities on T_2^* -weighted images (22, 23) caused by iron containing hemosiderin deposits in cerebral microbleeds (CMBs). Figure 2 show CMBs observed bilaterally in the thalamus of a 35 year old patient with CADASIL on a T_2^* - and T_1^- -weighted image. Initial results have shown diffuse areas of T_2^* hypointensity in the basal ganglia, most commonly caused by diffuse iron deposition in CADASIL (24). Such diffuse areas have been described in other neurodegenerative diseases such as Alzheimer's disease (AD) as well. Still, it is unsure whether iron deposition is exclusively a neurodegenerative process, or if it can also be caused by vascular mechanisms. High field T_2^* -weighted MRI is extremely sensitive to changes in the local magnetic field, such as those generated by iron-rich regions. These changes in local magnetic field lead to decreased signal intensity on magnitude images and an increased frequency shift (relative to non-iron containing brain tissue) on phase images. Preliminary data of high resolution T_2^* -weighted images using a 2D gradient echo sequence obtained with a resolution of $0.24 \times 0.24 \times 1 \text{ mm}^3$ (24), demonstrated increased iron deposition in the globus pallidus and the caudate nucleus.

These findings were based on both magnitude images and unwrapped phase images. Both approaches gave similar results but the phase shift measurements showed larger differences, emphasizing the sensitivity of phase to iron induced changes in the brain.

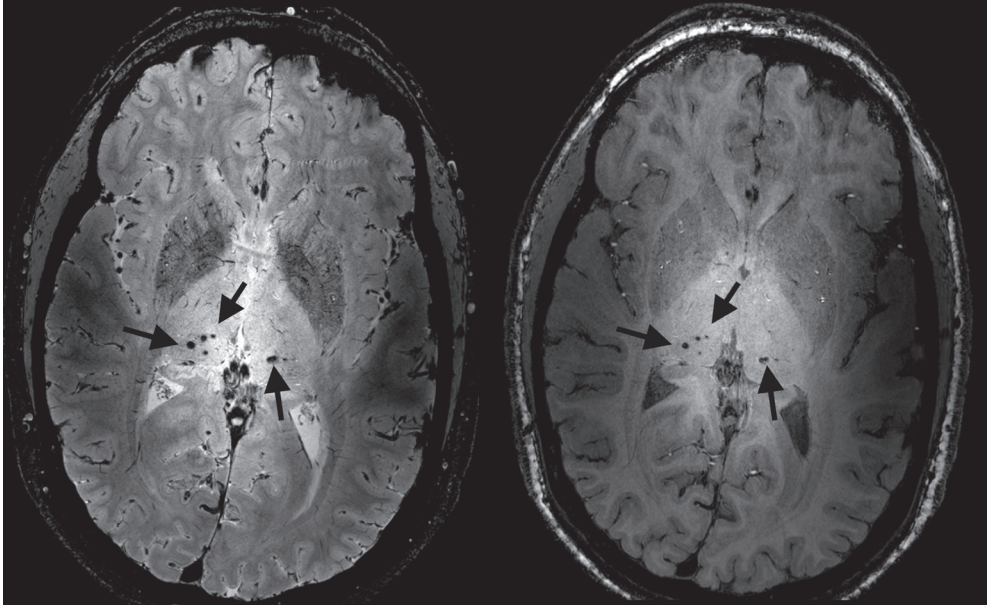


Figure 2: Microbleed detection in CADASIL.

Cerebral microbleeds (CMB) observed bilaterally in the thalamus of a 35 year old patient with CADASIL, visualized on a T_2^* -weighted (left) and T_1 -weighted (right) scan. The arrows point to the CMB. Accurate visualization of CMB is possible at high magnetic field strengths due to the induced susceptibility effect of haemosiderin deposits in the microbleeds. The sensitivity to detect CMB is highest on T_2^* -weighted scans.

In summary, high field MRI can provide useful additional information in understanding CADASIL pathology given the high resolution TOF images, sensitivity to CMBs (25) and diffuse iron deposition.

Huntington's Disease

Huntington's disease (HD) is a neurodegenerative autosomal dominant disorder caused by a gene mutation on the short arm of chromosome 4. A repeat expansion of the cytosine-adenine-guanine gene leads to an abnormally increased synthesis of huntingtin, a protein causing neuronal damage and brain atrophy. Ultimately, the disease leads to functional disturbances of motor function, cognition and behavior. Brain atrophy measurements, particularly of the striatum, are considered the MRI hallmark of the disease, showing changes up to a decade before clinical manifestations of the disease oc-

cur. The exact disease mechanism underlying these volume changes remains unclear. Several proposed theories include impaired energy metabolism and the degeneration of neurons due to neuronal overstimulation (excitotoxicity). MRS offers additional insight into which processes may play a role in these volume changes, by measuring, for example, N-acetylaspartate (NAA), creatine and glutamate concentrations. If the neuronal integrity were to be compromised, NAA would be expected to be reduced. Changes in energy deposition may be reflected in total creatine signals. In contrast, an increase in glutamate levels would reflect overstimulation of neurons. Lower field MRS studies have shown conflicting results, especially for findings in glutamate concentrations (26). Higher field provides improved spectral resolution allowing more metabolites to be quantified (1, 2). This can be done with better spatial localization (smaller volumes) due to increased SNR. In a study by Van den Bogaard et al. (26) localized MRS was performed using a stimulated echo acquisition mode (STEAM) sequence in the caudate nucleus, putamen, thalamus, hypothalamus and frontal lobe in patients with manifest and pre-manifest HD. Using 7 T MRS six metabolites could be identified in all of these nuclei: choline, creatine, glutamine + glutamate, total NAA, myo-inositol and lactate, despite the significant brain atrophy, which lead to reduced SNR. Figure 3 shows MR spectra in the caudate nucleus and putamen of control subjects and manifest patients. Lower concentrations of creatine and NAA were found in the caudate nucleus and the putamen, and a reduction of glutamate in the putamen, of manifests HD patients. Secondly an association between disease severity and metabolic levels of NAA, creatine and glutamate was demonstrated. The results from this study indicate affected energy metabolism in HD patients reflected in lower creatine concentrations, and a decrease in neuronal integrity reflected in lower NAA concentrations. In contrast to other studies a lower concentration of glutamate was found in the putamen of manifest patients. This study showed that 7 T allows measurement of reliable glutamate concentrations, thereby obtaining additional insight in the disease process.

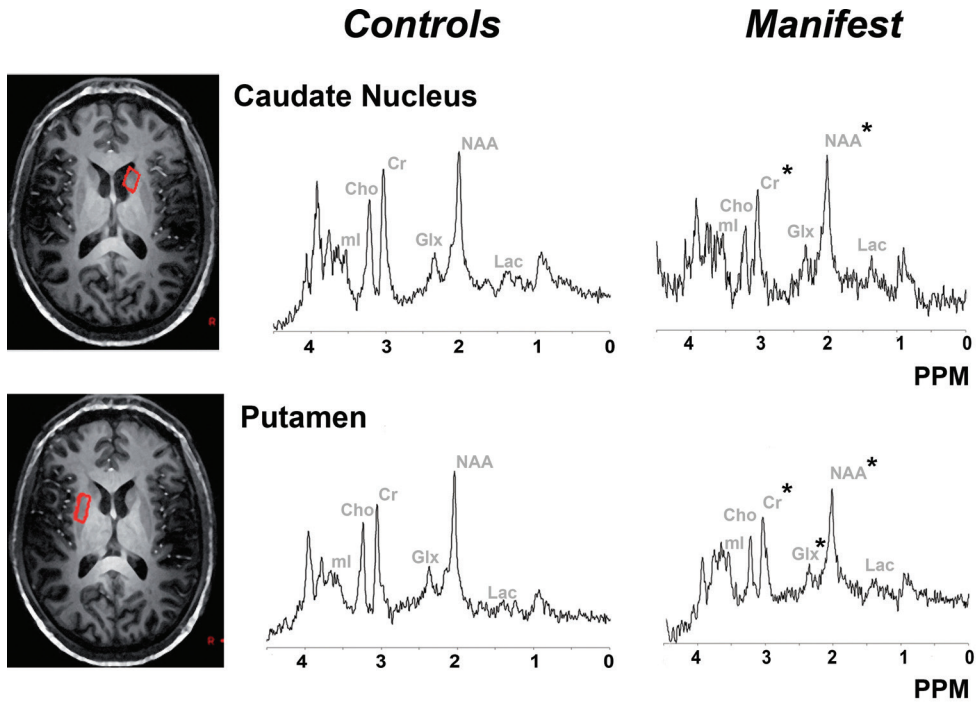


Figure 3: Representative MR spectra from the caudate nucleus and putamen in a control subject and manifest HD patient.

In total six metabolites could be identified in the hypothalamus, thalamus, caudate nucleus, putamen and the prefrontal region. In the caudate nucleus and putamen a significant decrease in NAA and creatine levels was found in manifest HD patients. Glutamate levels were found to decrease significantly in the putamen. Significance changes are depicted by asterisks (*), $p < 0.05$. **Cho** choline, **Cr** creatine, **NAA** N-acetylaspartate, **ml** myo-inositol, **Glx** glutamate + glutamine, **Lac** lactate, **PPM** parts per million.

In summary, the increased spectral and spatial resolution of 7 T MRS offer capabilities that are not possible at lower field strengths. It allows for the examination of metabolites in small anatomical structures in clinically acceptable scanning times, e.g. such as the caudate nucleus and putamen, which are important in many neurodegenerative diseases.

Multiple sclerosis

The field of MS research has been the most active since the introduction of 7 T MRI scanners. MS manifests itself through demyelinating lesions that can be detected by MRI. Conventional protocols use fluid attenuated inversion recovery (FLAIR) and dual inversion recovery (DIR) sequences to suppress signal from cerebrospinal fluid (CSF) or from both CSF and white matter, respectively, to highlight white matter (WM) lesions. In addition, gadolinium contrast agents can be administered to distinguish active lesions from older

lesions on T_1 -weighted images. Histology has revealed that lesions not only occur in WM but also frequently affect gray matter (GM) and that MS lesions have a preference for a perivenular location. The high spatial resolution and sensitivity of high field facilitates the detection of GM lesions and the perivenous location of lesions, which is more difficult at lower field strengths.

To make effective use of the high contrast generated by venous blood and to circumvent the difficulties implementing B_1 -sensitive and SAR-intensive sequences such as FLAIR and DIR, many studies have focused on T_2^* -weighted sequences. Using this type of contrast it was found that between 50% and 87% of lesions contain a central vein (4, 5, 27–29). Compared to lower field strengths, a significantly lower number of lesions containing a central vein was found. At 1.5 T no central venous structure was observed in any of the detected lesions (4), whereas twice as many lesions with a central vein were detected at 7 T compared to 3 T (5). Figure 4 shows a large WM lesion visualized using T_2^* -weighted MRI, comparing 7 T and 3 T (5). It is immediately apparent that the contrast within the lesion is enhanced at 7 T and that the perivenous location of the lesion can be appreciated.

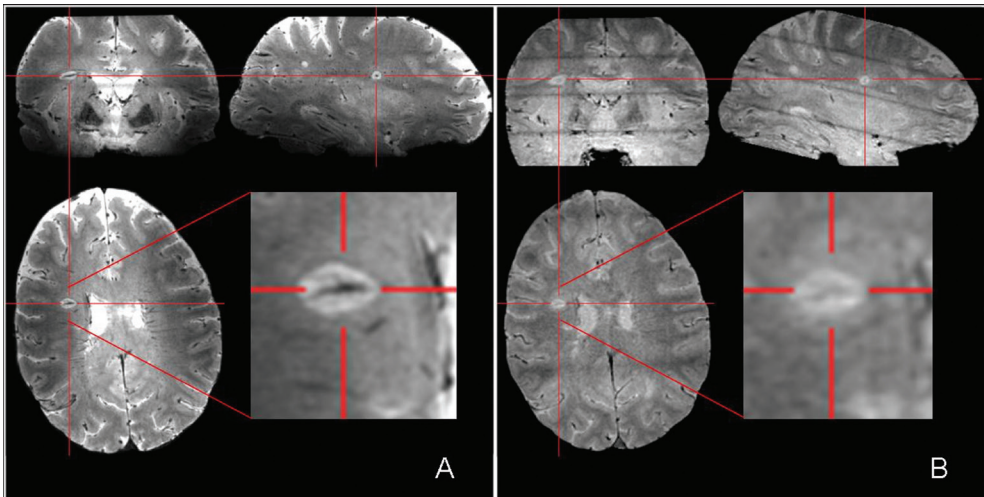


Figure 4: 7T T_2^* -weighted MRI shows more detail of central veins in MS lesions than 3T. T_2^* images of a patient with MS showing a large lesion with a perivenous orientation. On the 7T image (A) the vein can be seen in more detail than on the equivalent 3T image (B). Image courtesy of Dr. Emma Tallantyre.

The presence of a central vein in WM lesions may be an imaging characteristic that helps differentiating MS-related lesions from other WM lesions. This may be important for designing therapies targeted at MS lesions and monitoring disease progression, and also it may help providing insight into the mechanisms of lesion formation (27). It was found that the presence of

a central vessel is highly indicative of MS specific lesions. In a comparison between MS patients and subjects having WM lesions that were non-specific to MS, 80% of MS lesions had a perivenous location compared to only 19% in WM lesions not related to MS (29). The high sensitivity of 7 T in detecting perivascular signal changes is due to the susceptibility effect of venous blood. The effect of induced local magnetic field changes scales linearly with the applied magnetic field strength. Therefore the use of a sensitive method such as a T_2^* -weighted sequence at high field greatly improves the contrast generated by venous blood.

Apart from WM lesions, GM lesions are also a frequent finding in MS. GM MS lesions, however, can be very difficult to detect at lower field strengths. The increased spatial resolution at 7 T increases the number of visible GM lesions. Figure 5 shows an example of an MS patient with a cortical GM lesion (30). The arrow in the zoomed in section points towards the cortical GM lesion. In one study no GM lesions could be detected in patients at 1.5T, while 44% of the lesions detected at 7T showed cortical involvement (4). This was confirmed by other studies at 7 T (30, 31). In line with other neurodegenerative diseases higher iron deposition is expected in patients with MS. The high sensitivity to iron of 7 T has led to the investigation of MS lesions using phase images (3, 31, 32). However initial studies find that phase images have a lower sensitivity in detecting MS lesions (31) than the magnitude images. However between 8% and 21% of WM lesions show a characteristic ring around the lesion that is not readily visible on magnitude images (3, 31). This is thought to occur due to iron-rich macrophages and as such may provide information about the extent of inflammation around the MS lesion (4, 31).

T_2^* -weighted sequences were identified as being the most sensitive in detecting lesions compared to other sequences (31) and lower field strength (4). Recently, progress has been made in reducing the SAR requirements of FLAIR and DIR sequences at 7 T while maintaining comparable or improved contrast and spatial resolution (33, 34). Preliminary results have shown the applicability in MS patients (35), although no systematic comparison of using high field FLAIR and DIR sequences has been published to date.

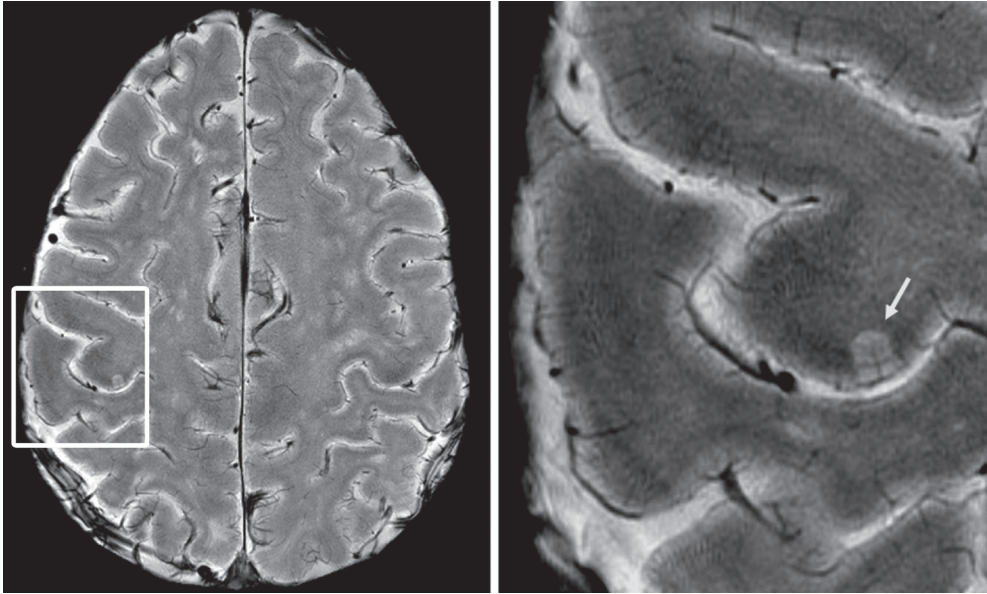


Figure 5: Axial T_2^* -weighted image (195x260 μm) of an MS patient with a cortical GM lesion at 7 T.

Right: Enlarged image of the region around the GM lesion demonstrating fine detail within the cortical lesion at this high magnetic field and fine spatial resolution. Image courtesy of Drs. Vigneron, Metcalf and Pelletier.

In summary, MS research at 7 T is promising. The difficulty in designing FLAIR and DIR sequences at 7 T has to date resulted in the use of T_2^* -weighted sequences to detect MS lesions. The high contrast and spatial resolution of this sequence provides an additional type of sequence to investigate MS lesions, especially suited for high magnetic field strengths.

Other neurodegenerative diseases

There have been a number of other clinical studies in the field of neurodegenerative diseases at 7 T. Most studies use the same contrast mechanisms as mentioned in the previous sections. In amyotrophic lateral sclerosis (ALS) patients 7 T MRI was used to investigate the presence of CMBs. In animal models of this disease deposits of hemosiderin and CMBs were found, in contrast no CMBs were found in sporadic ALS patients (36). In patients with Alzheimer's disease (AD) a limited number of studies has been published. One of the hallmarks of AD is the presence amyloid beta plaques, a protein thought to be associated with iron. The small size of these plaques (typically smaller than 150 μm) (37) makes direct in vivo visualization difficult, although not impossible. Using localized coils and a limited FOV a resolution of the same order of magnitude as individual plaques has been obtained in

a reasonable scan time (38). Susceptibility weighted imaging (SWI) post processing was performed to enhance the sensitivity to susceptibility changes (39), such as induced by iron. The results of this study suggest that plaques can be visualized using this technique. Still, it remains unclear whether the observed signal voids represent individual plaques or not. In addition to the presence of plaques, early in the process of the disease brain atrophy occurs. One of the first brain regions affected by AD is the hippocampus; however not all subsections of the hippocampus are affected in a similar way. These different subregions can be distinguished using high resolution T_2^* -weighted imaging sequences. One study has shown that in the very early stage of AD changes can be observed in the hippocampal subregion CA1 apical neuropil (40). From post mortem studies this region is known to be among the earliest affected in the brain. Interestingly at 7 T this was confirmed in vivo. Along the same line are findings in patients with hippocampal sclerosis (HS) where accurate visualization of subregions within the hippocampus is important for diagnosis. HS leads to atrophy of the intrahippocampal cortical fields CA1 to CA4 regions and to disruption of the internal hippocampal structure. In a study of focal epilepsy patients with HS, the intrahippocampal cortical fields could well be visualized on T_2^- and T_2^* -weighted sequences (41). Regional differences in hippocampal atrophy were shown between patients. In a different study similar findings were reported using T_1^- and T_2^- -weighted imaging. In all patients hippocampal abnormalities were observed. Using 7 T MRI localized atrophy in the Ammon horn was observed in temporal lobe epilepsy patients (42).

A small number of patients with Parkinson's disease (PD) has been studied at 7 T. The symptoms of PD can sometimes be reduced by deep brain stimulation. This is a neurosurgical technique that relies on the accurate placement of electrodes. Using high-resolution susceptibility weighted imaging (SWI) high contrast can be generated between the iron rich basal ganglia. It has been shown that high quality images can be obtained that help guiding the placement of these electrodes (43, 44).

FUTURE PROSPECTS AND CHALLENGES

In general, the theoretical gain in SNR and sensitivity of high field MR to, for example, diffuse iron accumulation have been shown to be achievable in practice. Transmit RF field inhomogeneity is still a major concern, but by using dedicated sequences that are less sensitive to these inhomogeneities some of these effects can be circumvented (45, 46). By placing high dielectric materials close to the brain the transmit field becomes more homogeneous

(2, 47). The coverage towards the cerebellum in particular is improved and the effect of high signal centrally in the brain is reduced. The ultimate “solution”, although currently only in the technical development phase, is the use of multiple transmit channels to improve the transmit homogeneity. Preliminary results already show the added value and one can anticipate that it will not take long before this technique is used in a clinical setting.

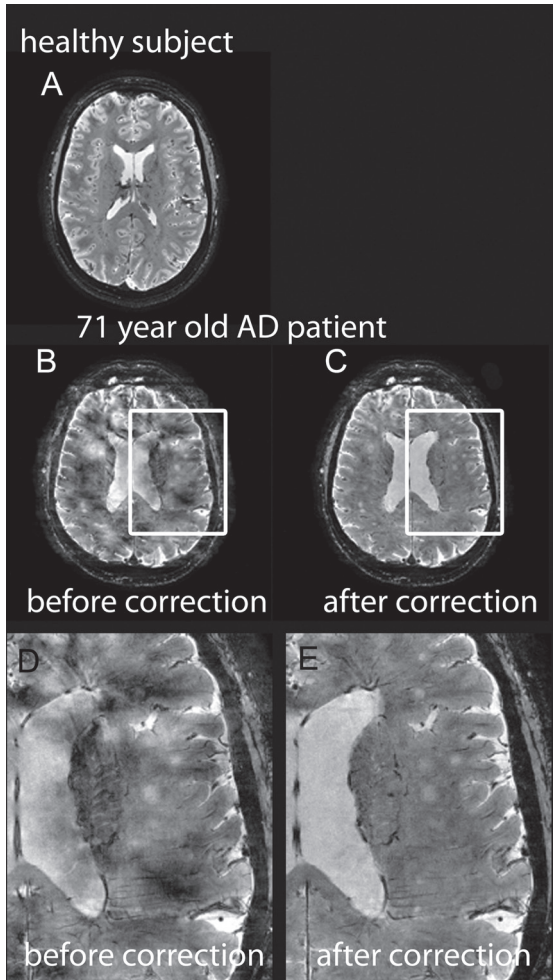


Figure 6: T_2^* -weighted images before and after correction

A healthy subject (a), showing the high image quality and contrast that can be obtained. Application of the same sequence in patients with AD leads to frequent image degradation (b and d) caused by fluctuating magnetic fields during image acquisition. Using a navigator echo correction technique it is possible to measure and correct for these dynamic fluctuations and improve image quality significantly (c and e). Correction techniques like these improve image quality at high field.

Sequence adaptations have not been trivial, the increased RF deposition and inhomogeneous transmit field preclude the simple translation from lower field strength protocols to 7 T. However, all conventional image contrasts (T_1 -, T_2 -, T_2^* -weighted and FLAIR) are currently available with high image quality. To limit the need for additional lower field strength scans, it is important to have these image contrasts available.

Magnetic susceptibility induced field changes scale linearly with the applied field strength. This leads to an increased sensitivity to iron accumulation in the brain (8, 9) and WM heterogeneity (13) detected in T_2^* -weighted sequences. An adverse effect is that the sensitivity to unwanted field changes is also increased. Air tissue interfaces at the edge of the brain or near the sinuses generate a static inhomogeneous magnetic field. Shim gradients up to third order are used to compensate for these changes. However the effects of dynamic susceptibility changes are also enhanced, leading to ghosting and image blurring. It has been shown that breathing (14, 48) and body movements (49) can lead to substantial magnetic field changes in the brain. In a study in AD patients image artifacts were observed that were related to dynamic magnetic field changes (15). Figure 6 shows a transverse slice from a T_2^* -weighted sequence in a healthy subject and an AD patient. The image quality is severely reduced in the AD patient. After navigator-based image correction for the effects of the magnetic field changes most image artifacts are suppressed. Still more advanced is to measure the field changes in real time using separate field probes that are positioned around the brain (16, 50), but this may not be clinically practical.

There has been rapid development of sequences and hardware since the introduction of 7 T MR systems. As a result most conventional sequences are available and high quality images are obtained in the brain. Based on the initial results so far, 7 T MRI is showing potential to be valuable in investigating neurodegenerative diseases. In patients with MS an increased number of lesions can be detected and more importantly, there is greater sensitivity to detect GM lesions. In addition to the increased sensitivity, also the pathophysiology of these lesions can be studied more extensively at high field. It was shown that most MS lesions have a clear vascular component. However, some lesions also showed up on phase images surrounded by a hypointense rim, possibly reflecting the area of inflammation or potentially a susceptibility effect. In patients with HD it was possible to quantify metabolite levels, including glutamate in very small regions of interest, providing valuable information about possible disease mechanisms. The sensitivity to iron and the high spatial resolution leads to a clearer depiction of the substantia nigra

and other deep gray matter nuclei in PD.

Even though limited clinical studies have been performed thus far, it is expected that the contribution of 7 T MRI especially in the field of neurodegenerative diseases will increase over time. Many of the initial problems related to magnetic and RF field inhomogeneities and the lack of optimized sequences have been solved or improved.

REFERENCES

1. Tkáč I, Oz G, Adriany G, Uğurbil K, Gruetter R. In vivo ^1H NMR spectroscopy of the human brain at high magnetic fields: metabolite quantification at 4T vs. 7T. *Magn Reson Med* 2009 ;62:868–879.
2. Mekle R, Mlynárik V, Gambarota G, Hergt M, Krueger G, Gruetter R. MR spectroscopy of the human brain with enhanced signal intensity at ultrashort echo times on a clinical platform at 3T and 7T. *Magn Reson Med* 2009 ;61:1279–1285.
3. Hammond KE, Metcalf M, Carvajal L, Okuda DT, Srinivasan R, Vigneron D, Nelson SJ, Pelletier D. Quantitative in vivo magnetic resonance imaging of multiple sclerosis at 7 Tesla with sensitivity to iron. *Ann. Neurol* 2008 ;64:707–713.
4. Kollia K, Maderwald S, Putzki N, Schlamann M, Theysohn JM, Kraff O, Ladd ME, Forsting M, Wanke I. First Clinical Study on Ultra-High-Field MR Imaging in Patients with Multiple Sclerosis: Comparison of 1.5T and 7T. *AJNR Am J Neuroradiol* 2009 ;30:699–702.
5. Tallantyre EC, Morgan PS, Dixon JE, Al-Radaideh A, Brookes MJ, Evangelou N, Morris PG. A comparison of 3T and 7T in the detection of small parenchymal veins within MS lesions. *Invest Radiol* 2009 ;44:491–494.
6. Kang C-K, Park C-W, Han J-Y, Kim S-H, Park C-A, Kim K-N, Hong S-M, Kim Y-B, Lee KH, Cho Z-H. Imaging and analysis of lenticulostriate arteries using 7.0-Tesla magnetic resonance angiography. *Magnetic Resonance in Medicine* 2009 ;61:136–144.
7. Duyn JH, van Gelderen P, Li T-Q, de Zwart JA, Koretsky AP, Fukunaga M. High-field MRI of brain cortical substructure based on signal phase. *Proc Natl Acad Sci U S A* 2007 ;104:11796–801.
8. Fukunaga M, Li T-Q, van Gelderen P, de Zwart JA, Shmueli K, Yao B, Lee J, Maric D, Aronova MA, Zhang G, Leapman RD, Schenck JF, Merkle H, Duyn JH. Layer-specific variation of iron content in cerebral cortex as a source of MRI contrast. *Proceedings of the National Academy of Sciences* 2010 ;107:3834 –3839.
9. Yao B, Li T-Q, Gelderen P van, Shmueli K, de Zwart JA, Duyn JH. Susceptibility contrast in high field MRI of human brain as a function of tissue iron content. *NeuroImage* 2009 ;44:1259–1266.
10. Conijn MMA, Geerlings MI, Luijten PR, Zwanenburg JJM, Visser F, Biessels GJ, Hendrikse J. Visualization of cerebral microbleeds with dual-echo T2*-weighted magnetic resonance imaging at 7.0 T. *J. Magn. Reson. Imaging* 2010 ;32:52–59.
11. Koopmans P, Manniesing R, Niessen W, Viergever M, Barth M. MR venography of the human brain using susceptibility weighted imaging at very high field strength. *Magnetic Resonance Materials in Physics, Biology and Medicine* 2008 ;21:149–158.
12. Theysohn JM, Kraff O, Maderwald S, Barth M, Ladd SC, Forsting M, Ladd ME, Gizewski ER. 7 tesla MRI of microbleeds and white matter lesions as seen in vascular dementia. *J. Magn. Reson. Imaging* 2011 ;33:782–791.
13. Li T-Q, van Gelderen P, Merkle H, Talagala L, Koretsky AP, Duyn J. Extensive heterogeneity in white matter intensity in high-resolution T2*-weighted MRI of the human brain at 7.0 T. *NeuroImage* 2006 ;32:1032–1040.
14. Van Gelderen P, de Zwart JA, Starewicz P, Hinks R, Duyn JH. Real-time shimming to compensate for respiration-induced B0 fluctuations. *Magnetic Resonance in Medicine* 2007 ;57:362–368.

15. Versluis MJ, Peeters JM, van Rooden S, van der Grond J, van Buchem MA, Webb AG, van Osch MJP. Origin and reduction of motion and f0 artifacts in high resolution T2*-weighted magnetic resonance imaging: Application in Alzheimer's disease patients. *NeuroImage* 2010 ;51:1082–1088.
16. Wilm BJ, Barmet C, Pavan M, Pruessmann KP. Higher order reconstruction for MRI in the presence of spatiotemporal field perturbations. *Magnetic Resonance in Medicine* 2011 ;65:1690–1701.
17. Webb AG, Collins CM. Parallel transmit and receive technology in high-field magnetic resonance neuroimaging. *Int. J. Imaging Syst. Technol.* 2010 ;20:2–13.
18. Hayes CE, Edelstein WA, Schenck JF, Mueller OM, Eash M. An efficient, highly homogeneous radiofrequency coil for whole-body NMR imaging at 1.5 T. *J Magn Reson* 1985 ;63:622–628.
19. Vaughan JT, Hetherington HP, Otu JO, Pan JW, Pohost GM. High frequency volume coils for clinical NMR imaging and spectroscopy. *Magn Reson Med* 1994 ;32:206–218.
20. Kang C-K, Park C-A, Kim K-N, Hong S-M, Park C-W, Kim Y-B, Cho Z-H. Non-invasive visualization of basilar artery perforators with 7T MR angiography. *J Magn Reson Imaging* 2010 ;32:544–550.
21. Zwanenburg JJM, Hendrikse J, Takahara T, Visser F, Luijten PR. MR angiography of the cerebral perforating arteries with magnetization prepared anatomical reference at 7T: Comparison with time-of-flight. *Journal of Magnetic Resonance Imaging* 2008 ;28:1519–1526.
22. Liem MK, van der Grond J, Versluis MJ, Haan J, Webb AG, Ferrari MD, van Buchem MA, Lesnik Oberstein SAJ. Lenticulostriate Arterial Lumina Are Normal in Cerebral Autosomal-Dominant Arteriopathy With Subcortical Infarcts and Leukoencephalopathy. *Stroke* 2010 ;41:2812–2816.
23. Jouvent E, Poupon C, Gray F, Paquet C, Mangin J-F, Le Bihan D, Chabriat H. Intracortical Infarcts in Small Vessel Disease. *Stroke* 2011 ;42:e27–e30.
24. Liem MKY, Oberstein SA., Versluis MJ, Haan J, Webb AG, Ferrari MD, van Buchem MA, van der Grond J. Diffuse iron deposition in the putamen and caudate nucleus in CADASIL: comparing phase and magnitude images at 7 Tesla. *Proceedings of the International Society of Magnetic Resonance in Medicine.* Montreal 2011 ;
25. Conijn MMA, Geerlings MI, Biessels G-J, Takahara T, Witkamp TD, Zwanenburg JJM, Luijten PR, Hendrikse J. Cerebral Microbleeds on MR Imaging: Comparison between 1.5 and 7T. *AJNR Am J Neuroradiol* 2011 ;32:1043–1049.
26. van den Bogaard SJA, Dumas EM, Teeuwisse WM, Kan HE, Webb A, Roos RAC, van der Grond J. Exploratory 7-Tesla magnetic resonance spectroscopy in Huntington's disease provides in vivo evidence for impaired energy metabolism [Internet]. *J Neurol* 2011 ;
27. Ge Y, Zohrabian VM, Grossman RI. Seven-Tesla Magnetic Resonance Imaging: New Vision of Microvascular Abnormalities in Multiple Sclerosis. *Arch Neurol* 2008 ;65:812–816.
28. Tallantyre EC, Brookes MJ, Dixon JE, Morgan PS, Evangelou N, Morris PG. Demonstrating the perivascular distribution of MS lesions in vivo with 7-Tesla MRI. *Neurology* 2008 ;70:2076–2078.
29. Tallantyre EC, Dixon JE, Donaldson I, Owens T, Morgan PS, Morris PG, Evangelou N. Ultra-high-field imaging distinguishes MS lesions from asymptomatic white matter lesions. *Neurology* 2011 ;76:534–539.

30. Metcalf M, Xu D, Okuda DT, Carvajal L, Srinivasan R, Kelley DAC, Mukherjee P, Nelson SJ, Vigneron DB, Pelletier D. High-Resolution Phased-Array MRI of the Human Brain at 7 Tesla: Initial Experience in Multiple Sclerosis Patients. *J Neuroimaging* 2010 ;20:141–147.
31. Mainero C, Benner T, Radding A, van der Kouwe A, Jensen R, Rosen BR, Kinkel RP. In vivo imaging of cortical pathology in multiple sclerosis using ultra-high field MRI. *Neurology* 2009 ;73:941–948.
32. Hammond KE, Lupo JM, Xu D, Metcalf M, Kelley DAC, Pelletier D, Chang SM, Mukherjee P, Vigneron DB, Nelson SJ. Development of a robust method for generating 7.0 T multichannel phase images of the brain with application to normal volunteers and patients with neurological diseases. *NeuroImage* 2008 ;39:1682–1692.
33. Zwanenburg J, Hendrikse J, Visser F, Takahara T, Luijten P. Fluid attenuated inversion recovery (FLAIR) MRI at 7.0 Tesla: comparison with 1.5 and 3.0 Tesla. *European Radiology* 2010 ;20:915–922.
34. Visser F, Zwanenburg JJM, Hoogduin JM, Luijten PR. High-resolution magnetization-prepared 3D-FLAIR imaging at 7.0 Tesla. *Magn Reson Med* 2010 ;64:194–202.
35. Visser F, Zwanenburg JJ, de Graaf WL, Castelijns JA, Luijten PR. 3D Magnetization Prepared Double Inversion Recovery (3D MP-DIR) at 7 Tesla. *Proceedings of the International Society of Magnetic Resonance in Medicine*. Montreal 2011 ;
36. Verstraete E, Biessels G-J, van Den Heuvel MP, Visser F, Luijten PR, van Den Berg LH. No evidence of microbleeds in ALS patients at 7 Tesla MRI. *Amyotroph Lateral Scler* 2010 ;11:555–557.
37. van Rooden S, Maat-Schieman MLC, Nabuurs RJA, van der Weerd L, van Duijn S, van Duinen SG, Natté R, van Buchem MA, van der Grond J. Cerebral Amyloidosis: Postmortem Detection with Human 7.0-T MR Imaging System. *Radiology* 2009 ;253:788–796.
38. Nakada T, Matsuzawa H, Igarashi H, Fujii Y, Kwee IL. In Vivo Visualization of Senile-Plaque-Like Pathology in Alzheimer's Disease Patients by MR Microscopy on a 7T System. *Journal of Neuroimaging* 2008 ;18:125–129.
39. Haacke EM, Xu Y, Cheng Y-CN, Reichenbach JR. Susceptibility weighted imaging (SWI). *Magnetic Resonance in Medicine* 2004 ;52:612–618.
40. Kerchner GA, Hess CP, Hammond-Rosenbluth KE, Xu D, Rabinovici GD, Kelley DAC, Vigneron DB, Nelson SJ, Miller BL. Hippocampal CA1 apical neuropil atrophy in mild Alzheimer disease visualized with 7-T MRI. *Neurology* 2010 ;75:1381–1387.
41. Breyer T, Wanke I, Maderwald S, Woermann FG, Kraff O, Theysohn JM, Ebner A, Forsting M, Ladd ME, Schlamann M. Imaging of Patients with Hippocampal Sclerosis at 7 Tesla: Initial Results. *Academic Radiology* 2010 ;17:421–426.
42. Henry TR, Chupin M, Lehericy S, Strupp JP, Sikora MA, Sha ZY, Ugurbil K, Van de Moortele P-F. Hippocampal Sclerosis in Temporal Lobe Epilepsy: Findings at 7 T [Internet]. *Radiology* 2011 ;
43. Abosch A, Yacoub E, Ugurbil K, Harel N. An Assessment of Current Brain Targets for Deep Brain Stimulation Surgery With Susceptibility-Weighted Imaging at 7 Tesla. *Neurosurgery* 2010 ;67:1745–1756.
44. Cho Z-H, Min H-K, Oh S-H, Han J-Y, Park C-W, Chi J-G, Kim Y-B, Paek SH, Lozano AM, Lee KH. Direct visualization of deep brain stimulation targets in Parkinson disease with the use of 7-tesla magnetic resonance imaging. *Journal of Neurosurgery* 2010 ;113:639–647.

45. Moore J, Jankiewicz M, Zeng H, Anderson AW, Gore JC. Composite RF pulses for -insensitive volume excitation at 7 Tesla. *Journal of Magnetic Resonance* 2010 ;205:50–62.
46. Henning A, Fuchs A, Murdoch JB, Boesiger P. Slice-selective FID acquisition, localized by outer volume suppression (FIDLOVS) for (1)H-MRSI of the human brain at 7 T with minimal signal loss. *NMR Biomed* 2009 ;22:683–696.
47. Haines K, Smith NB, Webb AG. New high dielectric constant materials for tailoring the distribution at high magnetic fields. *Journal of Magnetic Resonance* 2010 ;203:323–327.
48. Van de Moortele PF, Pfeuffer J, Glover GH, Ugurbil K, Hu X. Respiration-induced B0 fluctuations and their spatial distribution in the human brain at 7 Tesla. *Magnetic Resonance in Medicine* 2002 ;47:888–895.
49. Barry RL, Williams JM, Klassen LM, Gallivan JP, Culham JC, Menon RS. Evaluation of preprocessing steps to compensate for magnetic field distortions due to body movements in BOLD fMRI. *Magnetic Resonance Imaging* 2010 ;28:235–244.
50. Barmet C, Zanche ND, Pruessmann KP. Spatiotemporal magnetic field monitoring for MR. *Magnetic Resonance in Medicine* 2008 ;60:187–197.

10

Subject tolerance of 7 Tesla MRI examinations

*M.J. Versluis
W.M. Teeuwisse
H.E. Kan
M.A. van Buchem
A.G. Webb
M.J. van Osch*

ABSTRACT

Purpose: To determine the subjective experiences and the sources of discomfort for subjects undergoing 7 Tesla MRI examinations on a whole-body 7 Tesla system within a hospital setting

Materials and Methods: A post-scan survey was filled out by 101 healthy subjects who participated in a 7 Tesla examination. All participants answered questions regarding different potential sensations of discomfort including dizziness, claustrophobia, and scanner noise.

Results: Dizziness was reported most frequently with 34% of subjects experiencing dizziness while moving into the scanner and 30% while moving out of the magnet. Scanner noise was also frequently mentioned as uncomfortable (33% of the subjects). In 11% of the cases a metallic taste was reported. The overall experience was rated by 3% as unpleasant, 51% as neutral and 46% as pleasant.

Conclusion: The reported side effects are larger than previously reported for lower field strengths. However, overall 7 Tesla examinations are well tolerated, with only 3% of subjects rating it as unpleasant. These results agree well with previous in-depth studies, and provide further evidence that 7 Tesla MRI would be accepted by patients in clinical practice.

INTRODUCTION

There has been a rapid increase in the number of whole body 7 Tesla MRI scanners in research centers and hospitals worldwide; at the end of 2011 more than 30 systems were in operation. For 7 Tesla MRI to fulfill the promise of increased spatial resolution and increased sensitivity for the identification of pathologies in the clinical setting, it is important to assess how well examinations are tolerated by subjects and what adverse side effects, if any, are reported and whether they can be easily mitigated. The subjective perception of 7 Tesla examinations is important for local institutional review board (IRB) approval and for acceptance of 7 Tesla MRI as a true “medical device” by the regulatory bodies as opposed to the “investigational status” it has currently.

A number of studies have been performed on high field systems that have examined the possible effects of MRI on human subjects. Earlier studies at different field strengths of up to 9.4 Tesla have shown no effect of the static magnetic field on vital signs, such as blood pressure and heart rate (1–3) and very limited (2, 4) or negligible effects (5, 6) on cognitive function, such as short term memory have been found. A small effect on eye-hand coordination and the visual sensory domain was reported in the stray field of a 7 Tesla magnet, where subjects experienced a maximum of 1.6 Tesla (7). Perceived side effects occur most commonly when the subject moves through a high magnetic field gradient, with a metallic taste reported in 50% of subjects who shook their heads in the stray field of a 7 Tesla magnet (8). Vertigo can be induced by the induction of currents through the vestibular hair cells (9), but most reported side effects are acute and disappear rapidly after the exposure ended (10) and the United States Food and Drug Administration (FDA) has therefore classified MR systems of up to 8 Tesla to be non-significant risk devices for subjects above one month of age (11).

There have been two previous studies performed in subjects undergoing a 7 Tesla examination by the Essen group on a whole-body Siemens system to assess the subjective experience of a large number of both healthy volunteers and patients (12, 13). Their results indicated that feelings of dizziness and general discomfort were more pronounced at 7 Tesla than at 1.5 Tesla, but that overall the general acceptance was high with only ~12% of subjects rating the experience as unpleasant. Since results from subjects undergoing a 7 Tesla MRI exam from only one geographical site and one specific magnet/vendor configuration have so far been reported, it is important to assess whether these findings are similar at other sites and on scanners of other vendors for general acceptance of clinical 7 Tesla MRI. Specifically we report

from experiences on a Philips 7 Tesla scanner which has a slightly smaller diameter than the Siemens scanner in Essen, and which is also geographically located in a clinical hospital environment. Given the somewhat subjective nature of subjects reactions, one other important difference is that the siting-plan of the Philips scanners indirectly “obscures” the long length of the scanner bore (compared to 1.5 and 3 Tesla scanners) by having plastic side-planes which connect to the inside of the shielded room, in contrast to general siting for Siemens systems in which the volunteer can see the entire magnet bore. However the result on the perception of subjects is not clear.

METHODS

101 healthy subjects with mean age of 27 years (range is 18 – 57 years) underwent a 7 Tesla MRI examination on a human Philips Achieva scanner with a clear bore diameter of 58 cm and length of 340 cm. The diameter of 58 cm is slightly smaller than the 59.5 cm for the Siemens scanner used in previous studies: although this difference is small it is likely to have some effect on the experience of patient comfort. Many different scanning protocols were used, incorporating both imaging and spectroscopy, with individual scans ranging in duration from less than a minute to approximately 10 minutes. The types of sequences that were performed have not been recorded, but it has been estimated based on vendor supplied reports that highest noise levels are around 105 dB. In all cases the total scanning period was limited to one hour. All brain examinations were performed using a close fitting 16 channel Nova Medical (Wilmington, MA, USA) phased array receive-coil with a diameter of 29.2 cm and length of 26 cm, other examinations of the knee and calf muscle were performed using various custom built coils. For examinations of the calf muscle and knee, subjects were positioned feet first in the magnet, for examinations of the brain, subjects were head first in the magnet. Subjects were moved manually inside and outside the scanner bore at a constant pace of approximately 7 cm/s. No attempt was made to reduce the table speed in the vicinity of the highest gradient of the magnetic field. Noise protection was provided (3M Ear Classic) with a reported average noise reduction of 28 dB. When space within the coil allowed a custom adapted version of the manufacturer provided headphone was used for additional protection.

In conjunction with our local medical ethics committee a questionnaire was created to assess the experience of the participants in 7 Tesla MRI studies. Participants were recruited using advertisements in public spaces of our hospital and near the lecture rooms for medical students, and received a small compensation in the form of a gift certificate. Similar to examinations per-

formed on the clinical 1.5 Tesla and 3 Tesla scanners in our hospital, before scanning all subjects were informed of possible side-effects: claustrophobia, dizziness, metallic taste, noise and possible muscle twitching. No mention was made that these effects might be more intense than experienced at the lower field systems.

Immediately after the examination was finished the subjects were asked to fill in the questionnaire (see table 1) under supervision of a researcher to ensure accurate understanding of the questions. All questions were answered on the scale: yes, a little, or no except for the final question (overall experience), which was rated: unpleasant, neutral, or pleasant and the open question regarding additional comments of the subjects. The total duration of the examination was also recorded. Differences in side effects between subjects that were head first in the scanner versus feet first were addressed with a χ^2 test (SPSS 17.0, Chicago, US).

Because the primary purpose of the questionnaire was to comply with IRB regulations, additional details regarding scanning protocol, weight and height of subjects and history of previous MRI examinations were not recorded.

RESULTS

The responses to the questionnaire are summarized in figure 1; the findings are shown in descending order according to the number of participants answering yes, except for the last two questions, which were answered mostly positive. The total duration of the examination was approximately one hour (58 ± 8 minutes). The three most frequently reported negative findings (answers yes and a little) were, in descending order, dizziness moving in to the magnet (34%), scanner noise (33%) and dizziness moving out of the magnet (30%). 11% of subjects reported a metallic taste during the examination. Dizziness during scanning was mentioned in a similar number of cases (14%), which was significantly less frequent compared to dizziness while moving into or out from the magnet. This is an indication that both effects are likely to be caused by moving through the strong static magnetic field gradients, as also found in the previous studies (8, 9). Out of the 101 subjects included in this survey only two could not undergo the examination due to severe claustrophobia. One subject reported seeing light flashes during the first 10 minutes inside the scanner and one subject reported sensations of peripheral nerve stimulation. These remarks were reported in the additional comments section of the questionnaire and were not directly targeted as such. Of all cases, 78% were brain examinations, 9% knee examinations and 3% were examinations of the calf muscle, in 10% of the cases it was not possible to re-

trieve retrospectively what body part was imaged. A statistical trend towards more remarks of dizziness was reported by subjects that were head first in the scanner when they were moved outside the bore (χ^2 test, $p = 0.054$). No other differences were found. Whether subjects were well informed prior and during the examination was answered with yes by almost all subjects (98% and 97%, respectively). The large majority of the participants rated the examination as pleasant or neutral, with only 3% of subjects rating the examination as unpleasant, 51% as neutral and 46% as pleasant.

Table 1: Questionnaire
Did you experience dizziness when moving in the scanner?
Did you experience dizziness during scanning?
Did you experience dizziness when moving out the scanner?
Did you experience nausea during the examination?
Did you experience a metallic taste during the examination?
Was it too cold during the examination?
Was it too warm during the examination?
Were you feeling claustrophobic?
Did you suffer from the scanner noise?
Are there any additional comments?
What was your overall experience?
Were you informed well prior to the examination?
Were you informed well during the examination?

All questions were answered on the scale: yes, a little, no except for the last question (overall experience), which was rated: unpleasant, neutral, pleasant and the open question about additional comments.

DISCUSSION

The most important finding of this short survey is that 7 Tesla examinations in a hospital setting were tolerated well by healthy subjects. The most common experience was dizziness while moving inside the scanner bore, which was mentioned more frequently than previously reported at 1.5 Tesla (12), therefore it might be advantageous to inform subjects when they are being moved into the scanner of possible feelings of dizziness. In most cases dizziness was reported to disappear rapidly once inside the scanner. It has been hypothesized that the dizziness during movement is induced by magnetic susceptibility differences between the vestibular organs and the surrounding

fluid and induced currents acting directly on the vestibular hair cells (9).

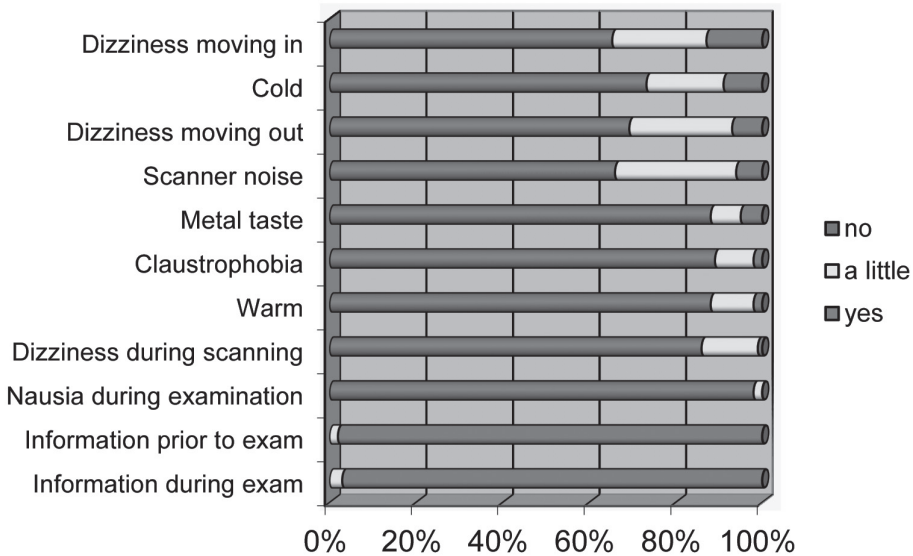


Figure 1: Results of the questions listed in table 1 in 101 subjects.

The most mentioned unpleasant remarks were dizziness when moving in and out of the magnet and the amount of scanner noise.

In terms of direct comparison of the results of this survey compared to the two previous studies in Essen, there is a strong general agreement for many of the either neutral or negative effects. For example, in Theyson et al. (13) approximately 25% of the subjects scanned at 7 Tesla reported dizziness during manual table movement, while our findings show slightly larger numbers (34% and 30% while moving in to and out from the scanner, respectively). More people reported a definite (rather than slight) sense of dizziness moving into the magnet as opposed to moving out, and this can be explained both by initial trepidation at the start of a scan as compared to a more relaxed feeling at the end of the scan in terms of heightened awareness to possible side-effects. Because the table had to be moved manually at the time of this study by different operators, there were variations in table speed between subjects, resulting in corresponding differences in sensations of dizziness. The larger number of subjects reporting dizziness when moving out of the scanner when they were positioned head first in the scanner compared to feet first is likely to be caused by movement of the head through the highest magnetic field gradient. However it must be noted that the number exams performed outside the brain was very limited (12%). Scanner noise is also mentioned frequently as unpleasant, which for studies

of the head could be explained by the limited space available for noise protection. The small size of the receive head coil frequently prevented the use of head phones in addition to ear plugs. This was especially the case for subjects with larger head sizes. A metallic taste was reported by 11% of the subjects, which is more than twice as frequent as previously reported (13) and is thought to be induced by moving through the static magnetic field (8). In contrast to previous studies, the length of the examination was not mentioned specifically by any volunteer as being a problem. There can be several reasons explaining this difference. First, the subjects were explicitly told that the maximum scan duration allowed by our IRB was one hour. Second, throughout the examination the subject was told how long each scan would take (shortest ~1 minute, longest ~10 minutes), and asked after every scan if they were comfortable. Thus full information was available to the subject throughout the examination – in accordance with recommended clinical procedures. A potential bias in the subject recruitment can exist because it was not recorded whether subjects had undergone any previous MRI examinations at lower field strengths, which can influence reported numbers on claustrophobia and other side effects.

Previous literature studies have focused on the effects of (moving through) the static magnetic field and have reported relatively mild effects in line with these findings. The most frequently mentioned effects are caused by moving through the magnetic field, similar to subjects being positioned in the scanner bore in this study and include a metallic taste, dizziness or concentration problems (2, 8–10). However these studies did not include an actual MRI examination, which is likely to influence the overall perception of possible side effects. Operating conditions, such as matching table speed to the position of the head within the magnetic field gradient (slowest speed through the highest gradient) could be adapted to minimize dizziness.

Overall the 7 Tesla MRI examinations were tolerated well, which is confirmed by only 3% of subjects rating the examination as unpleasant. Claustrophobia was only mentioned in a very small number of cases and resulted in only two subjects not being able to participate.

In conclusion, this report supports previous literature in showing that in general 7 Tesla MRI examinations are tolerated well. Very similar reactions were obtained from this current study in a clinical setting with a Philips 58 cm bore diameter magnet as reported previously from a Siemens scanner of 59.5 cm bore diameter. The similarities in two completely different settings, with different manufacturers, provide further evidence that patient acceptance of clinical 7 Tesla is not likely to be problematic.

REFERENCES

1. Atkinson IC, Renteria L, Burd H, Pliskin NH, Thulborn KR. Safety of human MRI at static fields above the FDA 8T guideline: Sodium imaging at 9.4T does not affect vital signs or cognitive ability. *Journal of Magnetic Resonance Imaging* 2007 ;26:1222–1227.
2. Chakeres DW, Kangarlu A, Boudoulas H, Young DC. Effect of static magnetic field exposure of up to 8 Tesla on sequential human vital sign measurements. *Journal of Magnetic Resonance Imaging* 2003 ;18:346–352.
3. Schenck JF. Physical interactions of static magnetic fields with living tissues. *Progress in Biophysics and Molecular Biology* 2005 ;87:185–204.
4. Chakeres DW, de Vocht F. Static magnetic field effects on human subjects related to magnetic resonance imaging systems. *Progress in Biophysics and Molecular Biology* 2005 ;87:255–265.
5. Kangarlu A, Burgess RE, Zhu H, Nakayama T, Hamlin RL, Abduljalil AM, Robitaille PML. Cognitive, cardiac, and physiological safety studies in ultra high field magnetic resonance imaging. *Magnetic Resonance Imaging* 1999 ;17:1407–1416.
6. Schlamann M, Voigt MA, Maderwald S, Bitz AK, Kraff O, Ladd SC, Ladd ME, Forsting M, Wilhelm H. Exposure to high-field MRI does not affect cognitive function. *J. Magn. Reson. Imaging* 2010 ;31:1061–1066.
7. de Vocht F, Stevens T, Glover P, Sunderland A, Gowland P, Kromhout H. Cognitive effects of head-movements in stray fields generated by a 7 Tesla whole-body MRI magnet. *Bioelectromagnetics* 2007 ;28:247–255.
8. Cavin ID, Glover PM, Bowtell RW, Gowland PA. Thresholds for perceiving metallic taste at high magnetic field. *J Magn Reson Imaging* 2007 ;26:1357–61.
9. Glover PM, Cavin I, Qian W, Bowtell R, Gowland PA. Magnetic-field-induced vertigo: A theoretical and experimental investigation. *Bioelectromagnetics* 2007 ;28:349–361.
10. de Vocht F, van Drooge H, Engels H, Kromhout H. Exposure, health complaints and cognitive performance among employees of an MRI scanners manufacturing department. *Journal of Magnetic Resonance Imaging* 2006 ;23:197–204.
11. U.S. FDA. Guidance Documents (Medical Devices and Radiation-Emitting Products) - Guidance for Industry and FDA Staff: Criteria for Significant Risk Investigations of Magnetic Resonance Diagnostic Devices [Internet]. 2003 ;
12. Heilmaier C, Theysohn JM, Maderwald S, Kraff O, Ladd ME, Ladd SC. A large-scale study on subjective perception of discomfort during 7 and 1.5 T MRI examinations. *Bioelectromagnetics* 2011 ;32:610–619.
13. Theysohn JM, Maderwald S, Kraff O, Moenninghoff C, Ladd ME, Ladd SC. Subjective acceptance of 7 Tesla MRI for human imaging. *Magn Reson Mater Phy* 2007 ;21:63–72.



11

General discussion

The development of magnetic resonance imaging (MRI) systems with increasing field strengths is driven by the promise of higher signal-to-noise ratios (SNR) resulting in imaging structures that could not be visualized before. However it is not trivial to obtain the improvements that can be theoretically expected. The transition from a conventional 3 Tesla MRI scanner to a research 7 Tesla system creates intrinsic challenges, such as radiofrequency (RF) inhomogeneity, B_0 inhomogeneity and increased tissue heating that can negate the expected improvements. In this thesis several new techniques have been developed and applied to 7 Tesla MRI to optimally benefit from the expected improvements in SNR, and contrast.

INTRINSIC CHALLENGES OF 7 TESLA MRI

RF field inhomogeneities

Creating a highly homogeneous RF field (B_1) is of great importance for many MR applications. In addition to the homogeneity it needs to be created with high efficiency to reduce the tissue induced heating. However this is not easily achieved. The short wavelength (approximately 11 cm in human tissue) and as a result deconstructive interference of the RF field (1) prohibits, or at least seriously limits the application of conventional RF coils (2, 3) used at lower field strengths. Almost all recently developed pulse sequences and system calibration sequences for 1.5 Tesla and 3 Tesla systems assume a homogeneous B_1 field, therefore a simple translation of protocols will not work at 7 Tesla. There are two ways to mitigate these issues, the first is to develop different coils which are sufficiently homogeneous within a certain region-of-interest (ROI), and the second approach is to develop sequences which are robust to variations in the B_1 -field. Since the introduction of 7 Tesla MRI systems a range of different coils has been developed. When the ROI is sufficiently small, such as for imaging leg muscles, the eye lens, or even the heart or spine, a relatively simple local transmit-receive (Tx/Rx) coils can provide adequate coverage and homogeneity (4–7). This thesis has shown the development of a local Tx/Rx coil for cardiac imaging, which was used to visualize the lumen of the right coronary artery (8). For larger anatomies, or for improved homogeneity more sophisticated design is required using multiple independently driven RF coils simultaneously (B_1 -shimming) to create constructive addition of B_1 -fields (9–11), or using “traveling wave” antennas (12, 13). Concurrently pulse sequences can be adapted to provide robustness for variations in the B_1 -field while staying within the specific absorption rate (SAR) limits for tissue heating. SAR intensive protocols involving turbo spin echo and fluid attenuated inversion recovery sequences have been adapted

to cope with these issues (14). For small targeted areas, such as in single voxel MRS the B_1 field can be considered homogeneous, relatively independent from the used coil configuration. This thesis has shown that a volume specific RF calibration can accurately establish the relation between RF amplifier power and generated B_1 field in a small localized region, resulting in an increased SNR of single voxel spectra obtained in the calf muscle (6).

Although the RF field inhomogeneities of 7 Tesla MRI will likely continue to be a challenge, several techniques, both in hardware and pulse sequences have been developed to overcome some of the issues.

Static magnetic field inhomogeneities

Inhomogeneities in the main magnetic field (B_0) become increasingly larger for higher magnetic field strengths. These inhomogeneities can be separated into static distortions and dynamically fluctuating distortions. The former are created by transitions in magnetic susceptibility between different types of tissue and particularly by air cavities and produces on MR imaging local areas of deformation or signal drop out. The latter can create an overall degradation of image quality, especially for sensitive protocols, such as T_2^* -weighted gradient echo sequences. Higher order shimming is used to counteract the static B_0 inhomogeneities and is available on most 7 Tesla systems. Additional improvements in compensating for static inhomogeneities have been shown using slice specific shim settings, however this requires dedicated hardware (15). Correcting for dynamically fluctuating magnetic fields, which can substantially degrade image quality becomes increasingly important for long scan durations. These fluctuations can be introduced by breathing, coughing or involuntary body movements (16, 17). Solutions have been proposed that prospectively change the shim settings depending on the respiratory cycle (18), by the additional placement of field probes (19, 20) or that retrospectively correct the images using an additionally acquired navigator echo (17, 21). Ultimately when the magnetic field distortions are known in real time it is possible to pro-, or retrospectively correct for the image artifacts, resulting in robust imaging. This thesis has shown that correcting for these artifacts is important for patient studies, which typically are more restless than healthy young volunteers. Similarly the frequent use of high resolution scans with a long scan duration lead to an increased chance of motion induced artifacts.

THE (CLINICAL) VALUE OF 7 TESLA MRI: CURRENT STATUS

Following the technical advancements and solutions to many of the initial problems, 7 Tesla MRI is gradually being used in a clinical setting. To date

the number of pure patient studies is still very limited. By far, the majority of studies have been performed in patients with neurological diseases, likely because the techniques for brain imaging are most developed. Patients with a variety of neurological disorders have been studied. To name a few, in patients with Multiple Sclerosis (MS) enhanced lesion detection and location of lesions was obtained (22–24). In patients suffering from Huntington’s disease (HD) single voxel MRS could be obtained from small brain structures, such as the caudate nucleus and putamen known to be affected by the disease. Due to the increased chemical shift and SNR accurate metabolite concentrations were obtained showing a decrease of NAA, creatine and glutamate levels in patients (25). The visualization of small arteries using time-of-flight (TOF) angiography benefits both from the higher SNR and from the increased background suppression of static tissue due to prolonged T_1 relaxation times. This technique has been applied to visualize the small perforating lenticulostriate arteries in stroke, vascular dementia and in cerebral autosomal-dominant arteriopathy with subcortical infarcts and leukoencephalopathy (CADASIL) patients (26–28). Studies from this thesis have shown the applicability of 7 Tesla MRI in patients with AD (chapters 5 and 8). Based on the phase images from a high resolution T_2^* -weighted sequence, which is very sensitive to changes in the magnetic field homogeneity differences were found between patients and controls. This difference is ascribed to local increases in iron concentration co-localized with Amyloid- β , one of the hallmarks of the disease. This technique benefits from an increased contrast caused by the increased sensitivity to magnetic field inhomogeneities in addition to the higher SNR.

Overall, more clinical studies are expected to be performed in the future, especially because subject tolerance for 7 Tesla examinations is high, as was shown in this thesis (chapter 10) and by others (29). Currently, 7 Tesla brain imaging is the most widely applied, for other anatomies of the human body it is still mainly an experimental system requiring more technical development for use in a clinical environment. Some initial studies using ^{31}P MRS in breast cancer or ^{23}Na imaging in patients after cartilage repair surgery (30, 31) have been performed, but numbers are very limited so far.

FUTURE DIRECTIONS AND OUTLOOK

In the near future, 7 Tesla MRI is not likely going to replace lower field strength MRI for a broad range of applications. The number of problems arising from the transition from 3 Tesla to 7 Tesla is more complicated than the previous transition from 1.5 Tesla. For many applications merely an increase in

SNR does not make up for much increased inhomogeneity, complexity and increased number of contra-indications (e.g. implants). Therefore research efforts need to focus on types of contrast that benefit from the higher magnetic field strength *in addition* to the higher SNR. The most promising applications, such as the detection of microbleeds, measuring disease related changes of iron in AD, single voxel MRS in small structures and native contrast angiography of small vessels all benefit from increased contrast in addition to SNR. In a more research setting is the potential for arterial spin labeling, or blood oxygen level dependent (BOLD) functional MRI.

Combining increased contrast with high resolution scans, often results in long scan durations making scans susceptible to subject induced artifacts. For the robust introduction of 7 Tesla MRI in clinical routine it is important to be able to correct for these artifacts. Proper subject fixation can be used to limit involuntary motion, however fluctuations of the magnetic field due to breathing, coughing or movement of other body parts is more difficult to avoid. A further complicating factor is that the amplitude of the magnetic field fluctuations scales with field strength. Navigator echo based measurement and correction of these fluctuations has already shown to substantially improve image quality (this thesis). Some very promising approaches measure real time field changes using magnetic field probes placed around the body or use multiple receive coil elements to sample the spatial distribution of the magnetic field (this thesis). In conjunction with the ability to prospectively switch higher order gradient shim terms in real time, this would allow for highly robust imaging even for scans with long scan duration. On the longer term with adequate hardware to individually drive multiple RF coils and modified sequences, other anatomies are likely to benefit from similar improvements in contrast and resolution, ultimately leading to improved and earlier diagnosis.

REFERENCES

1. Webb AG, Collins CM. Parallel transmit and receive technology in high-field magnetic resonance neuroimaging. *International Journal of Imaging Systems and Technology* 2010 ;20:2–13.
2. Hayes CE, Edelstein WA, Schenck JF, Mueller OM, Eash M. An efficient, highly homogeneous radiofrequency coil for whole-body NMR imaging at 1.5 T. *J Magn Reson* 1985 ;63:622–628.
3. Vaughan JT, Hetherington HP, Otu JO, Pan JW, Pohost GM. High frequency volume coils for clinical NMR imaging and spectroscopy. *Magn Reson Med* 1994 ;32:206–218.
4. Richdale K, Wassenaar P, Teal Bluestein K, Abduljalil A, Christoforidis JA, Lanz T, Knopp MV, Schmalbrock P. 7 Tesla MR imaging of the human eye in vivo. *J Magn Reson Imaging* 2009 ;30:924–932.
5. Versluis MJ, Tsekos N, Smith NB, Webb AG. Simple RF design for human functional and morphological cardiac imaging at 7tesla. *J. Magn. Reson.* 2009 ;200:161–166.
6. Versluis MJ, Kan HE, van Buchem MA, Webb AG. Improved signal to noise in proton spectroscopy of the human calf muscle at 7 T using localized B1 calibration. *Magn Reson Med* 2010 ;63:207–211.
7. Vossen M, Teeuwisse W, Reijnierse M, Collins CM, Smith NB, Webb AG. A radiofrequency coil configuration for imaging the human vertebral column at 7 T. *Journal of Magnetic Resonance* 2011 ;208:291–297.
8. van Elderen SGC, Versluis MJ, Westenberg JJM, Agarwal H, Smith NB, Stuber M, de Roos A, Webb AG. Right Coronary MR Angiography at 7 T: A Direct Quantitative and Qualitative Comparison with 3 T in Young Healthy Volunteers. *Radiology* 2010 ;257:254–259.
9. van den Bergen B, Van den Berg CAT, Bartels LW, Legendijk JJW. 7 T body MRI: B1 shimming with simultaneous SAR reduction. *Phys Med Biol* 2007 ;52:5429–5441.
10. Adriany G, Van de Moortele P-F, Ritter J, Moeller S, Auerbach EJ, Akgün C, Snyder CJ, Vaughan T, Uğurbil K. A geometrically adjustable 16-channel transmit/receive transmission line array for improved RF efficiency and parallel imaging performance at 7 Tesla. *Magn Reson Med* 2008 ;59:590–597.
11. Dieringer MA, Renz W, Lindel T, Seifert F, Frauenrath T, von Knobelsdorff-Brenkenhoff F, Waiczies H, Hoffmann W, Rieger J, Pfeiffer H, Ittermann B, Schulz-Menger J, Niendorf T. Design and application of a four-channel transmit/receive surface coil for functional cardiac imaging at 7T. *J Magn Reson Imaging* 2011 ;33:736–741.
12. Brunner DO, De Zanche N, Fröhlich J, Paska J, Pruessmann KP. Travelling-wave nuclear magnetic resonance. *Nature* 2009 ;457:994–998.
13. Webb AG, Collins CM, Versluis MJ, Kan HE, Smith NB. MRI and localized proton spectroscopy in human leg muscle at 7 tesla using longitudinal traveling waves. *Magnetic Resonance in Medicine* 2010 ;63:297–302.
14. Visser F, Zwanenburg JJM, Hoogduin JM, Luijten PR. High-resolution magnetization-prepared 3D-FLAIR imaging at 7.0 Tesla. *Magn Reson Med* 2010 ;64:194–202.
15. Juchem C, Nixon TW, Diduch P, Rothman DL, Starewicz P, De Graaf RA. Dynamic shimming of the human brain at 7 T. *Concepts in Magnetic Resonance Part B: Magnetic Resonance Engineering* 2010 ;37B:116–128.

16. Birn RM, Bandettini PA, Cox RW, Jesmanowicz A, Shaker R. Magnetic field changes in the human brain due to swallowing or speaking. *Magnetic Resonance in Medicine* 1998 ;40:55–60.
17. Versluis MJ, Peeters JM, van Rooden S, van der Grond J, van Buchem MA, Webb AG, van Osch MJP. Origin and reduction of motion and f0 artifacts in high resolution T2*-weighted magnetic resonance imaging: application in Alzheimer's disease patients. *Neuroimage* 2010 ;51:1082–1088.
18. Van Gelderen P, de Zwart JA, Starewicz P, Hinks R, Duyn JH. Real-time shimming to compensate for respiration-induced B0 fluctuations. *Magnetic Resonance in Medicine* 2007 ;57:362–368.
19. De Zanche N, Barmet C, Nordmeyer-Massner JA, Pruessmann KP. NMR probes for measuring magnetic fields and field dynamics in MR systems. *Magnetic Resonance in Medicine* 2008 ;60:176–186.
20. Boer VO, Klomp DWJ, Juchem C, Luijten PR, de Graaf RA. Multislice (1) H MRSI of the human brain at 7 T using dynamic B(0) and B(1) shimming. *Magnetic Resonance in Medicine* 2012 ;68:662-670.
21. Versluis MJ, Sutton BP, de Bruin PW, Börnert P, Webb AG, van Osch MJ. Retrospective image correction in the presence of nonlinear temporal magnetic field changes using multichannel navigator echoes. *Magnetic Resonance in Medicine* 2012 ;68:1836-1845.
22. Tallantyre EC, Morgan PS, Dixon JE, Al-Radaideh A, Brookes MJ, Morris PG, Evangelou N. 3 Tesla and 7 Tesla MRI of multiple sclerosis cortical lesions. *J Magn Reson Imaging* 2010 ;32:971–977.
23. Mainero C, Benner T, Radding A, van der Kouwe A, Jensen R, Rosen BR, Kinkel RP. In vivo imaging of cortical pathology in multiple sclerosis using ultra-high field MRI. *Neurology* 2009 ;73:941 –948.
24. Kollia K, Maderwald S, Putzki N, Schlamann M, Theysohn JM, Kraff O, Ladd ME, Forsting M, Wanke I. First Clinical Study on Ultra-High-Field MR Imaging in Patients with Multiple Sclerosis: Comparison of 1.5T and 7T. *AJNR Am J Neuroradiol* 2009 ;30:699–702.
25. van den Bogaard SJA, Dumas EM, Teeuwisse WM, Kan HE, Webb A, Roos RAC, van der Grond J. Exploratory 7-Tesla magnetic resonance spectroscopy in Huntington's disease provides in vivo evidence for impaired energy metabolism. *J. Neurol.* 2011 ;258:2230–2239.
26. Liem MK, van der Grond J, Versluis MJ, Haan J, Webb AG, Ferrari MD, van Buchem MA, Lesnik Oberstein SAJ. Lenticulostriate Arterial Lumina Are Normal in Cerebral Autosomal-Dominant Arteriopathy With Subcortical Infarcts and Leukoencephalopathy. *Stroke* 2010 ;41:2812 –2816.
27. Kang C-K, Wörz S, Liao W, Park C-A, Kim Y-B, Park C-W, Lee Y-B, Rohr K, Cho Z-H. Three dimensional model-based analysis of the lenticulostriate arteries and identification of the vessels correlated to the infarct area: preliminary results. *Int J Stroke* 2012 ;7:558-563.
28. Seo SW, Kang C-K, Kim SH, Yoon DS, Liao W, Wörz S, Rohr K, Kim Y-B, Na DL, Cho Z-H. Measurements of lenticulostriate arteries using 7T MRI: new imaging markers for subcortical vascular dementia. *Journal of the neurological sciences* 2012 ;322:200-205

174 | CHAPTER 11

29. Heilmaier C, Theysohn JM, Maderwald S, Kraff O, Ladd ME, Ladd SC. A large-scale study on subjective perception of discomfort during 7 and 1.5 T MRI examinations. *Bioelectromagnetics*. 2011 ;32:610-619.
30. Klomp DWJ, van de Bank BL, Raaijmakers A, Korteweg MA, Possanzini C, Boer VO, van de Berg CAT, van de Bosch MAAJ, Luijten PR. 31P MRSI and 1H MRS at 7 T: initial results in human breast cancer. *NMR Biomed* 2011 ;24:1337–1342.
31. Schmitt B, Zbyn S, Stelzeneder D, Jellus V, Paul D, Lauer L, Bachert P, Trattnig S. Cartilage quality assessment by using glycosaminoglycan chemical exchange saturation transfer and (23)Na MR imaging at 7 T. *Radiology* 2011 ;260:257–264.



Summary and Conclusions

SUMMARY

The aim of this thesis was to develop methods to enable the use of 7 Tesla MRI in clinical practice. Since the installation of the first whole body 7 Tesla magnet, less than 15 years ago, research in this field has seen a rapid increase, with over 40 human in vivo studies published in 2011 (PubMed). However to date, the number of clinical studies has been rather limited. One of the reasons is that translating existing techniques from lower field strengths to 7 Tesla is far from trivial in many cases. Intrinsic properties related to the high field, such as increased sensitivity to magnetic field inhomogeneities and reduced homogeneity of transmit and receive fields require specific sequence and hardware modifications. A simple translation of protocols from lower field strength to higher field is likely to deliver sub optimal results, or even worse results than obtained at lower field strengths. In this thesis a number of technical developments have been performed to facilitate clinical studies and to achieve the full potential that high field has to offer in terms of increased signal-to-noise, contrast and spatial resolution.

The first part describes techniques to improve MR applications in the heart and calf muscle.

Chapter 2 describes the development of a local transmit-receive coil to facilitate cardiac imaging. Different coil configurations have been tested to achieve a B_1 transmit field without tissue induced signal voids, caused by destructive B_1 interference due to the small RF wavelength. Empirically different coils were optimized, using a single loop configuration and a quadrature dual loop configuration. It was shown that using a relatively simple quadrature local transmit-receive coil sufficient coverage to image a large part of the heart could be obtained without introducing any signal voids in this region. RF safety validations were performed to ensure imaging experiments stayed within specific absorption rate (SAR) limit. Several applications of this coil were shown to be feasible, including functional cine moving heart imaging and morphological imaging of the right coronary artery (RCA)

The coil and techniques described in the previous chapter are used in **chapter 3** to image the RCA and to compare the results with a similar protocol at 3 Tesla. Ten healthy volunteers were included and images of the RCA were obtained at 3 Tesla and at 7 Tesla, while keeping the protocols as comparable as possible. The following measurements were performed at both field strengths to quantify the visualization of the coronary artery. Contrast-to-noise ratio between blood and epicardial fat, signal-to-noise ratio of the blood pool, RCA vessel sharpness, diameter, and length; and navigator efficiency. Incre-

ased vessel sharpness and signal-to-noise ratio were found at 7 Tesla. Overall in young healthy volunteers the image quality at 7 Tesla was equal or better than obtained at 3 Tesla.

In **chapter 4** a new calibration method is introduced that measures the B_1 transmit field in a small region of interest. To achieve a certain flip angle the RF amplifier needs to be calibrated depending on location, coil positioning and subject size. Conventionally this is done over a large region, because at lower field strengths the flip angle can be considered constant to a high degree. At 7 Tesla this assumption does not hold, because of the smaller wavelength of the RF field and the frequent use of local intrinsically inhomogeneous transmit coils therefore a new calibration method was developed. Because this method needs to be performed before each scan, it should be very fast without user interaction. The method that was developed used the ratio of two stimulated echoes to derive the actual flip angle. The power setting of the RF amplifier was subsequently iterated to reach the desired flip angle. Using this method an increased signal-to-noise ratio was obtained for localized spectroscopy scans acquired from the calf muscle compared to the conventional calibration method. The exact increase was dependent on the location with respect to the partial volume transmit-receive coil. Generally increases were larger for regions where the local B_1 field was more inhomogeneous.

The second part is concerned with technical developments for high resolution brain imaging.

In **chapter 5** high resolution T_2^* -weighted imaging is performed in Alzheimer's disease (AD) patients. One of the hallmarks of this disease is the aggregation of a protein (amyloid β) that is co-localized with iron. High resolution T_2^* -weighted imaging is a promising technique to image these deposits especially at high magnetic field strengths. However the image quality was found to be severely reduced in AD patients compared to previously acquired images in healthy volunteers. It was hypothesized that the images were degraded due to dynamic fluctuations of the static magnetic field (B_0 fluctuations). This was subsequently confirmed in healthy volunteers where comparable artifacts were observed when similar magnetic field fluctuations were synthetically added to the acquisition. These B_0 fluctuations are introduced by respiration and coughing, but also likely due to body movements not related to head motion. In addition, it was shown that the effect of typical translational and rotational head motion had a much smaller effect on the resulting image-quality. The T_2^* -weighted sequence was modified to include a navigator echo to dynamically estimate magnetic field changes during image acqui-

sition. Retrospectively this information was used in image reconstruction to substantially improve image quality in all cases enabling high quality imaging in AD patients.

An extension of this technique is described in **chapter 6**. Even after correction using the navigator echo technique, the images remained typically of lower quality than images obtained in healthy volunteers. It was hypothesized that the magnetic field fluctuations observed in AD patients had a spatial distribution within an acquired slice, whereas the previously proposed navigator technique was capable of only measuring a global B_0 offset in a slice for each RF excitation. In this chapter a sensitivity encoded (SENSE) navigator was introduced that samples the magnetic field using the 32 receive channels that were available. Because each element sampled signal from a small location of the head only, a spatial estimation of the underlying magnetic field could be obtained by combining the navigator with separately acquired coil sensitivity profiles. This approach was extended to include a frequency readout gradient to improve the magnetic field estimation further. High resolution T_2^* -weighted images were acquired in volunteers while they were intentionally touching their nose or taking deep breaths, to mimic the worst case magnetic field fluctuations seen in AD patients. It was found that the SENSE navigator technique could accurately estimate the induced B_0 -fluctuations. In the second part of this chapter a reconstruction framework is introduced that uses the spatially and dynamically fluctuating magnetic fields to retrospectively correct the images. The complexity of the reconstruction scales to the fourth power of the acquisition matrix, therefore an iterative solver was used based on conjugate gradient minimization to limit memory requirements and reconstruction times. Results show a much improved image quality. The approach using the SENSE navigator including frequency encoding yielded optimal results. Future patient studies are needed to validate this technique in clinical practice.

The long scan duration of most high resolution T_2^* -weighted sequences limits whole brain coverage, in **chapter 7** a new fast volumetric 3D echo planar imaging (EPI) protocol is introduced. By employing the high efficiency of EPI, typically used for fast low resolution functional brain imaging an improved SNR efficiency was obtained. The proposed sequence was compared to a conventional 3D T_2^* -weighted protocol, with the same resolution, amount of T_2^* weighting and scan duration. The spatial coverage of the EPI based protocol was a factor of 4.5 larger, while also the SNR was a factor of 2 increased. This effectively enabled whole brain acquisition of 0.5 mm isotropic resolution in less than 6 minutes of scanning time. The longer readout train in the

EPI protocol inevitably results in more spatial distortion and possibly areas of signal voids. However with the chosen parameters there were no apparent regions of signal voids and the distortion was less than 3 mm for the lowest slices. Due to magnetic field inhomogeneities these slices are most prone to distortion; the amount of distortion for the slices higher in the brain was therefore much less. The new sequence provides the necessary steps, such as resolution and coverage to utilize the high T_2^* contrast of high field MRI.

The third part of the thesis is focused on the current clinical applications of 7 Tesla MRI.

In **chapter 8** T_2^* -weighted imaging has been performed in AD patients to image changes occurring in the cortex related to the deposition of Amyloid- β and iron. The phase of the complex MRI signal of a T_2^* -weighted sequence is very sensitive to changes in iron deposition. Therefore T_2^* -weighted images were acquired in 15 mild to moderate AD patients and 16 control subjects. Phase measurements were performed in the cortex of different regions of the brain and in the hippocampus. It was found that the phase shift between gray and white matter in the cortex was increased in AD patients and that these differences were strongly associated to the Mini Mental State Examination, which tests basic cognitive functions. No differences were found in the hippocampus phase values. Therefore the increased cortical phase values on T_2^* -weighted images might provide a new biomarker that measures early changes related to amyloid pathology.

Chapter 9 reviews the current status of studies performed in patients with neurodegenerative diseases performed at 7 Tesla. Some of the technical challenges and solutions are discussed. Despite the limited number of purely clinical studies to date promising additional features in contrast can be obtained that may assist in better diagnosis of these disorders. High field MRI allowed to visualize the lenticulostriate arteries with great detail in patients with cerebral autosomal dominant arteriopathy with subcortical infarcts and leukoencephalopathy (CADASIL). In patients with AD and hippocampal sclerosis anatomical changes were observed using high resolution imaging. The increased contrast and resolution allowed visualizing the perivenous location of multiple sclerosis lesions and the frequent cortical involvement. Given the rapid progress over the last years it is expected that the contribution of 7 Tesla MRI especially in the field of neurodegenerative diseases will increase over time. Many of the initial problems related to magnetic and RF field inhomogeneities and the lack of optimized sequences have been solved or improved.

The acceptance of 7 Tesla MRI examinations by subjects is discussed in **chapter 10**. In order to fulfill the promise of increased spatial resolution and increased sensitivity for the identification of pathologies in the clinical setting, it is important to assess how well examinations are tolerated by subject and to identify potential adverse side effects. A total of 101 healthy subjects filled out a post scan survey with questions related to potential sensations of discomfort, such as nausea, vertigo and scanner noise. The most frequent (34% of subjects) mentioned negative finding was dizziness while moving in the scanner, followed by scanner noise (33%) and dizziness moving out (30%), also a metallic taste was reported in about 1 in 10 cases. Although the sensations of discomfort are mentioned more frequently than at lower field strength, overall the examinations were tolerated very well. Only 3% of the subjects rated the examination as unpleasant. These results provide further evidence that 7 Tesla MRI would be accepted by patients as with lower field strength examinations.

CONCLUSIONS

This thesis has shown that in order to fully benefit from the expected increase in signal-to-noise ratio and improved contrast of 7 Tesla specific sequence and hardware adaptations are necessary. Many standard techniques from lower field strength require to be redesigned taking into account the specific constraints of 7 Tesla MRI, such as inhomogeneous RF fields (**chapters 2, 3 and 4**) and increased sensitivity to B_0 artifacts (**chapters 5 and 6**). With proper adjustments it is possible to perform studies in almost all anatomies including difficult regions, such as the heart. The promises of 7 Tesla: higher SNR, resolution and faster scanning can be (partly) fulfilled. This has resulted in improved visualization of the right coronary artery, compared to 3 Tesla. With specific calibration sequences that take into account the inhomogeneous RF distribution the SNR of spectra obtained in the calf muscle could be improved. The high magnetic field strength results in very high contrast of T_2^* -weighted images; however the sensitivity to B_0 fluctuations can deteriorate the image quality substantially when applied in patients, who are typically more restless than healthy subjects. A correction technique was developed to reduce these artifacts, which allowed imaging of Alzheimer's disease patients with high image quality (**chapters 5, 6 and 8**). Improvements in the efficiency of T_2^* -weighted sequences resulted in whole brain acquisitions within acceptable scanning times (**chapter 7**), which is of great importance for the clinical introduction. Over the years the number of studies has steadily increased, however there is still only a limited number of pure clinical patient studies performed. The diagnostic added value of 7 Tesla MRI is

beginning to be demonstrated in patients with neurodegenerative diseases, which is also a large part of the patient studies performed so far (**chapter 9**). The largest advances are mainly seen in increased resolution resulting in more accurate visualization of Multiple sclerosis lesions, or visualization of small vessels that were previously not visible at lower field strengths. Visualization of microbleeds and changes in iron deposition, common to many neurodegenerative diseases, such as Alzheimer's disease is improved due to both the increased resolution and the increased sensitivity to iron deposition (**chapters 8 and 9**). The larger spectral separation of metabolites due to an increased chemical shift results in more accurate quantification of metabolites in for example Huntington's disease patients. Patient acceptance is of importance when 7 Tesla MRI is to be used in regular clinical practice, in healthy subjects the 7 Tesla examinations were tolerated very well (**chapter 10**).

These initial findings combined with the fact that 7 Tesla examinations are well tolerated by subjects will likely result in more clinical examinations performed at 7 Tesla. Due to some intrinsic issues (mainly B_1 and B_0) and the high cost, 7 Tesla MRI is not likely to replace all studies currently performed at lower field strength. Therefore it should probably not be considered to be a "one-stop-shop" technique; some applications are better served at lower field strength. High resolution brain imaging; especially combined with the increased sensitivity to the distribution of iron, or the ability to visualize very small arteries has already shown added value and could lead to new insight in early disease processes of neurodegenerative diseases. Future clinical research should focus on these areas, which could improve patient outcome. For most other anatomies more technical developments are needed before the full benefit of 7 Tesla MRI can be obtained.



Samenvatting en Conclusies

SAMENVATTING

Het doel van dit proefschrift was om methoden te ontwikkelen voor de klinische toepassing van 7 Tesla (T) magnetische resonantie beeldvorming (Magnetic Resonance Imaging, MRI). Ongeveer 15 jaar geleden is de eerste 7 T scanner geïntroduceerd met een diameter die groot genoeg is voor het gehele menselijke lichaam. Sindsdien heeft er veel wetenschappelijk onderzoek met behulp van 7 T MRI plaatsgevonden. In 2011 zijn er meer dan 40 in vivo studies gepubliceerd (PubMed). Echter het aantal puur klinische studies is nog zeer beperkt. Een van de redenen is dat bestaande methoden die gebruikt worden op lagere veldsterktes niet gemakkelijk aan te passen zijn voor 7 T. Door verstoringen die direct gerelateerd zijn aan het hoge veld, zoals de toegenomen gevoeligheid voor magnetische veldinhomogeniteiten (B_0) en de verminderde homogeniteit van de zend- en ontvangstvelden (B_1) zijn er specifieke protocol en scanner aanpassingen nodig. Wanneer scan protocollen en technieken van een lagere veldsterkte zonder aanpassingen worden overgenomen zijn de behaalde resultaten meestal suboptimaal dan wel slechter. In dit proefschrift wordt een aantal technische ontwikkelingen beschreven om klinische studies mogelijk te maken en zo het volledige potentieel van hoog veld te benutten. Een aantal voordelen van 7 T MRI zijn de toegenomen signaal ruis verhouding, contrast en spatiële resolutie.

In het eerste deel worden technieken beschreven om de toepassing van MRI in het hart en de kuitspier te verbeteren.

Hoofdstuk 2 beschrijft de ontwikkeling van een lokale zend- en ontvangstspoel om beeldvorming van het hart mogelijk te maken. Verschillende spoelconfiguraties zijn onderzocht om een B_1 -zend veld te creëren zonder gebieden met destructieve interferentie. Deze interferenties worden veroorzaakt door de kortere radiofrequente (RF) golflengte bij een hoger magnetisch veld. Verschillende spoelen zijn empirisch geoptimaliseerd waaronder een enkele “loop” spoel en een kwadratuur dubbele loop spoel. Met een vrij eenvoudige kwadratuur spoel was het mogelijk om een voldoende groot gebied van het hart in beeld te brengen, zonder gebieden van destructieve interferentie. RF veiligheidsvalidaties zijn uitgevoerd om te zorgen dat de experimenten binnen de veiligheidsmarges vallen, de zogeheten Specific Absorption Rate (SAR). In dit hoofdstuk worden enkele toepassingen van deze kwadratuur spoel getoond, zoals beeldvorming van het bewegende hart (cine) en morfologisch beeldvorming van het rechter coronair vat (RCA).

De verschillende spoelen en technieken die in het vorige hoofdstuk zijn beschreven, worden gebruikt in **hoofdstuk 3** om in studieverband de RCA

af te beelden. Tien gezonde vrijwilligers zijn middels een nagenoeg identiek protocol gescand met een 3 T en 7 T MRI scanner. Er zijn verschillende metingen uitgevoerd, onder andere is er gekeken naar de verhouding tussen contrast en ruis van bloed en epi cardiaal vet, de signaal-ruis ratio van bloed, de vaatscherpte van de RCA als ook de diameter, lengte en efficiëntie van de navigator bewegingscorrectie. De beelden vervaardigd op de 7 T MRI scan toonden een toegenomen vaatscherpte en signaal-ruis ratio ten opzichte van de op 3 T verkregen resultaten.

In **hoofdstuk 4** wordt een nieuwe kalibratiemethode geïntroduceerd die lokaal het zend B_1 -veld bepaalt. De RF versterker moet gekalibreerd worden om een bepaalde fliphoek die is gerelateerd aan het B_1 -veld, te verkrijgen. De waarde van de kalibratie hangt af van de locatie in het lichaam, de positie van de spoel en de lichaams grootte. Het is gebruikelijk bij lagere veldsterktes om de meting uit te voeren over een groot gebied, omdat voor deze veldsterktes de flip hoek als constant verondersteld kan worden binnen dit gebied. Voor 7 T gaat deze aanname niet meer goed op door de kortere golflengte van het RF veld en het frequente gebruik van lokale, intrinsiek inhomogene zendspoelen. De nieuwe kalibratiemethode die is ontwikkeld gebruikt de verhouding tussen twee signalen, zogenaamde gestimuleerde echo's, om de flip hoek te bepalen in een klein zelf te bepalen gebied. Door een aantal iteraties met verschillende RF instellingen kon de juiste fliphoek gevonden worden. Om het effect van de methode aan te tonen is deze gebruikt voor gelokaliseerde spectroscopie scans van de kuitspier. Dit zijn scans die zeer gevoelig zijn voor een juiste bepaling van de fliphoek. Wanneer deze nieuwe methode werd gebruikt werd er een hogere signaal-ruis ratio gevonden, dan met de conventionele methode, wat aantoont dat de nieuwe methode tot een nauwkeurigere fliphoek bepaling leidt. De exacte toename was afhankelijk van de locatie van het meetgebied (voxel) in verhouding tot de zendspoel. Over het algemeen was de toename hoger voor gebieden waar het B_1 -veld minder homogeen was, op grotere afstand van de spoel.

Het tweede deel van dit proefschrift beschrijft technische ontwikkelingen voor hoge resolutie visualisatie van het brein.

In **hoofdstuk 5** wordt T_2^* -gewogen (een MRI contrast gevoelig voor veldverstoringen) beeldvorming beschreven in patiënten met de ziekte van Alzheimer (AD). Een van de kenmerken van deze ziekte is de opeenhoping van een eiwit (β -amyloïde) met ijzer. Hoge resolutie T_2^* -gewogen beeldvorming is een veelbelovende techniek om deze afzettingen te visualiseren. Echter de beeldkwaliteit was ernstig verslechterd wanneer deze techniek werd toegepast in AD patiënten vergeleken met beelden in

gezonde vrijwilligers. De hypothese was dat de afname in beeldkwaliteit veroorzaakt werd door fluctuaties in het statische magnetische veld (B_0 -fluctuaties). Dit werd bevestigd in beelden van gezonde vrijwilligers waar deze B_0 -fluctuaties kunstmatig aan toe werden gevoegd tijdens acquisitie, wat leidde tot vergelijkbare artefacten. De B_0 -fluctuaties worden veroorzaakt door ademhaling en hoesten, maar ook door lichaamsbewegingen die niet gerelateerd zijn aan bewegingen van het hoofd. Verder werd aangetoond dat typische hoofdbewegingen (translaties en rotaties) tijdens acquisitie, een veel kleiner effect op de beeldkwaliteit hadden dan B_0 -fluctuaties. Aan de T_2^* -gewogen sequentie is een “navigator echo” toegevoegd, waarmee dynamisch de B_0 -fluctuaties gemeten konden worden tijdens acquisitie. Deze informatie kon achteraf gebruikt worden in de reconstructie om de beeldkwaliteit aanzienlijk te verbeteren. Hierdoor was het mogelijk om in AD patiënten een goede beeldkwaliteit te behalen.

Een uitbreiding van deze techniek wordt beschreven in **hoofdstuk 6**. Na correctie met de hiervoor beschreven navigator echo techniek waren de beelden nog altijd van een mindere kwaliteit dan in gezonde vrijwilligers. De hypothese was dat de magnetische veldfluctuaties die gemeten werden in AD patiënten een spatiële verdeling hadden. De eerder genoemde navigator echo correctie was in staat om alleen globale B_0 afwijkingen in een enkele plak te meten en niet de mogelijke spatiële component. In dit hoofdstuk is een nieuwe navigator geïntroduceerd, de “sensitivity encoded navigator (SENSE navigator) die het magnetische veld meet met behulp van de 32 ontvangst spoelen van de hoofdspool. Omdat elk afzonderlijk element alleen signaal ontvangt van een klein gebied in het hoofd, is het mogelijk om hieruit de spatiële distributie van het magnetische veld af te leiden door deze metingen te combineren met apart gemeten spoelgevoeligheidsprofielen. Deze methode is verder uitgebreid met een frequentie-gecodeerde uitleesgradiënt, die de meting nog nauwkeuriger maakte. Hoge resolutie T_2^* -gewogen opnames zijn gemaakt in gezonde vrijwilligers terwijl ze gevraagd waren hun neus aan te raken, of diep in en uit te ademen, om zo de gevonden veldverstoringen in patiënten na te bootsen. De SENSE navigator techniek was in staat om nauwkeurig de geïnduceerde B_0 -fluctuaties te meten. In het tweede deel van dit hoofdstuk wordt een reconstructie methode geïntroduceerd die de spatiële en dynamische magneetveld veranderingen gebruikt om de beelden te corrigeren. De complexiteit van de reconstructie schaalte met de vierde macht van de acquisitiematrix, daarom is er gekozen voor een iteratieve oplossing gebaseerd op de geconjugeerde gradiënt minimalisatie om zo het geheugengebruik en de reconstructie tijd te minimaliseren. Resultaten laten zien dat met deze methode de beeldkwaliteit sterk verbeterd kon worden. De aanpak die gebruik maakte van de SENSE navigator in

combinatie met de frequentie uitleescodering leverde de beste resultaten. Patientenstudies zijn de volgende stap om deze nieuwe techniek in de klinische praktijk te kunnen valideren en implementeren.

De lange scan tijd van de meeste hoge resolutie T_2^* -gewogen scans beperkt de toepassing om het hele brein af te beelden met deze techniek.

In **hoofdstuk 7** wordt een nieuw en snel 3D echo planar imaging (EPI) protocol geïntroduceerd. Deze techniek heeft een zeer hoge efficiëntie waardoor het mogelijk was om een hoge signaal-ruis efficiëntie te behalen. Normaal gesproken wordt deze techniek alleen gebruikt voor snelle lage resolutie functionele MR, omdat er mogelijk meer vervormingen kunnen optreden. Om dit te onderzoeken is de voorgestelde EPI sequentie vergeleken met een conventionele 3D T_2^* -gewogen protocol met gelijke resolutie, T_2^* weging en scantijd. Het spatiële bereik van het EPI protocol was een factor 4.5 groter dan het conventionele protocol en er werd een toename van een factor 2 in signaal-ruis ratio gemeten. Dit maakte het mogelijk om het hele brein af te beelden met een isotrope resolutie van 0.5 mm, in minder dan 6 minuten scantijd. De langere uitleestrein van het EPI protocol zorgt onvermijdelijk voor meer vervorming en mogelijke gebieden van signaaluitval. Echter met de gekozen parameters voor het protocol konden beide tot een minimum beperkt worden. De vervorming was minder dan 3 mm voor de laagste breinplakken. Omdat de magnetische veldstoring het grootst is in de laagste plakken, zijn deze het meest gevoelig voor vervormingen, de vervormingen van andere hoger gelegen plakken is dan ook veel minder. De nieuwe sequentie levert de stappen die nodig zijn, zoals resolutie en scan bereik om optimaal gebruik te maken van het hoge T_2^* -gewogen contrast van 7 T MRI.

Het derde deel van dit proefschrift is gericht op huidige klinische toepassingen van 7 T MRI.

Hoofdstuk 8 beschrijft beeldvorming in AD patiënten met als doel veranderingen in de cortex ten gevolge van de opeenhoping van β -Amyloïde en ijzer weer te geven. De fase van het complexe MRI signaal van een T_2^* -gewogen sequentie is erg gevoelig voor veldverstoringen ten gevolge van onder andere toename van ijzerconcentratie. Er zijn T_2^* -gewogen beelden geacquireerd in 15 mild tot matig aangedane AD patiënten en 16 gezonde controle personen. Fase metingen zijn uitgevoerd in de cortex van verschillende hersengebieden en in de hippocampus. Er werd een toename van het fase verschil gevonden tussen grijze en witte stof in de cortex van AD patiënten vergeleken met gezonde personen. Deze verschillen waren sterk geassocieerd met de "Mini Mental State Examination" (MMSE), een test voor de meest fundamentele cognitieve

functies. Geen verschillen werden gevonden in de hippocampus fase waarden. De toegenomen fase verschillen op T_2^* -gewogen beelden zouden een nieuwe biomarker kunnen zijn om vroege veranderingen gerelateerd aan amyloïde pathologie te meten.

In **hoofdstuk 9** wordt de huidige status van klinische studies op 7 T met patiënten met neurodegeneratieve aandoeningen besproken. Een aantal van de technische uitdagingen en oplossingen wordt behandeld. Ondanks het beperkte aantal puur klinische studies tot nog toe, zijn er de volgende veelbelovende resultaten verkregen die mogelijk kunnen leiden tot een betere diagnose. Met 7 T MRI was het mogelijk om de lenticulostriate arteriën in groot detail te visualiseren in patiënten met CADASIL (cerebral autosomal dominant arteriopathy with subcortical infarcts and leukoencephalopathy). Dit is nog niet eerder vertoond op een lagere veldsterkte. In AD patiënten en patiënten met hippocampus sclerose zijn anatomische veranderingen in de substructuren van de hippocampus gevonden door gebruik te maken van hoge resolutie beeldvorming. Het toegenomen contrast en de hoge resolutie maakten het mogelijk om de periveneuze locatie van multiple sclerose laesies in beeld te brengen als ook de veel voorkomende corticale deelname van deze afwijkingen. Dit zijn slechts enkele voorbeelden, gezien de snelle vooruitgang van de afgelopen jaren is het te verwachten dat de bijdrage van 7 T MRI, vooral in het veld van neurodegeneratieve ziektes, zal toenemen. Veel van de aanvankelijke problemen gerelateerd aan bv. RF veld inhomogeniteiten en het gebrek aan geoptimaliseerde sequenties zijn reeds opgelost.

Hoe personen een 7 T MRI onderzoek beleven wordt beschreven in **hoofdstuk 10**. Om de belofte van een hogere spatiële resolutie en toegenomen gevoeligheid om ziektes te detecteren waar te maken, is het belangrijk te onderzoeken hoe 7 T onderzoeken worden verdragen en wat de mogelijke bijwerkingen zijn. In totaal hebben 101 gezonde personen die een 7 T onderzoek hadden ondergaan een vragenlijst ingevuld met vragen over mogelijke ongemakken, zoals misselijkheid, duizeligheid en lawaai van de scanner. Het meest genoemd (34% van de personen) was duizeligheid tijdens het inschuiven in de scanner, gevolgd door last van scanner lawaai (33%) en duizeligheid tijdens het uitschuiven uit de scanner (30%). Een metaalsmaak werd genoemd door ongeveer 1 van de 10 personen. Ofschoon er vaker melding werd gemaakt van bij-effecten dan bij onderzoeken op een lagere veldsterkte noemde maar 3% van de personen het 7 T onderzoek onaangenaam. Deze resultaten zorgen voor verder bewijs dat 7 T MRI goed verdragen wordt door patiënten.

CONCLUSIE

Dit proefschrift laat zien dat om volledig te profiteren van de verwachte toename in signaal-ruis ratio en toegenomen contrast, er specifieke sequentie en hardware aanpassingen nodig zijn. Veel van de standaard technieken, die op lagere veldsterktes gebruikt worden, vereisen aanpassingen om rekening te houden met specifieke randvoorwaarden van 7 T, zoals inhomogene RF velden (**hoofdstuk 2,3 en 4**) en toegenomen gevoeligheid voor B_0 artefacten (**hoofdstuk 5 en 6**). Met de juiste aanpassingen is het mogelijk om studies uit te voeren in bijna alle anatomische structuren, waaronder ook lastige gebieden zoals het hart. De belofte van 7 T MRI: hogere signaal-ruis ratio, resolutie en sneller scannen kunnen (gedeeltelijk) waar worden gemaakt. Dit heeft geresulteerd in een verbeterde visualisatie van de rechter coronair arterie. Met behulp van specifieke kalibratie methodes die rekening houden met de inhomogene RF verdeling was het mogelijk om een hogere signaal-ruis ratio te behalen in MR spectra van de kuitspier. De hoge magnetische veldsterkte zorgt voor een zeer hoog contrast op T_2^* -gewogen beelden, alleen neemt hiermee ook de gevoeligheid voor artefacten veroorzaakt door B_0 -fluctuaties toe. In patiënten, die vaak minder goed stil kunnen liggen dan gemotiveerde (zou je gemotiveerd ook zo noemen, alsof patiënten niet gemotiveerd zijn) gezonde vrijwilligers, levert dit een sterke verslechtering van de beeldkwaliteit op. Een correctietechniek om deze artefacten te verminderen was ontwikkeld, waarmee het mogelijk werd om met hoge kwaliteit beelden op te nemen in AD patiënten (**hoofdstuk 5,6 en 8**). Verbeteringen in de efficiëntie van T_2^* -gewogen sequenties resulteerden in beeldvorming van de gehele hersenen binnen een klinisch geaccepteerde scantijd. Dit is van groot belang voor de klinische introductie van 7 T MRI.

De afgelopen jaren is het aantal 7 T studies voortdurend toegenomen, toch is er nog maar een klein aantal puur klinische studies. De diagnostische toegevoegde waarde van 7 T MRI begint zichtbaar te worden in studies met patiënten met neurodegeneratieve aandoeningen. Het grootste aandeel van klinische studies tot nu toe onderzoekt dan ook patiënten met neurodegeneratieve aandoeningen. De hoge resolutie die te behalen is met 7 T MRI, heeft geleid tot een nauwkeurigere visualisatie van Multiple Sclerose afwijkingen en de weergave van kleine vaten die niet zichtbaar zijn op lagere veldsterktes. De visualisatie van microbloedingen en veranderingen van ijzer ophoping, beide veel voorkomend bij neurodegeneratieve aandoeningen, zoals de ziekte van Alzheimer, is verbeterd door de hogere resolutie en de hogere gevoeligheid voor ijzer (**hoofdstuk 8 en 9**). De grotere spectrale scheiding van metabolieten door de toegenomen “chemical shift” resulteert in een nauwkeurigere

kwantificatie van metabolieten in bijvoorbeeld de ziekte van Huntington. De 7 T MRI onderzoeken werden goed verdragen door gezonde vrijwilligers die deel hadden genomen aan een onderzoek (**hoofdstuk 10**), wat een belangrijk voor de klinische introductie.

Deze bevindingen uit de beginfase van 7 T MRI, gecombineerd met de hoge tolerantie van personen voor 7 T MRI onderzoeken, zal hoogstwaarschijnlijk leiden tot meer klinische toepassingen. Door een aantal van de inherente problemen (B_1 en B_0) en de hoge kosten zal 7 T MRI niet alle studies vervangen die op dit moment op lagere veldsterktes uitgevoerd worden. Sommige toepassingen lenen zich beter voor lagere veldsterktes, omdat de verwachte toegevoegde waarde niet opweegt tegen de toegenomen problemen. Hoge resolutie beeldvorming van het brein en dan vooral gecombineerd met de hoge gevoeligheid voor ijzer concentraties, of de mogelijkheid om zeer kleine vaten in beeld te brengen hebben al toegevoegde waarde laten zien. Op termijn kan dit leiden tot betere inzichten in vroege ziekteprocessen van onder andere neurodegeneratieve aandoeningen. Verder klinisch onderzoek zou zich moeten richten op deze reeds veelbelovende toepassingen, die mogelijk zullen leiden to een vroege en betrouwbare klinische diagnose. Voor de meeste andere anatomische gebieden is er nog meer technische ontwikkeling nodig om volledig te kunnen profiteren van 7 T MRI.

List of publications

JOURNAL ARTICLES

- Poser B.A., **Versluis M.J.**, Hoogduin J.M., Norris D.G., 2006. BOLD contrast sensitivity enhancement and artifact reduction with multiecho EPI: parallel-acquired inhomogeneity-desensitized fMRI. *Magnetic Resonance in Medicine*, 55(6), pp.1227-1235.
- Rizzo Sierra C.V., **Versluis M.J.**, Hoogduin J.M., Duifhuis H.D., 2008. Acoustic FMRI noise: linear time-invariant system model. *IEEE Transactions on Bio-Medical Engineering*, 55(9), pp.2115-2123.
- Versluis M.J.**, Tsekos N., Smith N.B., Webb A.G., 2009. Simple RF design for human functional and morphological cardiac imaging at 7tesla. *Journal of Magnetic Resonance*, 200(1), pp.161-166.
- van Elderen S.G.C., **Versluis M.J.**, Webb A.G., Westenberg J.J.M., Doornbos J., Smith N.B., de Roos A., Stuber M., 2009. Initial results on in vivo human coronary MR angiography at 7 T. *Magnetic Resonance in Medicine*, 62(6), pp.1379-1384.
- Versluis M.J.**, Kan H.E., van Buchem M.A., Webb A.G., 2010. Improved signal to noise in proton spectroscopy of the human calf muscle at 7 T using localized B1 calibration. *Magnetic Resonance in Medicine*, 63(1), pp.207-211.
- Webb A.G., Collins C.M., **Versluis M.J.**, Kan H.E., Smith N.B., 2010. MRI and localized proton spectroscopy in human leg muscle at 7 Tesla using longitudinal traveling waves. *Magnetic Resonance in Medicine*, 63(2), pp.297-302.
- Versluis M.J.**, Peeters J.M., van Rooden S., van der Grond J., van Buchem M. A., Webb A.G., van Osch M.J.P., 2010. Origin and reduction of motion and f0 artifacts in high resolution T2*-weighted magnetic resonance imaging: application in Alzheimer's disease patients. *NeuroImage*, 51(3), pp.1082-1088.
- van Elderen S.G.C, **Versluis M.J.**, Westenberg J.J.M., Agarwal H., Smith N.B., Stuber M., de Roos A., Webb A.G., 2010. Right coronary MR angiography at 7 T: a direct quantitative and qualitative comparison with 3 T in young healthy volunteers. *Radiology*, 257(1), pp.254-259.
- Brandts A., Westenberg J.J.M., **Versluis M.J.**, Kroft L.J.M., Smith N.B., Webb A.G., de Roos A., 2010. Quantitative assessment of left ventricular function in humans at 7 T. *Magnetic Resonance in Medicine*, 64(5), pp.1471-1477.
- Liem M.K., van der Grond J., **Versluis M.J.**, Haan J., Webb A.G., Ferrari M.D., van Buchem M.A., Lesnik Oberstein S.A.J., 2010. Lenticulostriate arterial lumina are normal in cerebral autosomal-dominant arteriopathy with subcortical infarcts and leukoencephalopathy: a high-field in vivo MRI study. *Stroke; a Journal of Cerebral Circulation*, 41(12), pp.2812-2816.
- Zwanenburg J.J.M., **Versluis M.J.**, Luijten P.R., Petridou N., 2011. Fast high resolution whole brain T2* weighted imaging using echo planar imaging at 7T. *NeuroImage*, 56(4), pp.1902-1907.
- Snaar J.E.M., Teeuwisse W.M., **Versluis M.J.**, van Buchem M.A., Kan H.E., Smith N.B., Webb A.G., 2011. Improvements in high-field localized MRS of the medial temporal lobe in humans using new deformable high-dielectric materials. *NMR in Biomedicine*, 24(7), pp.873-879.
- Versluis M.J.**, Webb A.G. van Buchem M.A., 2011. Detection of microbleeds – physical principles, technical aspects and new developments, book chapter in *Cerebral Microbleeds: Pathophysiology to Clinical Practice*, edited by Werring D.J., ISBN: 9780521198455

- Versluis M.J.**, Sutton B.P., de Bruin P.W., Börnert P., Webb A.G., van Osch M.J.P., 2012. Retrospective image correction in the presence of nonlinear temporal magnetic field changes using multi-channel navigator echoes. *Magnetic Resonance in Medicine*, 68(6), pp.1836-1845.
- Versluis M.J.**, van der Grond J., van Buchem M.A., van Zijl P., Webb A.G., 2012. High-field imaging of neurodegenerative diseases. *Neuroimaging Clinics of North America*, 22(2), pp.159-71.
- Doan N.T., van Rooden S., **Versluis M.J.**, Webb A.G., van der Grond J., van Buchem M.A., Reiber J.H.C., Milles J., 2012. Combined magnitude and phase-based segmentation of the cerebral cortex in 7T MR images of the elderly. *Journal of Magnetic Resonance Imaging* 36(1), pp.99-109.
- Dumas E.M., **Versluis M.J.**, van den Bogaard S.J.A., van Osch M.J.P., 't Hart E.P., van Roon-Mom W.M.C., van Buchem M.A., Webb A.G., van der Grond J., Roos R.A.C., 2012. Elevated brain iron is independent from atrophy in Huntington's Disease. *Neuroimaging*, 61(3), pp.558-64.
- Liem M.K., Lesnik Oberstein S.A., **Versluis M.J.**, Maat-Schieman M.L., Haan J., Webb A.G., Ferrari M.D., van Buchem M.A., van der Grond J., 2012. 7 T MRI reveals diffuse iron deposition in putamen and caudate nucleus in CADASIL. *J Neurol Neurosurg Psychiatry*, 83(12), pp.1180-1185.
- Kröner E.S., van Schinkel L.D., **Versluis M.J.**, Brouwer N.J., van den Boogaard P.J., van der Wall E.E., de Roos A., Webb A.G., Siebelink H.M., Lamb H.J., 2012. Ultrahigh-Field 7-T Magnetic Resonance Carotid Vessel Wall Imaging: Initial Experience in Comparison With 3-T Field Strength. *Investigative Radiology*, 47(12), pp.697-704.
- Versluis M.J.**, Teeuwisse WM, Kan HE, Van Buchem MA, Webb AG, Van Osch MJ. Subject tolerance of 7T MRI examinations. *Journal of Magnetic Resonance Imaging* 2012 (in press).

CONFERENCE PROCEEDINGS AND INVITED TALKS

- Versluis M.J.**, Webb A.G., van Osch M.J.P., Magnetic field correlation contrast in the human brain at 7 Tesla, Oral presentation in: Proceedings of the second Annual Meeting of the Benelux chapter of the ISMRM, Antwerpen 2008
- Versluis M.J.**, van Elderen S.G.C., Webb A.G., Westenberg J.J.M., Doornbos J., Smith N.B., de Roos A., Stuber M., In Vivo Human Coronary Magnetic Resonance Angiography at 7 Tesla, Oral presentation in: Proceedings of the 17th Scientific Meeting, International Society for Magnetic Resonance in Medicine, Honolulu 2009
- Versluis M.J.**, Webb A.G., Milles J., Kan H.E., van Buchem M.A., van Osch M.J.P., Quantitative Susceptibility mapping using additional low resolution scans, Oral presentation in: Proceedings of the 17th Scientific Meeting, International Society for Magnetic Resonance in Medicine, Honolulu 2009
- Versluis M.J.**, Kan H.E., Teeuwisse W.M., van Buchem M.A., Webb A.G., Improved proton spectroscopy at 7T using localized B1 calibration, Poster presentation in: Proceedings of the 17th Scientific Meeting, International Society for Magnetic Resonance in Medicine, Honolulu 2009
- Versluis M.J.**, Webb A.G., van Buchem M.A., van Osch M.J., Magnetic field correlation contrast in the human brain at 7 Tesla, Poster presentation in: Proceedings of the 17th Scientific Meeting, International Society for Magnetic Resonance in Medicine, Honolulu 2009

- Versluis M.J.**, Peeters J.M., van Rooden S., van der Grond J., van Buchem M.A., Webb A.G., van Osch M.J., Assessment of motion and f_0 artifacts in 7T high resolution T_2^* -weighted imaging in Alzheimer's disease patients, and application of a navigator-based correction scheme, Oral presentation in: Proceedings of the 18th Scientific Meeting, International Society for Magnetic Resonance in Medicine, Stockholm 2010
- Versluis M.J.**, Peeters J.M., van Rooden S., van der Grond J., van Buchem M.A., Webb A.G., van Osch M.J., Assessment of motion and f_0 artifacts in 7T high resolution T_2^* -weighted imaging in Alzheimer's disease patients, and application of a navigator-based correction scheme, Oral presentation in: Proceedings of the third Annual Meeting of the Benelux chapter of the ISMRM, Utrecht 2010
- Versluis M.J.**, Teeuwisse W.M., Kan H.E., Webb A.G., van Osch M.J., Subject Tolerance For A Whole Body 7T Scanner, Poster presentation in: Proceedings of the 19th Scientific Meeting, International Society for Magnetic Resonance in Medicine, Montréal 2011
- Versluis M.J.**, Webb A.G., Börnert P., van Buchem M.A., van Osch M.J., Spatial Field Monitoring Using Navigator Echoes, Poster presentation in: Proceedings of the 19th Scientific Meeting, International Society for Magnetic Resonance in Medicine, Montréal 2011
- Versluis M.J.**, Dumas E.M., van den Bogaard S.J., Webb A.G., van Buchem M.A., 't Hart E.P., van Osch M.J., van der Grond J., Roos R.A., Changes in Iron Concentration of the Basal Ganglia in Huntington's Disease Using Magnetic Field Correlation, Poster presentation in: Proceedings of the 19th Scientific Meeting, International Society for Magnetic Resonance in Medicine, Montréal 2011
- Versluis M.J.**, Vessel imaging at 7T: coronary angiography, Invited talk at Biennial high field workshop, Center for magnetic resonance research (CMRR), Minneapolis, Minnesota, 2011

Dankwoord

DANKWOORD

Dan is het nu tijd om een aantal mensen te bedanken. Zonder hun hulp zou dit proefschrift nooit tot stand gekomen zijn.

Ik zal beginnen bij het begin. Dr. M.J.P van Osch, beste Thijs, toen ik toevallig bij je langs kwam tijdens een bezoek aan het LUMC heb je me overtuigd van de spannende tijd die zou komen. De 7 Tesla stond er nog niet, ik werkte nog voor Philips en de groep onderzoekers was nog een stuk kleiner dan nu, maar er stond veel te gebeuren. Dankzij dit gesprek ben ik begonnen in het C.J. Gorter centrum en ik wil je bedanken voor alle begeleiding en de altijd weer nieuwe invalshoeken. Als jij het eenmaal met de tekst in een artikel eens was dan viel het review proces altijd weer mee.

Prof. Dr. A.G. Webb, beste Andrew, bedankt voor de fijne werk omgeving die het Gorter centrum is geworden. Je hebt met jouw zeer brede kennis en interesse er voor gezorgd dat dit een veel diverser proefschrift is geworden dan ik van te voren voor mogelijk had gehouden. Bedankt ook voor alle hulp tijdens het schrijven. Ik weet dat je Nederlands beter is dan wij denken.

Prof. Dr. M.A. van Buchem, beste Mark, zonder jou was de 7 Tesla en het Gorter centrum er nooit geweest. Ik weet zeker dat dit proefschrift veel technischer is geworden dan je oorspronkelijk had gedacht en ik wil je bedanken voor de ruimte die je me hebt geboden dit naar eigen wens in te kunnen vullen.

Daarnaast wil ik jullie bedanken dat jullie mijn promotores en co-promotor willen zijn.

Wouter en Hermien, (ex-)kamerogenoten van de enige kamer met daglicht. Ik weet dat jullie je gespreksonderwerpen vaak hebben moeten aanpassen als ik er was, geen Crusoe island, maar Boer zoekt Vrouw. Ik heb met veel plezier een kamer met jullie gedeeld en door onze verschillende achtergronden veel geleerd en gelachen. Ik hoop nog lang met jullie samen te kunnen werken.

Itamar, jouw eindeloze plannen en pulsprogrammeer wensen hebben bij mij tot veel nieuwe inzichten en ideeën geleid, bedankt daarvoor.

Jeroen, bedankt voor alle zinvolle, maar ook sociale bezoeken aan het Gorter centrum. Je enthousiasme is van grote afstand te horen.

Hans Peeters, voormalige collega bij Philips, bedankt voor alle hulp bij het maken van reconstructie patches. Zonder jou geen navigators.

Ilya, Paul, Nicole, Koos, Sanneke, Beatrijs en Mathijs, bedankt voor alle gesprekken soms over werk, maar vaak ook niet. Ik hoop dat we de traditionele maandagmiddag borrel kunnen voortzetten.

Rob, bedankt voor alle CCLB-tjes tijdens elke fase van ons onderzoek. Jammer dat we geen collega's meer zijn, maar ik kijk uit naar jouw promotie!

Michiel, bedankt voor het mooie ontwerp!

Ik wil de rest van het Gorter centrum bedanken, jullie zijn een bijzondere en hechte groep.

Lieve Marjan, er is veel gebeurd in de tijd dat dit proefschrift tot stand is gekomen. Samen kunnen we de wereld aan!

Curriculum Vitae

CURRICULUM VITAE

In August 2005 Maarten Versluis (Bussum, 1979) received a Master's degree in Applied Physics at the University of Groningen, specializing in functional MRI research. After staying for a period of six months at the department he moved to Philips Medical systems in Best, working in the MR methods group on the development of MR pulse sequences. After almost two years he moved in November 2007 to the Leiden University Medical Center to work on the development of new scanning techniques for the recently installed 7 Tesla MRI scanner. The work towards his PhD was conducted at the C.J. Gorter Center within the department of Radiology of the Leiden University Medical Center. He currently works as a postdoctoral researcher on the development of techniques to compensate for motion induced artefacts, a collaboration between the Leiden University Medical Center and the Utrecht University Medical Center.

CURRICULUM VITAE

